

THE ASSEMBLY AND SIZE EVOLUTIONARY PROCESSES OF LOW REDSHIFT,  
MASSIVE, CENTRAL GALAXIES



THOMAS MATTHEW JACKSON



Dissertation submitted to the  
combined Faculties of the Natural Sciences and Mathematics  
of the Ruperto-Carola-University of Heidelberg, Germany,  
for the degree of Doctor of Astronomy

Put forward by:  
Thomas Matthew Jackson

Born in: Gloucester, United Kingdom  
Oral examination: 19 July 2021



TO ALL MY FRIENDS FROM MY TIMES IN YORK, DURHAM AND HEIDELBERG, WHO HAVE ALWAYS BEEN THERE TO BRING OUT THE BEST IN ME, TO CELEBRATE THE GOOD TIMES WITH ME, AND FOR ALL THE GOOD MEMORIES MADE OVER THE YEARS. TO MY SUPERVISOR, MENTOR AND FRIEND DR. ANNA PASQUALI, WHO WAS NEVER SHORT OF ENTHUSIASM AND ENCOURAGEMENT IN GETTING ME THROUGH THIS PhD AND THE CONVERSATIONS THROUGHOUT, BOTH SCIENTIFIC AND NON-SCIENTIFIC. TO MY PARENTS, JEREMY AND PATRICIA JACKSON, AND MY SIBLINGS HARRY, JOSEPH, HAMISH AND MEGAN JACKSON, WHO ARE THE HARDEST PEOPLE I KNOW IN THIS WORLD AND A WONDERFUL FAMILY, SUPPORTING ME ALL THE WAY AND MAKING ME WHO I AM TODAY (AND TO MY GRANDPARENTS PHILLIP AND THELMA JACKSON WHO I REALLY WISH COULD HAVE BEEN HERE TO SEE THIS). FINALLY TO MY PARTNER MELANIE KAASINEN FOR ALL THE SUPPORT AND LOVE REGARDLESS OF THE TIME OR SITUATION, YOU'RE A CONSTANT INSPIRATION TO ME AND ONE OF THE MOST REMARKABLE PEOPLE I'VE EVER MET. THANK YOU ALL, BECAUSE WITHOUT ALL OF YOU THIS FARM LAD FROM THE LAKE DISTRICT WOULDN'T HAVE MADE IT THIS FAR.

THOMAS MATTHEW JACKSON - MAY 2021

## ABSTRACT

---

I present a study into the stellar mass assembly and size growth of low redshift, massive, central galaxies using a three-stage process. Stage one investigates the stellar mass assembly times of  $\sim 90,000$  galaxies from the SDSS. Stellar mass is the main driver of assembly, with secondary dependencies on environment. A comparison to simulations shows that despite reproducing isolated trends, simulations struggle to reproduce secondary trends. Stage two investigates the nature of low surface brightness (LSB) features around a sub-sample (236) of these galaxies using deep, multi-band imaging from Subaru-HSC. High levels of interaction features are found from minor mergers, imprinted on stellar mass profiles. The LSB material properties such as stellar mass and colours are similar to SDSS satellites. This provides the first direct observational evidence of minor mergers driving the size evolution of galaxies. Stage three uses stellar population fitting of IFU data for a further sub-sample (15) of these galaxies. Subtle differences in age and metallicity profiles in galaxies of different interaction classes are found, however no difference in fractions of ex-situ stars are found. Differences in the stellar populations of galaxies are found to be preferentially linked to the assembly histories, not interaction morphologies.

## ZUSAMMENFASSUNG

---

Ich präsentiere eine Studie über die Anordnung von Sternmassen und das Größenwachstum von massereichen Zentralgalaxien mit niedriger Rotverschiebung in drei Teilen. Der erste Teil untersucht die Anordnungszeiten von Sternmassen aus  $\sim 90.000$  Galaxien der SDSS. Die Anordnungszeiten hängen primär von der Sternmasse ab, sekundär von der Umgebung. Der Vergleich mit Simulationen zeigt, dass Simulationen trotz der Reproduktion isolierter Trends Schwierigkeiten haben, sekundäre Trends zu reproduzieren. Der zweite Teil der Studie untersucht die Eigenschaften von Materie niedriger Oberflächenhelligkeit (LSB-Materie) um eine Teilprobe (236) dieser Galaxien, unter Verwendung von tiefen Multiband-Bildgebung durch Subaru-HSC. Große Mengen an Interaktionsmerkmalen weisen ein hohes Maß an kleinen Galaxienverschmelzungen auf, die auf Sternmassenprofilen zu erkennen sind. Die Eigenschaften der LSB-Materie, wie Sternmasse und Farbe ähneln denen von SDSS Satellitengalaxien. Dies liefert den ersten direkten Beobachtungsnachweis für kleinere Galaxienverschmelzungen, die die Größenentwicklung von Galaxien vorantreiben. Der dritte Teil der Studie verwendet Datenanpassung von Sternpopulation aus IFU-Daten für eine weitere Teilprobe (15) dieser Galaxien. Es werden leichte Unterschiede in den Alters- und Metallprofilen in Galaxien verschiedener Verschmelzungsklassen gefunden, jedoch keine Unterschiede in den Profilen von ex-situ Sternen. Unterschiede in den Sternpopulationen von Galaxien hängen bevorzugt mit der Anordnungsgeschichte zusammen, nicht mit Interaktionsmorphologien.



# Contents

1	INTRODUCTION	1
1.1	The Stellar Mass Assembly and Properties of Central Galaxies . . . . .	4
1.2	The Size Growth of Central Galaxies . . . . .	9
1.3	The Effect of Mergers on Central Galaxies . . . . .	13
1.4	This Work on Central Galaxies . . . . .	15
2	DATA AND METHODS FOR THE STELLAR MASS ASSEMBLY OF CENTRAL GALAXIES	19
2.1	The SDSS Group Catalogues . . . . .	19
2.2	The Photometric SED Fitting Process of <a href="#">Pacifci et al. (2012)</a> . . . . .	23
2.3	The Illustris TNG Simulation Suite . . . . .	24
2.4	The Selection of the Simulated Sample . . . . .	26
3	RESULTS I - THE STELLAR MASS ASSEMBLY OF CENTRAL GALAXIES IN SDSS AND TNG	29
3.1	The Average Assembly Times of SDSS and TNG300 Galaxies . . . . .	29
3.2	The Differences in the Lookback Times between SDSS and TNG300 . . . . .	31
3.3	The Characteristic Galaxy Properties of TNG300 Galaxies . . . . .	34
3.4	The Stellar Mass Growth Rate of SDSS Galaxies . . . . .	36
3.5	Assembly Trends Yielded from the EAGLE Simulations . . . . .	38
4	DATA AND METHODS FOR THE SIZE GROWTH OF CENTRAL GALAXIES	41
4.1	The Subaru Hyper-Suprime-Cam Survey and Data . . . . .	41
4.2	The Visual Classification Scheme . . . . .	44
4.3	The Treatment Process of the HSC Imaging Data . . . . .	46
4.4	The SED Fitting Process with CIGALE . . . . .	49
5	RESULTS II - THE SIZE GROWTH OF CENTRAL GALAXIES THROUGH RADIAL PROFILES	53
5.1	The Levels of Merger Activity . . . . .	53
5.2	Colour and Stellar Mass Density Profiles of HSC Galaxies . . . . .	54

5.3	The Profiles Yielded from Stacked Imaging . . . . .	57
5.4	The Profiles of Interaction Sub-samples . . . . .	60
6	DATA AND METHODS FOR THE RADIAL GRADIENTS OF CENTRAL GALAXIES	63
6.1	The SAMI Survey and Data . . . . .	63
6.2	Stellar Populations and STARLIGHT . . . . .	65
6.3	The In- and Ex-Situ Fractions of Stars (via <a href="#">Boecker et al. 2020</a> ) . . . . .	69
7	RESULTS III - THE STELLAR POPULATION RADIAL GRADIENTS OF CENTRAL GALAXIES	73
7.1	The Age and Metallicity Profiles of SAMI-HSC Galaxies . . . . .	73
7.2	The Stellar Mass Density Profiles of SAMI-HSC Galaxies . . . . .	75
7.3	The Stellar Population Profiles of Interaction Sub-Samples . . . . .	76
7.4	Stellar Mass vs Intrinsic Differences in Stellar Populations . . . . .	78
7.5	The In- and Ex-situ Fractions of SAMI-HSC Galaxies . . . . .	80
8	DISCUSSION	83
8.1	Discussion I - Interpreting the Stellar Mass Assembly of Central Galaxies . .	84
8.1.1	Trends in the Formation Times: Stellar Mass vs Halo Mass . . . . .	84
8.1.2	High Stellar-to-Halo Mass Objects: The Exception to Downsizing . .	85
8.1.3	Connecting the Oldest Galaxies and High Redshift, Compact Objects	86
8.2	Discussion II - Interpreting LSB Material around Central Galaxies . . . . .	86
8.2.1	Comparison of the Colour Profiles to SDSS Satellites . . . . .	86
8.2.2	Interpretation of the Merger Activity and Radial Profile Excesses . . .	88
8.2.3	Comparison to HSC studies and Difference in Activity Levels . . . . .	90
8.3	Discussion III - Interpreting the Stellar Populations of Central Galaxies . . .	92
8.3.1	Upper Limits on the Fractions of Ex-Situ Material . . . . .	92
8.3.2	The Driver of Intrinsic Differences in Stellar Populations . . . . .	93
8.4	Discussion IV - Future Outlooks for Central Galaxies . . . . .	94
9	CONCLUSION	97
A	APPENDIX: CHECKS OF THE DATA AND POSSIBLE BIASES	101
A.1	Bias Checking the SED Fitting of <a href="#">Pacifci et al. (2016)</a> . . . . .	101
A.2	Selection Effects and Sample Matching Between SDSS and TNG300 . . . . .	104
A.3	Exploration of Biases in the Stellar Mass Estimates from CIGALE . . . . .	105
A.4	Comparing the Estimates of Stellar Populations from Different Methods . . .	106

# List of figures

1.0.1	High redshift, compact, quiescent galaxies from <a href="#">Daddi et al. (2005)</a> . . . . .	3
1.1.1	An example of stellar population modelling . . . . .	5
1.1.2	An example of SED fitting from <a href="#">Leja et al. (2019)</a> . . . . .	7
1.2.1	The size growth of galaxies from <a href="#">van der Wel et al. (2014)</a> . . . . .	10
1.3.1	The in- and ex-situ material of galaxies from <a href="#">Remus &amp; Forbes (2021)</a> . . . . .	16
2.1.1	The average properties of our SDSS galaxy sample . . . . .	22
2.4.1	The SDSS and TNG galaxy samples in stellar and halo mass phase space . . . . .	28
3.1.1	The stellar mass assembly lookback times of SDSS galaxies . . . . .	30
3.1.2	The stellar mass assembly lookback times of TNG300 galaxies . . . . .	31
3.2.1	Detailed trends in the stellar mass assembly lookback times . . . . .	32
3.3.1	General properties of the TNG300 galaxy sample . . . . .	35
3.4.1	The growth rates of SDSS galaxies . . . . .	37
3.5.1	The stellar age of <code>EAGLE</code> galaxies . . . . .	40
4.1.1	Properties of the HSC sample . . . . .	43
4.2.1	Classification examples in HSC imaging data . . . . .	45
4.3.1	Examples of the processing of the HSC sample . . . . .	48
4.4.1	SED fitting examples using <code>CIGALE</code> of central regions of HSC galaxies . . . . .	50
4.4.2	SED fitting examples using <code>CIGALE</code> of outer regions of HSC galaxies . . . . .	52
5.1.1	Merger activity levels of HSC galaxies . . . . .	54
5.2.1	Radial profiles of the HSC passive sample . . . . .	55
5.2.2	Radial profiles of the HSC comparison sample . . . . .	56
5.3.1	Radial profiles of stacked galaxies and PSF effects . . . . .	59
5.4.1	Radial profiles of different interaction classes . . . . .	61
6.1.1	The SAMI-HSC sample . . . . .	64

6.2.1	An example fitted spectrum with STARLIGHT . . . . .	67
6.2.2	Further example STARLIGHT fits . . . . .	68
6.3.1	The estimation process of in- and ex-situ stars . . . . .	71
6.3.2	Further examples of estimating in- and ex-situ fractions . . . . .	72
7.1.1	Age and metallicity profiles of SAMI-HSC galaxies . . . . .	74
7.2.1	Stellar mass surface density and velocity dispersion profiles of SAMI-HSC galaxies . . . . .	76
7.3.1	Stellar population radial profiles of the morphological sub-samples . . . . .	77
7.4.1	Drivers of the differences in the stellar population estimations . . . . .	79
7.5.1	The fraction of in-situ stars with radius for SAMI-HSC galaxies . . . . .	81
7.5.2	The stellar ex-situ fraction of different interaction classes . . . . .	82
8.2.1	$g - r$ colours of SDSS satellite galaxies . . . . .	87
8.2.2	The $t_{90}$ values of different interaction classes . . . . .	91
8.3.1	The $t_{90}$ values of our SAMI-HSC sample . . . . .	94
A.1.1	The average SED and AGN contribution of sub-samples in SDSS . . . . .	102
A.1.2	Assembly trends from alternative catalogues . . . . .	103
A.3.1	Comparison of different SED fitting codes used in this work . . . . .	105
A.4.1	Comparison of estimations from different SSP fitting methods . . . . .	107
A.4.2	Comparison of stellar mass estimations from STARLIGHT and SED fitting . . . . .	108

# List of tables

- 8.2.1 The radial stellar mass distribution of HSC passive galaxies . . . . . 89
- 8.2.2 The radial stellar mass distribution of HSC comparison galaxies . . . . . 89
- 8.3.1 A comparison of the ex-situ stellar fractions . . . . . 93



# Acronyms

**AGN:** Active Galactic Nucleus/Nuclei

**AMR:** Age - Metallicity Relation

**AU:** Astronomical Unit

**BaSTI:** A Bag of Stellar Tracks and Isochrones

**CALIFA:** Calar Alto Legacy Integral Field spectroscopy Area

**DR:** Data Release

**E-ELT:** The European Extremely Large Telescope

**ESO:** The European Southern Observatory

**FoF:** Friends-of-Friends

**FWHM:** Full-width-half-maximum

**GALEX:** The Galaxy Evolution Explorer mission

**HSC:** Hyper-Suprime-Cam (From the Subaru Telescope)

**IFU:** Integral Field Unit

**IMF:** Initial Mass Function

**IR:** Infrared

**LINER:** Low-Ionization Nuclear Emission-line Region

**LSB:** Low Surface Brightness

**MaNGA:** The Mapping Nearby Galaxies at Apache Point Observatory Survey

**mas:** milli-arcsecond

**MATLAS:** The Mass Assembly of early-Type GaLaxies with their fine Structures survey

**MICADO:** The Multi-AO Imaging Camera for Deep Observations

**MILES:** The Medium-resolution Isaac Newton Telescope Library of Empirical Spectra

**MUSE:** The Multi Unit Spectroscopic Explorer

**NEWFIRM:** The NOAO Extremely Wide Field Infrared Imager

**NFW:** [Navarro et al. \(1997\)](#) (dark matter profile)

**NOAO:** The National Optical Astronomy Observatory

**pc:** Parsec

**pPXF:** The Penalized Pixel-Fitting method ([Cappellari 2017](#))

**PSF:** Point Spread Function

**SAMI:** The Sydney-Australian-Astronomical-Observatory Multi-object Integral-Field Spectrograph

**SDSS:** The Sloan Digital Sky Survey

**SED:** Spectral Energy Distribution

**SFH:** Star Formation History

**SFR:** Star Formation Rate

**sSFR:** Specific Star Formation Rate

**SPH:** Smoothed Particle Hydrodynamics

**SSP:** Simple Stellar Population

**S/N:** Signal-to-Noise

**TNG300:** The 300 Mpc simulation run from the IllustrisTNG suite

**UKIDSS:** The United Kingdom Infrared Deep Sky Survey

**UV:** Ultraviolet

**VLT:** The Very Large Telescope

**WISE:** The Wide-field Infrared Survey Explorer

*"Surely there is no other place in this whole wonderful world quite like Lakeland... no other so exquisitely lovely, no other so charming, no other that calls so insistently across a gulf of distance. All who truly love Lakeland are exiles when away from it."*

Alfred Wainwright – The complete pictorial guides of the Lake District, 1955 - 66

# 1

## Introduction

A full description of the stellar mass assembly history and growth of galaxies is unfortunately impossible to summarise in just one thesis. This is due to the extremely wide range of astrophysical processes which may influence the assembly and evolution of any one galaxy or a population of galaxies. The astrophysical processes involved range from star formation and giant molecular clouds on astronomical unit (AU) and parsec (pc) scales respectively to galactic instabilities and environmental processes on kpc and Mpc scales, to name but a few. Having to track and account for such processes over twelve orders of magnitude, which can also be interlinked or interdependent on each other presents a major challenge to improving our models of galaxy assembly and evolution. Other problems are presented by the exact contributions of each of the various processes mentioned above and the numerous other processes not covered here, both relatively well and poorly known to researchers. Indeed astronomers are likely to be working for a long time yet using both observations and theory, in an attempt to unravel many of the questions associated with galaxy assembly and evolution.

The introduction of this thesis attempts to provide an overview of the relevant astrophysical processes and the techniques used throughout this research into galaxy evolution, parts of which have been published in the following studies of [Jackson et al. \(2020b\)](#), [Jackson et al. \(2021\)](#) and Jackson et al. (in prep.). Citations are also included where the reader can find more detailed information on the subjects provided. The reader is also referred to the following book of [Mo, van den Bosch & White \(2010\)](#), commonly known in the research group as the "Bible" of galaxy formation and evolution, which covers a much wider range of topics and astrophysical processes within the subject of galaxy formation and evolution than this thesis. I concentrate this research on one type of galaxy, so as to avoid spreading the scope of this research too thinly trying to encompass the significant variety of galaxies

within the known Universe. In particular, as the title of this thesis states, on the assembly and size evolutionary processes of low redshift, massive, central galaxies.

Massive, central galaxies are defined as the galaxy with the highest stellar mass (usually  $10^{10-12} M_{\odot}$ ) or highest luminosity within their dark matter halo (Yang et al. 2007). They also make up the most massive objects in our universe today, with masses up to and greater than  $10^{12}$  solar masses (Vulcani et al. 2011; Vázquez-Mata et al. 2020). They are also the likely evolutionary endpoint of all galaxies, including our own Milky Way. Studying samples of massive, central galaxies at low redshift means that these types of galaxies can also be studied in great detail due to good spatial resolution and the wealth of data sets compared to high redshift objects, thereby better constraining their evolutionary histories.

Numerous observational, theoretical and simulational studies have been carried out probing the nature and properties of massive, central, quiescent galaxies ("quiescent" indicates low levels of star formation, such as a specific star formation rate  $< 10^{-11} \text{ Gyr}^{-1}$  in Pasquali et al. 2019, where specific star formation rate = star formation rate / stellar mass). This population appears visually, on average, rather homogeneous and relatively simple compared to their late morphological type counterparts. This simplicity is reflected by the tight scaling relations that these galaxies display between numerous galaxy properties such as the size, surface brightness and the stellar velocity dispersion (which is tightly correlated to the stellar mass). These relations between size, surface brightness and velocity dispersion are all different dimensional projections of what is commonly known as the fundamental plane of elliptical galaxies (Faber & Jackson 1976; Dressler et al. 1987). The majority of these galaxies have also been found to display relatively smooth structure and surface brightness profiles (Gott 1975; Carter 1979; Huang et al. 2018b), old stellar ages (Thomas et al. 2005; Gallazzi et al. 2005), little star formation (Brinchmann et al. 2004) and relatively little molecular gas (Lees et al. 1991; Young et al. 2011).

These properties and observational trends led early studies to conclude a fairly simple formation and evolution scenario for such galaxies. The scenario presented by these early studies claimed that the bulk of the stellar mass was formed in a short but massive and intense burst of star formation at high redshift, before an almost completely passive evolution to the present epoch (Thomas et al. 2005; Renzini 2006). However, a renewed interest in this population of galaxies was motivated by evidence of a more complex evolution than a simple burst of star formation followed by a completely passive evolution. This spark came from one observational study in particular, that of Daddi et al. (2005). The results of their study have led to numerous follow-up studies over the last 15 years into the formation and evolution of massive, quiescent galaxies, both observational and theoretical.

In their study, Daddi et al. (2005) used a colour-colour selection criterion ( $BzK$ , see Daddi et al. 2004, 2005, for more details) to select and study seven massive, early-type, quiescent galaxies in the Hubble Ultra-Deep Fields (see the left panel of Figure 1.0.1 for an example galaxy). They used ACS grism spectra to confirm the high redshifts of these objects, ranging from  $1.4 \lesssim z \lesssim 2.7$ . They also used spectral energy distribution (SED) fitting on the extracted photometry of the imaging data to estimate high stellar masses and relatively old average stellar ages at these cosmic epochs, confirming their quiescent nature. The sur-

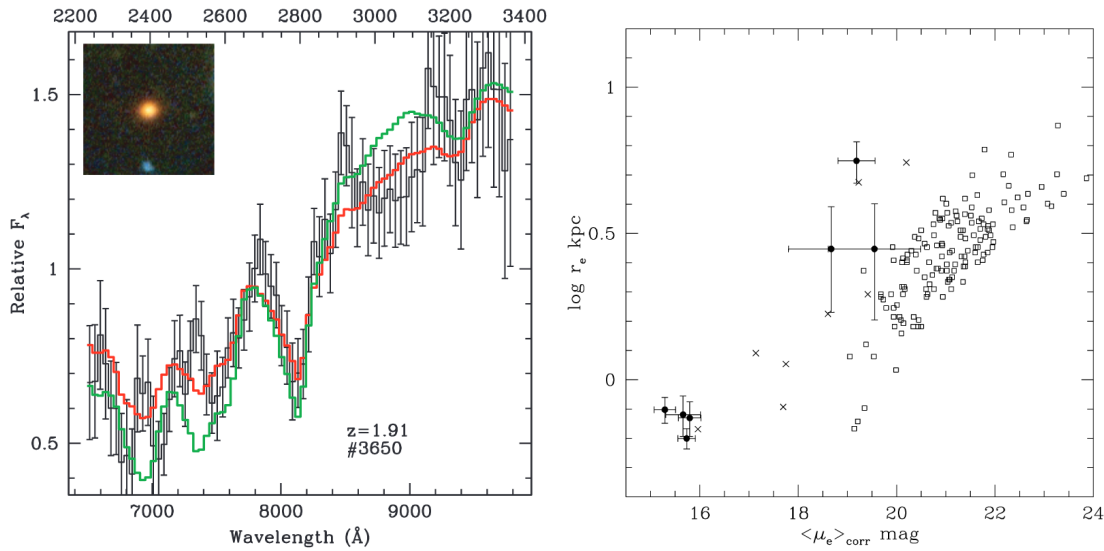


**Figure 1.0.1:** Figures 5 and 12 from the study of [Daddi et al. \(2005\)](#). **Left panel:** An example of one of the quiescent galaxy sample, with HST imaging in the inset and the corresponding ACS grism spectra in the main section of the panel (black lines) with two different stellar population fits (orange and green). The quiescent nature is confirmed by the large drop at  $\lambda \sim 8200 \text{ \AA}$  and the relatively red spectrum. A visual inspection of the imaging data shows red colours and a fairly early-type morphology. **Right panel:** The high redshift, quiescent galaxy sample represented by black points in the size - surface brightness plane compared to a low redshift sample of quiescent galaxies represented by the empty squares. The quiescent sample occupy a part of the phase space not populated by galaxies in the local Universe, being much more compact than their low redshift counterparts.

prising result from this study, however, was the seemingly compact sizes of their sample. They found that the radius enclosing half of the integrated light of the objects, better known as the effective radius, of four out of their seven galaxies was  $< 1 \text{ kpc}$ . This is compared to an average effective radius of 5 - 10 kpc expected for galaxies of similar stellar mass in the low redshift universe ([Kormendy 1977](#)). When a passive evolution for these objects is assumed, they populate a part of the Kormendy relation ([Kormendy 1977](#)), or alternatively the fundamental plane ([Faber & Jackson 1976](#); [Dressler et al. 1987](#)), not populated by low redshift galaxies ([Daddi et al. 2005](#), see the right-hand panel of [Figure 1.0.1](#)). These differences in size imply a substantial stellar mass density difference of an order of magnitude ([Bezanson et al. 2009](#)). The corresponding lack of compact, massive objects at low redshift and the dearth of large, massive systems at high redshift re-ignited the debate of how the most massive elliptical galaxies in our local universe were formed and what their connection is to these abundant, high redshift, compact, massive objects.

## 1.1 The Stellar Mass Assembly and Properties of Central Galaxies

To understand the evolution of low redshift, massive, quiescent galaxies, the assembly of a galaxy's stellar mass needs to be understood initially. The stellar mass is the result of any one galaxy's integrated star formation history (SFH), making it an indicator of the processes that a galaxy may have undergone throughout its lifetime. There are a number of different techniques used for estimating the stellar mass of a galaxy, such as colour relations motivated by simple stellar population assumptions (e.g. [Bell et al. 2003](#)), dynamical estimates from orbiting systems such as globular clusters or satellite galaxies (e.g. [Callingham et al. 2019](#)), SED fitting of observed photometry (e.g. [Brinchmann et al. 2004](#); [Salim et al. 2016](#)) or fitting stellar populations to observed spectra (e.g. [Cid Fernandes et al. 2005](#)). I will outline the latter two techniques as these are the most commonly used in current studies and are also utilised within this research.

Both SED fitting and stellar population modelling (also referred to as spectral fitting) rely on the utilisation of a large database of stars, better known as a stellar library. This stellar library can be built in two different ways. The first route is to use a collection of observed stars in the vicinity of our solar system which are well known and calibrated, better known as an empirical library (like those of [Bruzual & Charlot 2003](#); [Vazdekis et al. 2010](#)). The second route is to use a collection of simulated stars which are theoretically synthesised using techniques such as modelling of stellar atmospheres and radiative transfer codes (like those of [Maraston 2005](#)).

Both the libraries of empirical and theoretical single-age stellar spectra need a wide and detailed range of models in order to sufficiently sample the parameter space in age and metallicity, resulting in stellar libraries of up to hundreds of possible stars. The stars usually cover a wide range of ages, from the youngest stars with an age of approximately 10 Myr to the oldest with ages of  $\sim 13$  Gyr. The stellar libraries also cover a range of metallicities, from extremely metal-poor stars containing  $1/100^{\text{th}}$  of the solar metallicity to metal-rich at a few times solar metallicity. An example empirical stellar library of different metallicities and ages is shown the top panel of Figure 1.1.1. Some libraries also contain models with stars which display an enhancement in the abundance of  $\alpha$  elements, usually indicative of a stellar population which has undergone a short, intense burst of star formation.

Importantly, there are degeneracies between the colour of the star, its age, and its metallicity, whereby a stellar population may be redder either because it is older, more metal-rich, or both and vice-versa (known as the age-metallicity degeneracy, see e.g. [Vazdekis et al. 2010](#), and references therein for more information and possible ways to break this degeneracy). This means that such techniques have to be used with care.

The library of stellar spectra is then combined with the assumption of a certain stellar Initial Mass Function (IMF, e.g. [Salpeter 1955](#); [Chabrier 2003](#)). The IMF determines the relative fractions of certain masses of stars in a stellar population as a function of stellar mass of those stars, i.e. the fraction of low to high mass stars expected to be born on average in a cloud/galaxy. A further combination is performed with models of stellar evolution in the form of isochrones (e.g. the BaSTI isochrones, [Hidalgo et al. 2018](#)) in order to calculate the

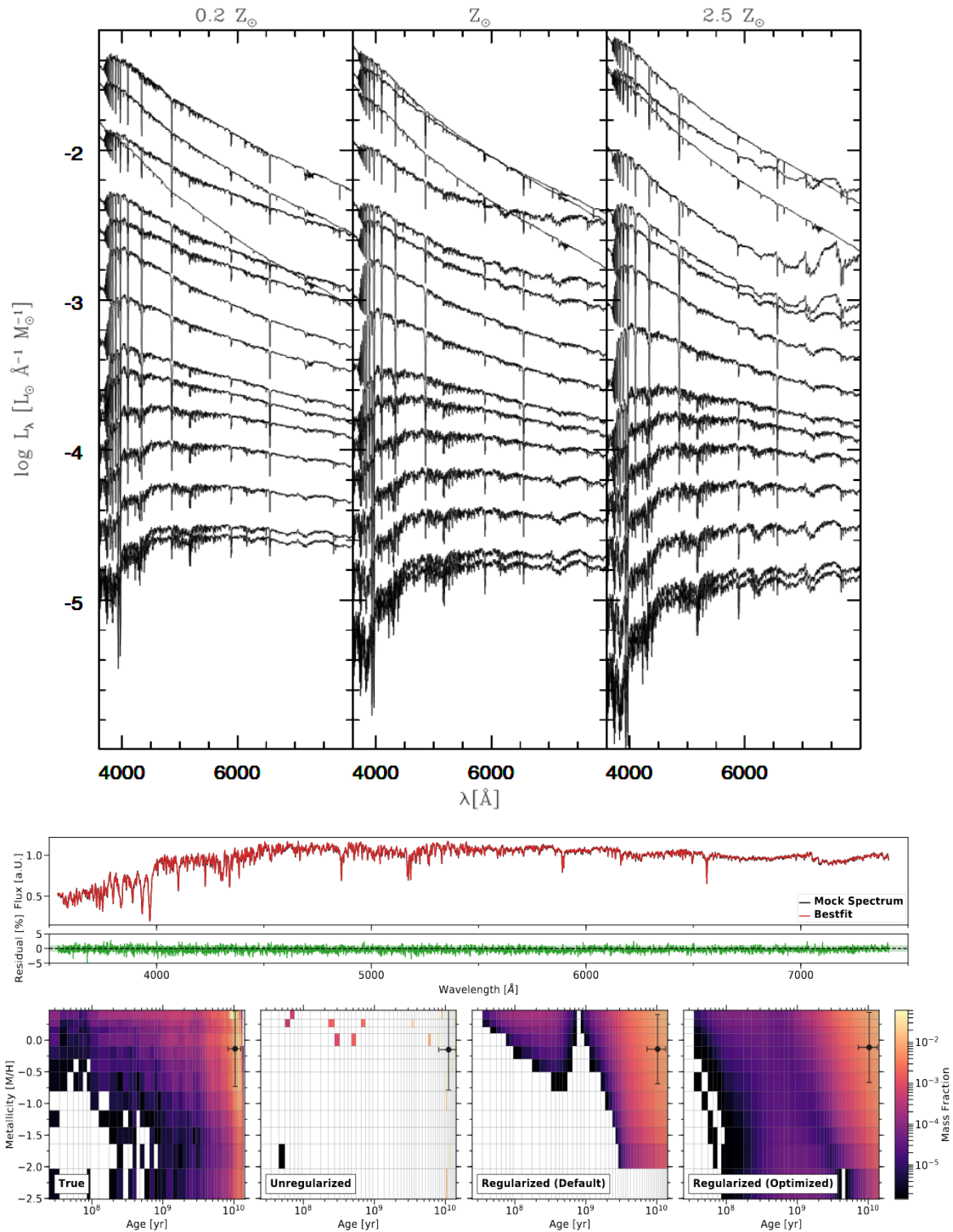


**Figure 1.1.1:** Top panel: Figure 1 of [Cid Fernandes et al. \(2005\)](#). Stellar populations with different metallicities ranging from left to right and ages varying between 1 and 13 Gyr from top to bottom in each metallicity bin. Mid and bottom panels: Figure 2 from [Boecker et al. \(2020\)](#). Mid panel: A simulated spectra in black, with the best-fitting stellar population combination given in red, with residuals shown in green directly below. Bottom panels: From left to right the true distribution in age and metallicity of the stellar populations (obtained from simulations) and the age and metallicity distributions estimated by different fitting parameters in the same full spectral fitting code in the following 3 sub-panels (see [Boecker et al. 2020](#), for more details).

relative amount of certain types of stars still contained in an evolved population of a certain age and metallicity. The library of stellar spectra are then summed additively in various weighted fractions according to the expected amount of stars in each population to create a model spectrum of combined stellar populations.

The model spectra are then compared or fitted to the observed spectrum of a galaxy. This fitting process then estimates the best-fitting combination of the stellar populations for each observed spectra. A probability distribution function of each combination can then be built, yielding estimates on the properties of the stellar population such as the total stellar mass, the average stellar age, the stellar metallicity, or alpha element to iron ratio  $[\alpha/\text{Fe}]$  of a population. The estimated properties can then reveal the details of the formation history (see [Conroy et al. 2009](#), and references therein for a detailed summary and overview). An example of this fitting process can be seen in the mid and bottom panels of [Figure 1.1.1](#), whereby the mid panel shows the original spectra in black with the best-fitting spectra in red, with the corresponding true distribution of the stellar population in age and metallicity in the lefthandmost bottom sub-panel and the estimated distributions in age and metallicity found in the other three bottom panels (using different techniques, see [Boecker et al. 2020](#), for more details).

There are, however, some restrictions associated with stellar spectral fitting. The sample sizes can be significantly smaller compared to photometric studies of galaxy evolution, as spectroscopic data requires much longer integration times than imaging. They may also focus mainly on early-type galaxies rather than the general galaxy population due to the problems in breaking degeneracies in dust, age and metallicity, which all cause the colours of stellar populations to redden, that dominate late-type galaxies. Late-type galaxies also generally have more complicated star formation histories, which cannot be well described by a single or relatively simple mixture of stellar populations (see [Conroy et al. 2009](#), and references therein).

An alternative technique to estimate properties of galaxies is via the use of photometric SED fitting (e.g. [da Cunha et al. 2008](#)). SED fitting is based on the same principle as the stellar population modelling described above, whereby a library of stellar populations, either empirical or theoretical is used. The difference, however, is that rather than immediately comparing the constructed library of model spectra to an observed spectra, the model libraries are initially combined with filter functions. These filter functions provide the relative amount of light per wavelength collected by a broad band filter spanning a specific wavelength range (such as those in [Doi et al. 2010](#), describing the filters of the Sloan Digital Sky Survey, or SDSS). The measured fractions are convolved with the model spectra and integrated to calculate the total flux expected in a certain filter from a certain stellar population or combination of stellar populations.

The integrated fluxes from the models are then compared to the fluxes from observed galaxies. Similar to the stellar population modelling, estimates of the best-fitting stellar population properties can then be inferred, such as the stellar mass or approximate stellar age of any one galaxy. The advantage of SED fitting is that other components such as heating from dust via the process of star formation ([Dale et al. 2014](#)) or components from Active

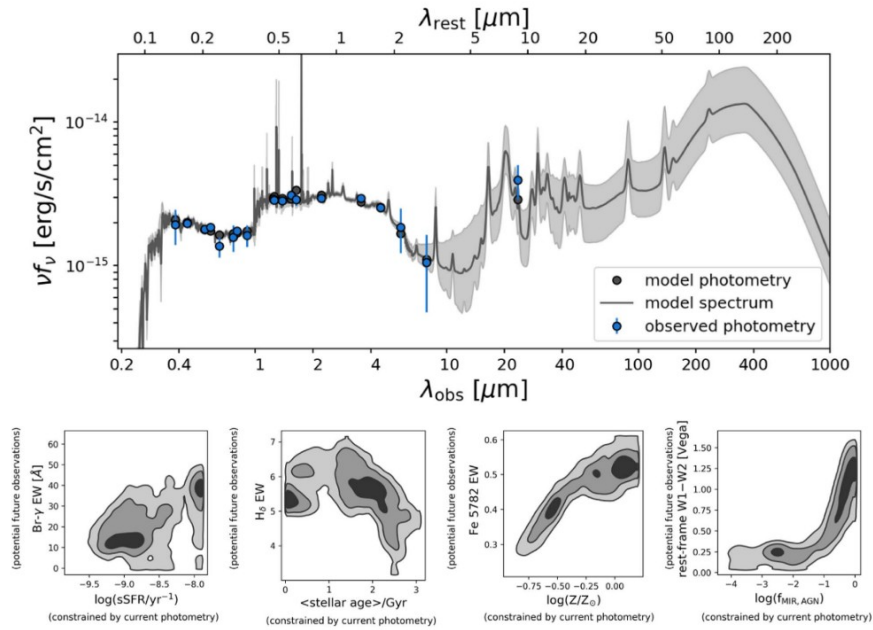


**Figure 1.1.2:** Figure 13 of [Leja et al. \(2019\)](#). **Top panel:** An example best-fitting model spectral energy distribution (SED) represented by the solid black line ( $1\sigma$  uncertainties represented by the shaded area), with the expected fluxes from the SED given by the black circles, compared to the observed photometry given by the blue circles. **Bottom panels:** The probability distributions of the certain galaxy properties, such as stellar age, star formation rate and metallicity, as a function of the corresponding photometric indicators included in the SED fitting process.

Galactic Nuclei (AGN, [Mullaney et al. 2011](#)) can be modelled and accounted for in the fitting process. Due to this enhanced flexibility, as well as the fact that photometry requires much lower exposure times for similar depths or signal-to-noise levels compared to spectra, SED fitting on photometry can be applied on much larger samples of galaxies than stellar population modelling. An example SED can be found in [Figure 1.1.2](#), where the solid black line represents the best-fitting model SED ( $1\sigma$  uncertainties represented by the shaded area), with the expected fluxes from the SED given by the black circles, compared to the observed photometry given by the blue circles. The bottom panels show the probability distributions of certain galaxy properties yielded by the fitting process.

Due to different approaches in the philosophy applied to SED fitting, there are a number of different codes available. Some SED fitting codes use an energy balance principle, whereby the Ultraviolet (UV) light generated by massive, young stars is absorbed by dust and completely re-emitted in the Infrared (IR), such as CIGALE ([Noll et al. 2009](#)) or MAGPHYS ([da Cunha et al. 2008](#)). Other SED fitting codes use combined Bayesian and Monte Carlo methods, along with options like the simultaneous fitting of both photometry and spectroscopy such as BAGPIPES ([Carnall et al. 2018](#)). Another technique gaining increasing usage is the utilisation of SFHs that are not just described by simple mathematical models, such as a declining exponential burst, but which consist of a mixture of functions or shapes.

These irregular SFHs are better known as non-parametric SFHs and are used in codes such as PROSPECTOR (Leja et al. 2017). The range of philosophies and available models and techniques means that care needs to be taken when selecting an SED code for use, whereby the selected code considered is usually chosen dependent on the type of galaxy or galaxy properties of most interest to the researcher. This is because estimates of some parameters, such as a stellar mass, may be well constrained with agreements between different codes within 0.2 dex of each other, but others such as star formation rates can differ by up to an order of magnitude (see e.g. Leja et al. 2019).

Early studies utilising stellar population modelling on integrated galaxy properties found evidence that more massive galaxies form their stars earlier and on shorter timescales than less massive ones (Thomas et al. 2005; Gallazzi et al. 2005; Thomas et al. 2010). This phenomenon of more massive galaxies assembling their stellar mass earlier than less massive ones is commonly known as downsizing (Cowie et al. 1996). These results have also been confirmed by studies using SED fitting on photometric datasets such as the studies of Pacifici et al. (2012, 2016). In their study Pacifici et al. (2016) found a range of values at which galaxies assembled 90 per cent of their stellar mass ( $t_{90}$ ), with the most massive galaxies estimated at having  $t_{90}$  values of up to 10 Gyr, whereas the youngest have an average  $t_{90}$  of  $\sim 2$  Gyr. This difference in  $t_{90}$  values is coupled by a steady transition, in agreement with previous studies using stellar population modelling.

Studies using both stellar population modelling and SED fitting have also found that, as well as displaying older stellar ages, more massive galaxies tend to be metal-enriched and have higher values of  $[\alpha/\text{Fe}]$ , indicative of shorter, more intense bursts of star formation at early cosmic epochs (Thomas et al. 2005; Gallazzi et al. 2005; Thomas et al. 2010). This shows that the stellar mass assembly history is also imprinted on the present-day properties of each galaxy. This work has also been extended by follow-up studies, utilising long slit spectroscopy (La Barbera et al. 2012, 2019; Martín-Navarro et al. 2015) and, more recently, integral field spectroscopy (Wilkinson et al. 2015; Zibetti et al. 2020) to explore galaxy assembly and evolution processes in more detail. Some of the results which have implications on the stellar mass assembly processes of galaxies include evidence for a variable IMF (La Barbera et al. 2019) and the imprints of the energy injected by a black hole quenching star formation (Martín-Navarro et al. 2018).

Estimated stellar ages or stellar mass assembly lookback times are usually compared as a function of stellar mass, which is postulated to be the main driver in galaxy evolution, especially in central galaxies (Gallazzi et al. 2005; Pasquali et al. 2010). Environment, however, is also known to have an effect on galaxy assembly (Pasquali et al. 2010). Processes ranging from star formation (Kennicutt 1998) to the quenching of star formation via supernova or AGN feedback (see e.g. Bower et al. 2006) correlate strongly with the stellar mass of a galaxy. On the other hand major and minor mergers supplying molecular gas for starbursts (e.g. Sanders & Mirabel 1996) and processes which shut down star formation such as strangulation and ram-pressure stripping (see e.g. De Lucia 2011) are triggered by environment. All of the processes mentioned here can affect how any one galaxy assembles its stellar mass.

This variety of astrophysical processes driving stellar mass assembly can also affect the

same present-day galaxy properties meaning that there may be degeneracies between the two drivers of galaxy evolution, including the aforementioned assembly times. By comparing galaxy properties as a function of both stellar mass and environment simultaneously, researchers can attempt to somewhat separate secular evolution from environmental effects. To do this, two proxies for the environmental and secular processes are commonly selected, namely the stellar mass of the galaxy itself for secular processes and the parent halo mass of a galaxy for the environment (Weinmann et al. 2006). Galaxy properties are then usually averaged in bins of stellar and halo mass, or compared in a number of different fixed stellar (halo) masses while varying halo (stellar) mass. This concept has been employed successfully in previous studies in order to investigate galaxy morphological types (Weinmann et al. 2006), AGN activity types (Pasquali et al. 2009), star formation rates (van den Bosch et al. 2008; Wetzel et al. 2012), ages and metallicities (La Barbera et al. 2014; Trussler et al. 2020), and satellite assembly and evolution (Pasquali et al. 2019; Smith et al. 2019) and their dependencies on both halo and stellar mass. This allows us to somewhat disentangle which factors contribute most in influencing the stellar mass assembly of low redshift, massive, central galaxies.

In summary; a number of techniques can be used to estimate the stellar mass assembly of galaxies, such as stellar population modelling or spectral energy distribution fitting. Studies utilising these techniques have already helped constrain our models of the stellar mass assembly of galaxies, also showing that the assembly history of any one galaxy is also imprinted on the average properties of a galaxy population. Many studies have also shown that the stellar mass assembly processes of galaxies can be influenced by both secular effects, driven by the stellar mass of a galaxy, or by the environment that a galaxy is situated in. This means that both stellar mass and environment need to be accounted for simultaneously to break degeneracies which may bias interpretations of observed trends in the stellar mass assembly of low redshift, massive, central galaxies.

## 1.2 The Size Growth of Central Galaxies

With some of the aforementioned studies having proposed models of the mass assembly of low redshift, quiescent galaxies, I will now concentrate on the link between low and high redshift galaxies. Firstly there is a relative lack of compact, massive objects at low redshift comparable to the high redshift, compact, massive systems observed. Secondly both high redshift, compact, quiescent galaxies and low redshift, massive galaxies display similar times of formation (e.g. Daddi et al. 2005; Carnall et al. 2020). These two results led to researchers trying to connect the two galaxy types in an evolutionary sequence.

After the initial study of Daddi et al. (2005), numerous follow-up studies found similarly small sizes for larger samples of high redshift galaxies with similar stellar masses at the same cosmic epochs (Trujillo et al. 2006, 2007; Zirm et al. 2007; van Dokkum et al. 2008; Cimatti et al. 2008). Later studies investigating this size growth in more detail utilised samples spanning across multiple redshift ranges (Ferreras et al. 2009; van Dokkum et al. 2010), finding a smooth and gradual growth curve across redshift. To date, one of the most

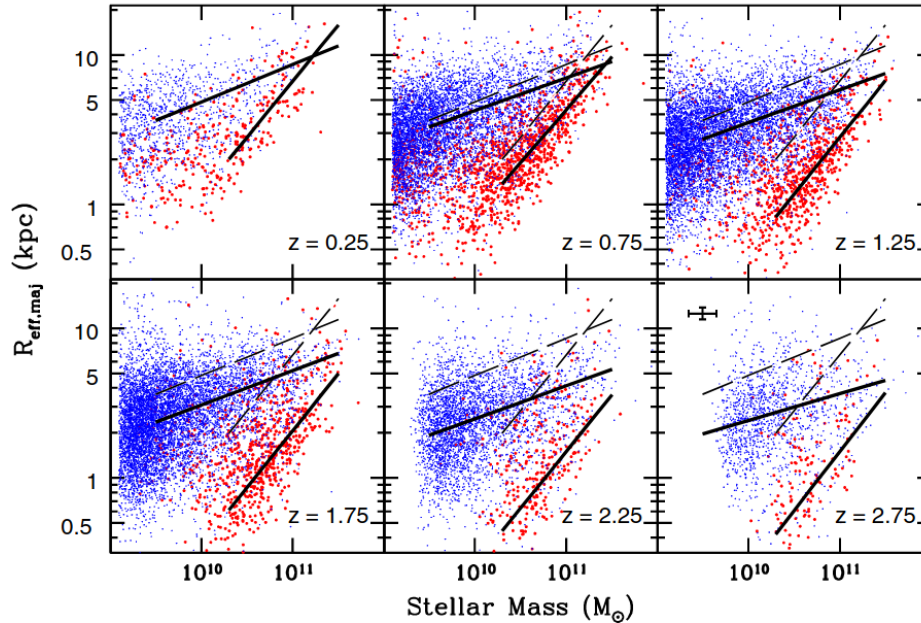


**Figure 1.2.1:** Figure 5 from [van der Wel et al. \(2014\)](#). **Top left to bottom right:** The galaxy distributions of quiescent (red points) and star-forming (blue points) galaxies in the stellar mass - size plane, in increasing redshift bins. Noticeable is the decrease in physical size with increasing redshift at fixed stellar mass, as can be seen by the solid lines which give the average trends at each epoch, compared to the dashed line which represents the  $z = 0.25$  relation.

detailed studies of the size growth of galaxies across cosmic time is that of [van der Wel et al. \(2014\)](#).

[van der Wel et al. \(2014\)](#) built upon earlier studies by extending their study to also include star-forming galaxies as well as quiescent galaxies across multiple redshift ranges. They found a similar growth behaviour across redshift for star-forming galaxies to quiescent galaxies, albeit with a shallower gradient (i.e. a size difference that is not as great between high and low redshift star-forming galaxies as for quiescent galaxies). Their results can be seen in Figure 1.2.1, where the blue and red points represent star-forming and quiescent galaxies respectively, separated into multiple redshift bins and are plotted in the size-stellar mass plane. A gradual decrease in the average size (fitted solid black lines) at constant stellar mass is observed from low to high redshift. The size difference between the highest redshift quiescent galaxies and their low redshift counterparts can amount to a factor of  $\sim 4$  ([Trujillo et al. 2007](#)) and thereby implies significant stellar density differences of up to 1 or 2 orders of magnitude greater ([van Dokkum et al. 2008](#)).

Although progenitor bias, which implies that high redshift galaxies may not necessarily be the progenitors of low redshift galaxies ([van Dokkum & Franx 2001](#)), may be used to argue that these multiple samples are not evolutionarily linked, there are arguments against this. One of these arguments is that there is a lack of compact massive galaxies in the local

universe (Trujillo et al. 2009; Valentinuzzi et al. 2010; Taylor et al. 2010), which would be expected if all of these objects evolved completely passively and without interactions. A second argument is the old average age of the stellar material in the majority of early-type galaxies in the local universe (e.g. Thomas et al. 2005, 2010), whereas a significant fraction of galaxies with young ages would be expected in the progenitor bias driven scenario. These arguments rule out progenitor bias as the sole driver of the size growth processes of massive galaxies, hence numerous physical mechanisms have therefore been suggested to account for the size evolution of massive galaxies.

Some studies argue that major mergers (stellar mass ratio  $< 1:4$ ) could increase the size of an object dramatically (Feldmann et al. 2010). In this scenario, material from both galaxies involved in the merger is significantly disturbed and displaced in such interactions. Other studies, however, state that this is likely to increase the stellar mass of an individual object too greatly (van der Wel et al. 2008; Bezanson et al. 2009), especially in the central regions of massive galaxies (Naab et al. 2009). This scenario would result in much greater numbers of extremely high mass objects than observed in the local universe and stellar mass density profiles which would be much steeper in the central regions of galaxies than observed.

Feedback from AGN is another argument proposed that could cause the size growth of such galaxies (Fan et al. 2008, 2010). In this scenario outflows and winds driven by AGN could remove gas from the galaxy and induce an expansion of the stellar component. Numerous counterarguments to this theory, however, have been presented (see Trujillo et al. 2009; Bezanson et al. 2009, and references therein). These counterarguments include that the amount of feedback would need to be extremely fine tuned to reproduce the properties of local, massive ellipticals and that the dynamically expected size-to-mass ratio increase of such a mechanism disagrees with the observed trends such as in van der Wel et al. (2014).

The theory currently favoured by the astronomical community to explain this observed size growth behaviour has emerged as the two-phase evolutionary scenario of massive galaxies (e.g. Naab et al. 2007, 2009; Oser et al. 2010, 2012). This scenario postulates that the first phase of evolution is the rapid formation of the bulk of the stellar mass through a main dissipative episode of star formation, resulting in a compact, massive object. This is followed by a secondary phase with the accretion of material onto the massive galaxy from satellite galaxies via gas-poor or "dry" minor mergers (stellar mass ratio  $\gtrsim 1:4$ ), gradually increasing the physical sizes of the central galaxies (e.g. Bezanson et al. 2009).

Simulations have provided some of the strongest evidence to date supporting the scenario that minor mergers drive the size growth of massive galaxies. Many have found a rapid build up of the bulk of the stellar mass via gas accretion, dissipation and rapid, in-situ star formation at high redshifts (from  $z = 8$  to  $z = 2$ ) for many high mass galaxies. This initial stellar mass assembly phase is followed by a relatively small increase in mass and a large increase in size, with this secondary phase coinciding with multiple minor mergers (Naab et al. 2007, 2009). Similar studies have also presented evidence that massive galaxies are made up of an increasing amount of old ex-situ material towards higher stellar masses and lower redshifts, connecting this old ex-situ material to satellite galaxies (Oser et al. 2010, 2012). The most recent studies have provided yet more evidence for this scenario, finding

that the outskirts of massive galaxies are increasingly dominated by ex-situ material delivered from satellite galaxies (Hirschmann et al. 2015; Davison et al. 2020; Remus & Forbes 2021).

Hints of minor mergers driving the growth of massive galaxies has also been found in various observational studies. Early studies showed that the surface brightness profiles at various redshifts increases the most in the outer regions of galaxies, likely driven by the accretion of ex-situ material (Hopkins et al. 2009; van Dokkum et al. 2010; Bílek et al. 2020). Other studies also find a high estimated rate of minor mergers for early-type galaxies (Ferreras et al. 2014), which is argued to be sufficient to account the growth of central galaxies below  $z \lesssim 1$  (Newman et al. 2012). Arguments such as the expected size growth to mass growth of quiescent galaxies expected by either major merger, AGN feedback or minor merger scenarios have also been invoked in order to favour the minor merger scenario (Bezanson et al. 2009; Trujillo et al. 2011), whereby major mergers provide too much mass growth and AGN feedback not enough for the expected size growth of the average galaxy. These arguments, however, are all indirect, with direct links of accreted stellar material and satellite galaxies via observations still lacking.

In order to search and study minor mergers around low redshift, massive galaxies, researchers need to target the ongoing process. The accreted stellar material from lower mass galaxies in the process of merging is usually extremely diffuse in comparison to the host galaxy, manifested in so called "Low Surface Brightness" features (LSB features) located in the outskirts of central galaxies. Extremely deep imaging is needed in order to detect a signal from such diffuse material. Studies ranging from using a number of small aperture and amateur telescopes with long exposures (e.g. Martínez-Delgado et al. 2010; Koch et al. 2017) to surveys on larger class telescopes such as the Canada-France-Hawaii Telescope (e.g. Ludwig et al. 2012; Atkinson et al. 2013; Duc et al. 2015; Morales et al. 2018) have been carried out. Such studies have successfully found signatures of the accretion of stellar material with LSB features detected down to surface brightnesses of  $\mu_{g\text{-band}} \sim 29 - 30 \text{ mag arcsec}^{-2}$  (Bílek et al. 2020; Duc 2020). Simulations also show that as imaging data go increasingly deeper, an increasing number of tidal features and distorted stellar material is revealed (Mancillas et al. 2019).

However most observational studies considering larger samples, although finding significant signs of tidal material, generally have not attempted to quantify the physical properties such as colour or stellar mass of this material. This is namely due to a lack of multi-band or multi-wavelength data that is deep enough to enable the colour of the material to be determined or SED fitting to be carried out. Properties of the material such as colour and stellar mass (as well as the prevalence of this merger activity) can help us understand its origin and thereby possibly constrain the processes driving the size evolution of galaxies via direct observations.

In summary: low redshift, massive galaxies are found to have old ages, similar to their high redshift, compact counterparts. This has led researchers to believe that compact, massive galaxies grow in size to evolve into their low redshift counterparts. This size growth has also been shown to proceed fairly steadily over cosmic time. Major mergers and AGN feedback were initially proposed as a potential physical mechanism to explain this size growth,

but have however been found to predict a different size growth scenario to observations. Hence, minor mergers have become the favoured explanation. In the minor merger scenario, satellite galaxies likely orbit their central galaxy and get accreted onto the outskirts of the central, massive galaxy, causing a large size increase of the galaxy without adding significant stellar mass. Although simulations have found evidence of these processes and there are some hints of observational evidence, a direct link has yet to be made between the tidal features and outskirts of central galaxies and the surrounding satellite population in observations.

### 1.3 The Effect of Mergers on Central Galaxies

As previously mentioned in Section 1.1, the stellar mass assembly history of galaxies correlates with certain properties of the stellar material. This means that the assembly and evolutionary history of any one galaxy is imprinted on the properties of its stellar material. One recently developed set of data is especially useful for such investigations, namely Integral Field Unit (IFU) spectroscopy. The release of data from a number of large scale, public IFU surveys over the last few years such as Mapping nearby Galaxies at Apache Point Observatory (MaNGA, [Bundy et al. 2015](#)), Sydney-AAO Multi-object Integral-field spectrograph (SAMI, [Croom et al. 2012](#)) and Calar Alto Legacy Integral Field spectroscopy Area (CALIFA, [Sánchez et al. 2012](#)) surveys to name a few, have significantly developed our understanding of many of the details of galaxy evolution on smaller scales. These surveys contain spatially resolved spectra of between hundreds and thousands of galaxies, providing, for the first time, detailed spectral data of galaxies while also containing statistically significant sample sizes.

The analysis carried out on IFU data sets covers a wide range of areas of astronomical research such as the spatially resolved kinematics of galaxies ([Cappellari et al. 2013](#); [van de Sande et al. 2017b](#)), our understanding of AGN and their ionised outflows ([Scholtz et al. 2020](#); [Wylezalek et al. 2020](#)) and star formation processes and their relation to various local scales or galaxy properties ([Sánchez et al. 2013](#); [Bluck et al. 2020](#)). These data sets have also enabled researchers to extensively investigate the stellar population properties of galaxies in higher detail than previously possible ([Martín-Navarro et al. 2018](#); [Zibetti et al. 2020](#)). Studying the stellar populations of galaxies has allowed researchers to constrain processes such as star formation and quenching in more detail across multiple epochs, with one popular method concentrating on radial gradients of certain stellar properties.

The radial gradient of a stellar population of a galaxy (i.e the change of properties such as stellar age or metallicity as a function of radius) indicates how a galaxy has formed its stars. A negative gradient in stellar age, meaning that the stars in the centre are older than those in the outskirts, indicates an inside-out scenario. This is where star formation ceases in the central regions of a galaxy earlier than the outskirts. In contrast, positive gradients may indicate an outside-in formation scenario. Similarly, negative metallicity gradients, whereby the central regions of a galaxy are more metal-rich than the outskirts, may indicate the renewal of star formation in the outskirts by metal-poor gas which is accreted onto the outskirts of the galaxy and a starvation of star formation in the central regions. This picture, however

can be complicated by other processes such as ongoing star formation bursts or mergers, especially in late-type star-forming galaxies.

In the case of a simple monolithic collapse model similar to the scenario outlined earlier, whereby a galaxy undergoes an intense, short burst of star formation to form the bulk of its stellar mass, models predict strong negative age and metallicity gradients (Carlberg 1984; Thomas et al. 1999). Galaxy merging, however, is expected to cause a flattening of these gradients in the outskirts of a galaxy or the entire profile, depending on the type of merger (Kobayashi 2004). Therefore, as star formation may proceed from different regions in galaxies and the subsequent quenching may have many possible causes, including feedback from AGN or supernovae, regulation of gas, or mergers, the analysis of radial gradients must be carried out with care.

Studies utilising low redshift IFU data sets in combination with stellar populations have generally found shallow or flat age and metallicity gradients in galaxies, albeit with some variation (Sánchez-Blázquez et al. 2014; Goddard et al. 2017a). Such studies generally agree about a smooth and fairly linear transition from slightly positive gradients at low stellar masses or line of sight velocity dispersions to slightly negative gradients at higher stellar masses or velocity dispersions (Sánchez-Blázquez et al. 2014; Goddard et al. 2017a). This indicates a likely progression of outside-in star formation and metal enrichment in lower mass galaxies before a proceeding of inside-out quenching at higher stellar masses. Caution must be taken, however, as the two processes can imprint themselves in similar ways on the same stellar population properties, meaning disentangling star formation from quenching is not straightforward.

Despite some agreement on the general radial gradients of various galaxy properties between studies, mixed results are presented on the dependence of these gradients with morphology or galaxy type among other galaxy properties. This is likely due to varying sample sizes or different sample selections. Similarly Goddard et al. (2017a) also find no significant difference in the gradients when splitting their sample by environmental density, indicating that stellar mass is the main driver of the observed trends. Further studies, however, have not been carried out to date to confirm these initial results, as such investigations are still relatively recent.

Further studies such as those of Martín-Navarro et al. (2018) and Zibetti et al. (2020) have tried to connect low redshift, massive galaxies to high redshift, massive compact objects by investigating the metallicity and age gradients of galaxies contained within CALIFA (Sánchez et al. 2012). They find negative metallicity gradients in the centre of their low redshift galaxies with a flattening towards the outskirts, indicative of a transition in the origin of the stellar material. Martín-Navarro et al. (2018) also compare the age and metallicity gradients of their sample to compact, old, relic galaxies in the local universe (similar to the high redshift, compact massive galaxies from Section 1.2), finding similar ages, metallicities and trends in these low redshift, compact objects as is expected for high redshift, compact objects. They claim that this indicates that the centres of local, massive galaxies were formed in gas-rich, rapid bursts of star formation at high redshift, producing the negative metallicity gradients, which are flattened in the outskirts by the steady accretion of material from

minor mergers over a longer time span. This result provides more support to the two-phase assembly scenario outlined in the previous sections.

Cosmological simulations have also been used to investigate the resolved properties of galaxies and their radial gradients (e.g. [Tissera et al. 2016](#); [Trayford & Schaye 2019](#)), generally finding similar trends to the observations. However, simulations also provide another advantage, in that each stellar particle can be precisely tracked throughout cosmic time within the simulation ([Schaye et al. 2015](#); [Qu et al. 2017](#)). This means that the time at which the original gas particle is converted into a stellar particle can be determined as well as the geometric position of the particle at this timestep with respect to the present-day position of the particle or the present-day host galaxy. In other words if the star is formed in- or ex-situ ([Qu et al. 2017](#); [Boecker et al. 2020](#)).

The tracking of the in- and ex-situ stellar material of galaxies has been used to great effect. For example, some studies of cosmological simulations find that higher mass galaxies contain higher fractions of ex-situ stars ([Oser et al. 2010, 2012](#); [Pillepich et al. 2018b](#)). Recently, this has been explored further, with studies such as [Davison et al. \(2020\)](#) and [Remus & Forbes \(2021\)](#) finding that the bulk of this ex-situ material is located in the outskirts of galaxies. These studies find that the centres of galaxies are, on average, dominated by in-situ stellar material with a crossover point at a certain radius, whereby the ex-situ fraction of stars is greater than the in-situ component in the outskirts of galaxies.

In their study, [Remus & Forbes \(2021\)](#) take this a step further, finding that the fraction of in- to ex-situ stars can vary, and correlates with the average merger history of the subsample. They find that a minority of galaxies display high fractions of ex-situ stars at all radii and have undergone major mergers, such as the galaxies in the two left panels of [Figure 1.3.1](#). They also find that another minority display high in-situ fractions of stars and have undergone cumulatively less mergers, however these mergers have been gas-rich. The majority of their sample, however, displays a crossover from being in-situ dominated in their central regions to ex-situ dominated in their outskirts (i.e. with increasing radius). They find that these galaxies undergo very few major mergers, instead undergoing multiple minor mergers which deliver the ex-situ stars to the outskirts of the galaxy. An example of this type of galaxy can be seen in the right-hand panel of [Figure 1.3.1](#), whereby the top panel shows the in-situ (red) and ex-situ (blue) stellar mass, the mid panel shows the relative fractions and the bottom panel shows the merger histories (with blue lines showing minor mergers and red showing major mergers). This work provides an insight that may allow researchers, observationally, to further connect the radial gradients in age, metallicity and the fractions of in- and ex-situ stellar material to a galaxy's assembly and evolution history, including the evolutionary paths of low redshift, massive, central galaxies.

## 1.4 This Work on Central Galaxies

In order to thoroughly investigate the assembly and evolutionary processes of low redshift, massive, central galaxies I will take a three step approach. I will concentrate one by one on the points of each section in this introduction, using the processes outlined above. From here

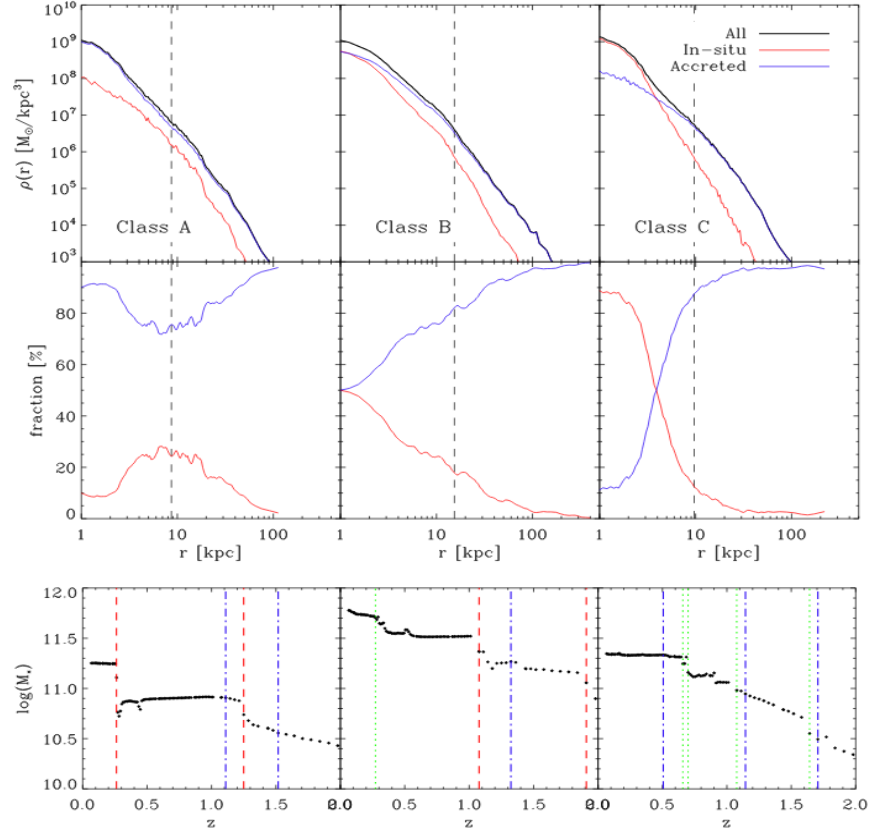


**Figure 1.3.1:** Figure 1 from [Remus & Forbes \(2021\)](#). **Top two rows of each column:** The density and fraction of in-situ (red lines) and ex-situ (blue lines) stellar material as a function of galaxy radius in certain galaxy types (3 of 6 possible categories shown here). Ex-situ dominated galaxies are presented in the first two columns and galaxies which have a turnover from being in-situ dominated in their centre, to ex-situ dominated in their outskirts in the right-hand set of panels. These galaxies with a turnover constitute the majority of galaxies in their simulation ( $\sim 72$  per cent). **Bottom row of each column:** The merger histories of these galaxy categories, with blue dot-dashed lines indicating minor mergers and red dashed indicating major mergers. The galaxies with in-situ dominated centres but ex-situ dominated outskirts have undergone more minor mergers on average, whereas ex-situ dominated galaxies have undergone at least one major merger.

on I use the pronoun "we" to reflect that although the majority of this work has been carried out by myself, there have also been contributions by various collaborators, whose specific contributions are presented at the start of each chapter.

In Part I of this research, covered by Chapters 2 and 3, we present the assembly processes of low redshift, central galaxies and how they are affected by secular and environmental effects, connecting them to high redshift, compact objects. In Chapter 2, we present our initial observational sample of central galaxies selected from the SDSS group catalogues. We also present the methods for estimating the assembly histories of our sample via the SED fitted models from the work of [Pacifci et al. \(2016\)](#). We then present the cosmological simulations used for comparing the mass assembly of central galaxies. In Chapter 3, we initially present the effect that both environmental and host galaxy stellar mass has on the assembly histories of central galaxies. We then compare the findings inferred from the observational data with the cosmological simulations before analysing which factors may be responsible for points of tension between the observations and simulations.

In Part II, covered by Chapters 4 and 5, we present a direct link between the abundant merger features of central galaxies and the surrounding satellite population, providing evidence of minor mergers driving the size growth of central galaxies. In Chapter 4, we present the deep imaging data from the Hyper Suprime-Cam (HSC) Subaru Strategic Programme (-SSP) of a sub-sample of 118 of our original galaxies, with an added comparison sample of younger galaxies. We also outline our morphological classification and then explain our processing of the imaging data and the subsequent SED fitting. In Chapter 5, we present our spatially resolved radial profiles in colour and stellar mass surface density in order to investigate and quantify the nature of the tidal features and provide the link to the satellite population. Finally, we briefly compare our results to other techniques from previous studies on the size growth of massive galaxies.

In Part III, covered by Chapters 6 and 7, we take a further sub-sample of our galaxies, observed by the SAMI IFU survey, in an attempt to constrain the effects that minor mergers may have on the evolution of these objects, imprinted in the stellar population properties and radial gradients. In Chapter 6 we present the sub-sample of galaxies with available data, followed by the stellar population modelling parameters and techniques used to estimate the age and metallicity gradients, as well as the in- and ex-situ fractions of stellar material. In Chapter 7, we present our gradients in age and metallicity and how this may depend on the morphological state of the galaxy.

A discussion of these results is given in Chapter 8, including a deeper interpretation of the trends in the assembly times due to secular and environmental effects, the direct link between the colours and stellar masses of the LSB features and the surrounding satellite population, and the effect minor mergers may imprint on the stellar population radial gradients of galaxies. This is followed by a conclusion of this research in Chapter 9, with ancillary analysis referred to throughout the paper presented in Appendix A.



*"I asked the professor why I was wasn't getting top marks. He told me the marks were good, but I should be more me and less a copy of everyone else there. It hadn't occurred to me that being me was a potential advantage. And then the penny dropped. Everyone in Oxford was bored with perfect kids from perfect schools. Being a bit northern and weird was my greatest strength. It could make me interesting. I could beat the perfect people by doing things they couldn't do."*

James Rebanks – The Shepherd's life, 2015

# 2

## Data and Methods for the Stellar Mass Assembly of Central Galaxies

We begin by considering the stellar mass assembly of low redshift, massive, central galaxies. We present the SDSS group catalogues, the catalogues and SED fitting techniques of [Pacifi et al. \(2016\)](#), the IllustrisTNG simulations, and our matching criterion between observations and simulations. This Chapter of the thesis is contained in the paper of [Jackson et al. \(2020b\)](#). Contributions by collaborators to this Chapter are as follows: Dr. Camilla Pacifi for providing her catalogue of SED fitted galaxies; Mr Christoph Engler for the collection of the IllustrisTNG data; Dr. Anna Pasquali, Dr. Annalisa Pillepich and Mr Christoph Engler for the discussion on the optimal sample selection techniques for the IllustrisTNG sample.

### 2.1 The SDSS Group Catalogues

Group catalogues are extremely useful for exploring the characteristic properties of various sub-populations of galaxies, including stellar mass assembly histories. This is due to their statistically significant sample sizes, which reduce biases introduced by outliers in host galaxy property distributions and reveal an overall and continuous picture of galaxy formation and evolution and its possible dependencies on both secular and/or environmental effects. In this section of this research we used the SDSS group catalogues of [Lim et al. \(2017\)](#) which build upon the group catalogues of [Yang et al. \(2007\)](#) to build our initial parent galaxy sample. We give a brief outline of the catalogues here: A full description of the entire catalogues and techniques can be found in the paper of [Lim et al. \(2017\)](#).

The group catalogues of [Lim et al. \(2017\)](#) use data from the SDSS Data Release 13 (DR13, [Albaret et al. 2017](#)), which improves on the DR7 ([Abazajian et al. 2009](#)) used in the group

catalogues of [Yang et al. \(2007\)](#). Two of the main improvements are in the photometry, which implements refined reduction of the raw data and uses updated zero-points, and the multi-object spectroscopy, which obtains spectroscopic redshifts for some objects that were missed in DR7 due to fibre collisions. [Lim et al. \(2017\)](#) also use an improved Friends-of-Friends (FoF) algorithm to link galaxies to their parent haloes. This has been compared to [Yang et al. \(2007\)](#), with no significant differences in the majority of groups, however better constraints on the halo masses of groups with low numbers of galaxies.

Stellar masses for each galaxy are initially derived using an approximation from [Bell et al. \(2003\)](#), based on the  $g$  and  $r$  colours and  $r$ -band magnitude. Each galaxy is then treated individually while the algorithm estimates corresponding halo masses based on the derived stellar masses. These halo masses are generated from mock catalogues from the EAGLE simulation ([Schaye et al. 2015](#); [Crain et al. 2015](#)), which assumes a Lambda Cold Dark Matter ( $\Lambda$ CDM) cosmology and returns dark matter halo profiles consistent with [Navarro, Frenk & White \(1997, NFW\)](#) profiles. Line-of-sight velocity dispersions ( $\sigma_{\text{LoS}}$ ) and halo radii ( $r_{180}$ , the radius of the halo where the mean mass density is 180 times the mean density of the Universe) are then estimated based on relations with the halo mass. A probability function of any two galaxies belonging to the same parent halo is derived using  $\sigma_{\text{LoS}}$  and  $r_{180}$  and is then compared to a background probability in order to cut any galaxies that are not likely to belong to the group. We note that there is no distinction made between groups and clusters in these catalogues.

Final halo masses are then calculated as follows: For groups with more than one member, the GAP correction of [Lu et al. \(2015\)](#) is applied. This uses the luminosity difference between the brightest galaxy assigned to the group and then  $n^{\text{th}}$  nearest neighbour. For galaxies without companions, halo masses are estimated either using galaxy luminosity or stellar mass. We use the luminosity derived halo masses, which are derived from the relation between luminosity and halo mass yielded by the EAGLE simulations, defined as the total mass contained within a sphere where the density is 180 times the mean density of the Universe. [Lim et al. \(2017\)](#) state that the typical uncertainty of these estimations is  $\sim 0.2$  dex. For the purposes of this analysis, we scaled the halo masses using the same cosmological parameters as in IllustrisTNG300 (TNG300) for consistency between the observational data and simulations, whereby  $h = 0.6774$  and  $\Omega_{\text{m}} = 0.3089$  ([Planck Collaboration et al. 2016](#)). It should be noted, however, that for all that concerns the shape and properties of the stellar-to-halo mass relations of the SDSS and TNG300 data, differences may arise because of modeling differences between the EAGLE and the TNG300 simulations and do not necessarily reflect failures of one or the other with respect to reality, which we cannot assess.

In order to obtain further galaxy properties that were not contained in the [Lim et al. \(2017\)](#) catalogues, we cross-matched the sample with the New York University value-added catalogue of SDSS galaxies presented in [Blanton et al. \(2005\)](#) and the [Yang et al. \(2007\)](#) group catalogue, using the SDSS identification number. We then obtained properties such as the Malmquist bias weightings, which account for the sensitivity of the survey, allowing us to correct any average galaxy properties for galaxies that fall under the survey limits (see [Yang et al. 2007](#), and references therein) and the Sérsic index (obtained by fitting az-

imuthally averaged surface brightness profiles), which provides an indicator for the characteristic galaxy morphology. All observational values presented here forth are corrected for these bias weightings.

To link the star forming histories back to present-day properties such as halo mass, we then further cross-matched the catalogues with those of [Pacifci et al. \(2016\)](#), presented in more detail below in Section 2.2) using a matching radius of 5 arcsec. This reduces the likelihood of miss-matches while still allowing for small differences in the astrometry. We retrieved better constrained estimations of the stellar mass from the photometric SED fitting method of [Pacifci et al. \(2016\)](#), described in Section 2.2) than those in the other group catalogues, hence these are the stellar masses referred to hereafter. We also used the specific star formation rates (sSFR) estimated by the photometric SED fitting and the  $g$  and  $r$  magnitudes used by [Pacifci et al. \(2016\)](#) for consistency in our analysis.

We finally applied a cut in halo mass of  $M_{\text{Halo}} > 10^{12} M_{\odot}$  and selected only central galaxies in their respective groups. This halo mass cut was chosen as below this value the halo mass estimates display increasingly significant uncertainties. Our final sample, hereafter referred to as our SDSS sample, contains 89,647 galaxies, of which 12,663 have companions according to the group catalogues and are hereafter referred to as group environments and 76,984 are without a companion, hereafter referred to as field galaxies. The sample spans a redshift range of  $z = 0 - 0.13$ . We characterise this sample in Figure 2.1.1, where galaxy properties are plotted in 0.1 dex bins of stellar and halo mass.

By splitting our sample into bins with a size of 0.1 dex in both stellar mass and halo mass and calculating the (Malmquist weighted) properties for each bin, we can reveal any trends in the data. This binning allows us to simultaneously control for both secular processes, of which stellar mass is a proxy, and environmental processes, of which halo mass is a proxy. This enables us to highlight how secular and environmental processes can shape the evolution of a specific galaxy population, imprinted in their characteristic present-day properties and average evolutionary sequences.

The top left-hand panel of Figure 2.1.1 shows the logarithm of the number of galaxies per bin of stellar and halo mass. As could be expected, those bins in the centre of the distribution contain the highest number of galaxies ( $\gtrsim 1000$  galaxies per bin) with the edges of the distributions containing the least ( $\sim 10$  galaxies per bin). The top right-hand panel shows the mean amount of satellites within the parent halo (as determined by the modified FoF halo finder algorithm from [Lim et al. 2017](#)). The most massive galaxies ( $M_{\text{Stellar}} \gtrsim 10^{11} M_{\odot}$ ) in the most massive haloes ( $M_{\text{Halo}} \gtrsim 10^{13.5} M_{\odot}$ ) in our sample have the most satellites.

The mean aperture size used in the photometry from [Pacifci et al. \(2016\)](#) divided by the SDSS effective radius from [Blanton et al. \(2005\)](#) is plotted in the mid left panel. We see that most galaxies use an aperture of 1.9 effective radii with no obvious trend in halo or stellar mass, except for a sub-sample ( $M_{\text{Stellar}} \sim 10^{11} M_{\odot}$ ,  $M_{\text{Halo}} \sim 10^{12} M_{\odot}$ ) which have  $\sim 0.3R/R_e$  smaller aperture sizes, showing any trends in further analysis are unlikely to be biased by aperture variations in each bin. In the mid right panel we compute the mean Sérsic index (mid left panel) in order to give an indication of the average morphology of each bin. Similar to previous studies, we find that galaxies with greater stellar masses have,

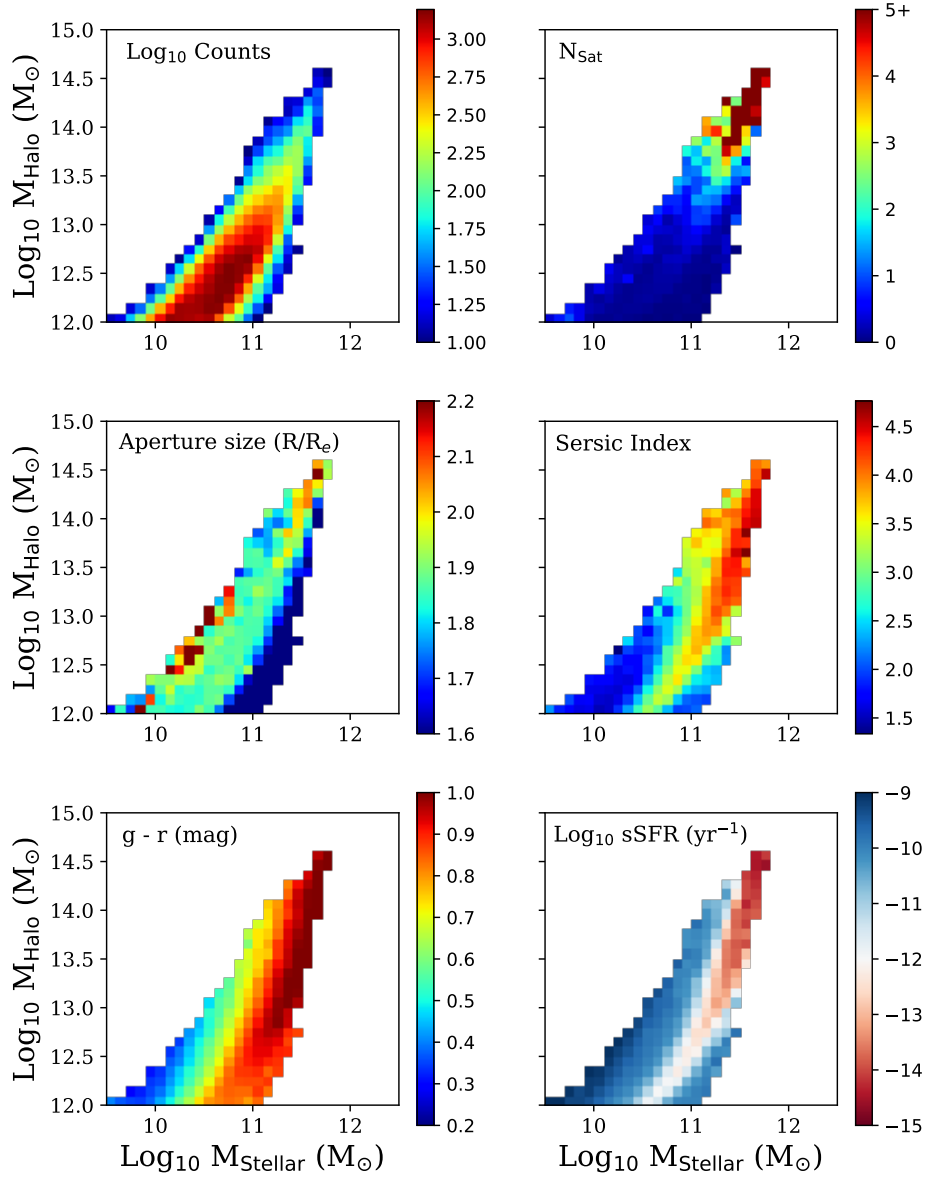


**Figure 2.1.1:** The average properties of our SDSS galaxy sample per bin in both stellar and halo mass. **Top left to bottom right:** The logarithm of the counts of galaxies, the average number of satellites ( $N_{\text{Sat}}$ ), the ratio of the radius in which the photometry was measured to the effective radius, the average Sérsic index, the mean  $g - r$  colour and the sSFR estimated from the SED fitting of [Pacifiçi et al. \(2016\)](#).

on average, higher Sérsic indices, with the exception of a sub-sample ( $M_{\text{Stellar}} \sim 10^{11}M_{\odot}$ ,  $M_{\text{Halo}} \sim 10^{12}M_{\odot}$ ) which show lower Sérsic indices at higher stellar masses for constant halo mass. We also see subtle halo mass dependencies, whereby in galaxies with stellar mass  $M_{\text{Stellar}} < 10^{11}M_{\odot}$ , at constant stellar mass but with higher halo masses have, in general, lower Sérsic indices.

The bottom left panel shows the mean  $g - r$  colour from the photometry used by [Pacifci et al. \(2016\)](#). We see that the average colour of a galaxy correlates heavily with the stellar mass, however similar to the Sérsic index there is a slight halo mass dependence at stellar masses  $M_{\text{Stellar}} < 10^{11}M_{\odot}$ . A galaxy of the same stellar mass in a more massive halo is, on average, bluer in this regime. The bottom right panel shows the mean sSFR as determined from the SED fitting of [Pacifci et al. \(2016\)](#). The behaviour correlates in the same way as the Sérsic index, as a strong function of stellar mass, however with a secondary halo mass dependency below  $M_{\text{Stellar}} < 10^{11}M_{\odot}$ , whereby galaxies with the same stellar mass but in more massive haloes have higher sSFRs. We also see an exception in a sub-sample of galaxies with  $M_{\text{Stellar}} \sim 10^{11}M_{\odot}$  and  $M_{\text{Halo}} \sim 10^{12}M_{\odot}$ , which have higher sSFRs than less massive galaxies at constant halo mass.

## 2.2 The Photometric SED Fitting Process of [Pacifci et al. \(2012\)](#)

In their paper, [Pacifci et al. \(2016\)](#) carried out photometric SED fitting on a large sample of galaxies ( $\sim 230,000$ ) from the SDSS. This catalogue of galaxies includes estimates of the assembly times (i.e. the formation time of both in- and ex-situ stars) of 10, 50 and 90 per cent of the stellar mass ( $t_{10}$ ,  $t_{50}$ ,  $t_{90}$ ) as well as estimates of the Star Formation Rate (SFR) and stellar mass of each galaxy. A full description of the SED fitting process can be found in [Pacifci et al. \(2012\)](#) and [Pacifci et al. \(2016\)](#), however we provide a brief outline here.

[Pacifci et al. \(2016\)](#) initially take photometry in 4 optical bands from the SDSS DR10 ([Ahn et al. 2014](#)):  $g$ ,  $r$ ,  $i$  and  $z$  (with central wavelength,  $\lambda_c$ : 4770 Å, 6231 Å, 7625 Å and 9134 Å), excluding the  $u$ -band due to systematic differences of 0.1 mag compared to the model library (see [Pacifci et al. 2016](#), for more details). The SDSS Petrosian radius is used to measure the photometric fluxes and has a median aperture of 5 arcsec, with 16<sup>th</sup> and 84<sup>th</sup> percentiles of 3.8 and 7.8 arcsec. In order to more accurately constrain the stellar masses, SFRs and the SFHs, photometry was added in the ultraviolet from *GALEX*: the far-ultraviolet ( $\lambda_c \sim 1550$  Å) and the near-ultraviolet ( $\lambda_c \sim 2200$  Å), and in the infra-red from *WISE*: *W1* ( $\lambda_c = 3.4\mu m$ ). A 3 arcsec matching radius was applied between surveys.

All data were corrected for foreground extinction using the dust maps of [Schlafly & Finkbeiner \(2011\)](#) and the extinction law of [Fitzpatrick \(1999\)](#), except for *W1*, where the reddening is assumed to be negligible. The redshifts required for the SED fitting process were obtained from optical fibre spectroscopy from the SDSS DR10. [Pacifci et al. \(2016\)](#) also exclude any type 1 AGN, which are expected to significantly affect the shape of the SED, by using the emission line catalogue of [Oh et al. \(2011\)](#). [Pacifci et al. \(2016\)](#) state they do not exclude type 2 AGN as previous studies argue that continuum emission from these objects does not affect the estimates of the physical parameters derived from optical

photometric fits (Kauffmann et al. 2003).

Individual galaxies within a wider sample can undergo an extremely wide range of evolutionary histories, which in turn affects their SFH. This SFH is reflected in the shape of the expected SED, implying that a wide variety of SFHs needs to be constructed to compare to the observed photometry, in order to cover a wide range of possible evolutionary histories. The library of SFHs used in Pacifici et al. (2016) is built from the Millennium Simulation (Springel et al. 2005) post-processed with the semi-analytic models (SAMs) from De Lucia & Blaizot (2007). These SFHs contain a number of different star formation scenarios (e.g bursty, smooth, declining etc.) and account for a number of different metal enrichment histories.

These models are then combined with the empirical stellar population synthesis models from Bruzual & Charlot (2003). Nebular emission is computed using CLOUDY (Ferland et al. 1998, 2017) and dust attenuation models account for internal reddening, including both spatial distribution and orientation uncertainties, via an implementation of Charlot & Fall (2000). The final full library contains around 1.5 million corresponding SED models.

A Bayesian method is then applied to match the observed photometry of any one galaxy to the SED models. The weighted likelihood of all possible models is used to construct a probability distribution (with median, 16<sup>th</sup> percentile and 84<sup>th</sup> percentile values) for host galaxy properties such as the stellar mass and SFR averaged over the last 10 Myr. The SFH, however, is calculated from the weighted 10 best model fits to significantly reduce computational time, this then yields the  $t_{10}$ ,  $t_{50}$  and  $t_{90}$  values. We note that the SED fitting does not depend on the steepness of the stellar mass - halo mass relation and does not depend on the SAMs used (Pacifici et al. 2012), hence differences in the analysis should not be biased by these factors.

The mean uncertainties on the assembly times range from 0.3 Gyr for  $t_{90}$  to up to 0.9 Gyr for  $t_{10}$ , with mean uncertainties on the stellar mass and SFR estimations of 0.1 and 0.5 dex respectively. Pacifici et al. (2016) state that although a wider range or the full library of models could be used to generate better constrained probability distributions for the SFHs, the difference in the precision compared to using the 10 best-fitting models does not justify the significant increase in computational time needed.

As our SDSS sample is distributed between  $0 < z < 0.13$ , each lookback time is not the expected  $z = 0$  value. We calculate the luminosity distance based on the redshift and apply a correction to the lookback time, to bring these values into line with those expected as if each galaxy was observed at  $z = 0$ . This provides a uniformity over the observational sample and allows an easier comparison with the simulations, as described in the next section.

Further checks of these catalogues and possible biases are presented in Appendix A.1.

## 2.3 The Illustris TNG Simulation Suite

Cosmological simulations have recently progressed to the stage where they can re-produce multiple properties of the observed universe to a significant degree of detail and accuracy.

Some of the numerous examples include the reproduction of the stellar mass function, Hubble sequence of morphologies, colour bi-modality, star-forming main sequence, AGN galaxy properties etc. (Schaye et al. 2015; Furlong et al. 2015; McAlpine et al. 2017; Trayford et al. 2017; Scholtz et al. 2018; Pillepich et al. 2018a; Springel et al. 2018; Genel et al. 2018; Jackson et al. 2020c). As our observational sample contains  $\sim 90,000$  galaxies, IllustrisTNG provides the advantage of having a comparable sample size after matching in their 300 cMpc simulational run compared to other similar simulations which have sizes of 100 cMpc such as EAGLE or HORIZON-AGN (Dubois et al. 2014), while still including a reasonable baryonic particle resolution of  $1.1 \times 10^7 M_{\odot}$  for tracking the relevant astrophysical processes for this research.

IllustrisTNG is a suite of magnetohydrodynamical simulations (Pillepich et al. 2018b; Marinacci et al. 2018; Springel et al. 2018; Nelson et al. 2018; Naiman et al. 2018) which build upon the original Illustris simulations (Vogelsberger et al. 2014a,b; Genel et al. 2014) while trying to address and improve on points of tension with observations (Nelson et al. 2015). It includes a number of different simulation boxes (50 co-moving Mpc, 100 cMpc and 300 cMpc per side), and dark-matter-only counterparts. The simulation uses the AREPO moving mesh code (Springel 2010), which utilises an adaptive Voronoi tessellation to solve the ideal magnetohydrodynamical equations and TreePM to solve the coupled equations of self-gravitation at discrete timesteps. Galaxy groups are identified using a FoF algorithm, with galaxies identified using the SUBFIND algorithm (Springel et al. 2001) and connected in each timestep using merger trees.

IllustrisTNG includes schemes to account for a number of astrophysical processes including some that take place below the resolution limit of the simulations, i.e. the sub-grid physics. This covers gas radiative processes featuring multiple heating and cooling mechanisms as well as star formation given by a pressure dependent law according to the models of Springel & Hernquist (2003). Stellar evolution and chemical enrichment are governed by yield tables and stellar, supernova and AGN feedback are included (see Pillepich et al. 2018a, and references therein). One of the main refinements in IllustrisTNG compared to the original Illustris simulations is the implementation of a different AGN feedback scheme. This includes both a thermally injected mode (at high Eddington accretion ratios) and a kinetically injected mode (at low Eddington ratios, see Weinberger et al. 2017).

The sub-grid physics choices are made so that specific relations are approximately consistent with observations. These include the galaxy stellar mass function, the galaxy stellar mass - size relation, the stellar mass - black hole mass relation and the halo gas fraction versus halo mass at  $z = 0$  as well as the cosmic star formation rate density evolution.

These improvements in the physics and sub-grid physics yield a better reproduction of a number of observables than the original Illustris simulations, even without specific calibration. Pillepich et al. (2018b) showed that IllustrisTNG reproduces galaxy sizes and the stellar mass function more accurately, especially at lower stellar masses. They also showed that the stellar-to-halo mass relation is more consistent with other semi-empirical findings and that the gas fraction-to-halo mass relation is in better agreement with X-ray inferences above a halo mass of  $\sim 10^{13} M_{\odot}$ . Nelson et al. (2018) showed that IllustrisTNG reproduces

the colour bi-modality to a better degree than the original Illustris, and [Springel et al. \(2018\)](#) showed that the clustering of red versus blue galaxies is also consistent with observations at  $z \sim 0$ .

## 2.4 The Selection of the Simulated Sample

Comparing observations to simulations is advantageous in such studies for a number of reasons: Simulations can track the entire stellar material of galaxies throughout cosmic time, allowing for a full construction of the star formation and mass assembly histories ([De Lucia & Blaizot 2007](#)). Therefore, by comparing trends in both data sets, we can improve the modelling within simulations, leading to more accurate predictions. We can also use simulations to better constrain and estimate the physical processes driving the evolution of galaxies. However, when employing these sorts of techniques, a deep level of matching is needed and a realisation of the limits for both observations and simulations needs to be clearly acknowledged in order to avoid over-interpreting results.

Hence, to be able to make a meaningful comparison between observations and simulations, we first need to select the samples of galaxies in the considered data sets as similarly as possible. Second, the galaxy properties from the simulated data need to be computed in as similar a way as possible to how they are inferred from the observational data. If the two data sets are unmatched then biases in either data set cause a comparison to be of little worth and the possibility that results appear completely different. A number of possible matching or selection techniques are in volume, stellar mass, redshift or flux. Some of these options, along with their possible impact on our results, are discussed further in [Appendix A.2](#).

In this research, we use the publicly-available data from the largest simulation box ([Nelson et al. 2019](#)) with the best resolution at this level, TNG300-1 (hereafter TNG300), in order to obtain a simulated sample with a comparable number of galaxies to the SDSS set and thereby reduce volume-driven biases. We use the  $z = 0$  snapshot from the TNG300<sup>1</sup> and apply a cut in halo mass, computed as the total mass of all particles enclosed in a sphere whose mean density is 200 times the mean density of the universe, to all galaxies of  $M_{\text{Halo}} > 10^{12} M_{\odot}$ . We note that although this radius is not 180 times the mean density which is used for the observations, it is the closest match in the TNG catalogues, and that using subtly different halo mass definitions has a minimal effect on later results.

This yields 46,241 central galaxies, hereafter our TNG300 galaxy sample, seen in [Figure 2.4.1](#). We also note that although the FoF halo finders used for the simulations and the observational group catalogues are not exactly the same, such as the designation of the central galaxy in a halo being the most luminous member of the assigned group in the observations compared to the most massive in the simulations. We proceed by assuming that the algorithms should provide similar results as they are based on the same basic concepts, and any minor errors should not significantly impact trends in the data as we expect this to be mitigated by binning in both stellar and halo mass. A thorough test of this, however, is beyond the scope of the research presented here.

<sup>1</sup>We correct SDSS stellar assembly times to bring them in line with expectations at  $z = 0$ , see [Section 2.2](#)

The majority of the SDSS photometry used in [Pacifci et al. \(2016\)](#) was measured within approximately two effective radii (hereafter  $2 R_{\text{eff,SDSS}}$ , see [Figure 2.1.1](#)), hence we choose to use this as our matching criterion for the simulations. Although the photometry apertures are not uniform and there is a slight scatter, we do not expect this to impact significantly on the results and trends we see. We take the available aperture of  $2 R_{\text{half-mass}}$  in TNG300 (in three dimensions) to calculate the majority of our values. We stress at this point that we are making the assumption that  $R_{\text{half-mass}}$  and  $R_{\text{eff,SDSS}}$  are equivalent, which although not exact ([Suess et al. 2019](#); [Pillepich et al. 2019](#)) is not expected to significantly impact our results. All measurements from the simulation are hereforth within the three-dimensional stellar half-mass radius ( $2 R_{\text{half-mass}}$ ).

As explained in [Section 2.2](#), the  $t_{10}$ ,  $t_{50}$  and  $t_{90}$  times for the observational data are calculated from the weighted 10 best-fitting SFHs. These SFHs are also weighted by the initial stellar birth mass. In order to create the best comparison possible, we considered all the present-day stellar particles in each TNG300 galaxy within  $2 R_{\text{half-mass}}$ . We then used the formation times of each stellar particle weighted by the initial stellar birth mass of each particle (the same as the observations) to construct a profile of the cumulative initial stellar mass at birth as a function of time for each galaxy in the simulation. From these profiles we calculated the corresponding  $t_{10}$ ,  $t_{50}$  and  $t_{90}$  times for each galaxy in our simulated sample.

We also retrieve the stellar masses which are calculated from the combined mass of all stellar particles within  $2 R_{\text{half-mass}}$ , and are re-scaled according to [Pillepich et al. \(2018a\)](#) to account for biases caused by the lower resolution limit of the simulation with a 300 cMpc box size (TNG300) compared to the simulation with higher resolution with a 100 cMpc box (TNG100). We compute the SFR averaged over the last 10 Myr ([Donnari et al. 2019](#)) within  $2 R_{\text{half-mass}}$ . This provides a comparable estimation to the observations, which are also averaged over 10 Myr. In their study [Donnari et al. \(2019\)](#) show that resolution has no significant effect on the SFRs, therefore no re-scaling of the SFRs due to resolution is needed. Colours, namely the  $g$  and  $r$  magnitudes, are calculated by summing the luminosity of all stellar particles belonging to that galaxy within  $2 R_{\text{half-mass}}$ . We also convolve all simulational values with the uncertainties in the observational results to better represent the simulational data.

A comparison of the final distributions in stellar versus halo mass of the observational sample and simulated sample can be seen in [Figure 2.4.1](#). We highlight again that SDSS galaxies halo mass estimates are generated from mock catalogues of the EAGLE simulation and therefore no conclusions can be derived here regarding the level of realism of the TNG300 model in relation to the overall shape of its stellar-to-halo mass relation. [Figure 2.4.1](#) shows that the distributions in halo masses are similar, however our sample from IllustrisTNG has a slightly different stellar mass distribution, compared to our observational sample. These differences however are small at the most massive end ( $< 100$  galaxies with  $M_{\text{Stellar}} \gtrsim 10^{12} M_{\odot}$ ) and should be somewhat accounted for by binning in both stellar and halo mass, minimising the impact on the average trends presented and the resulting conclusions drawn later in this work.

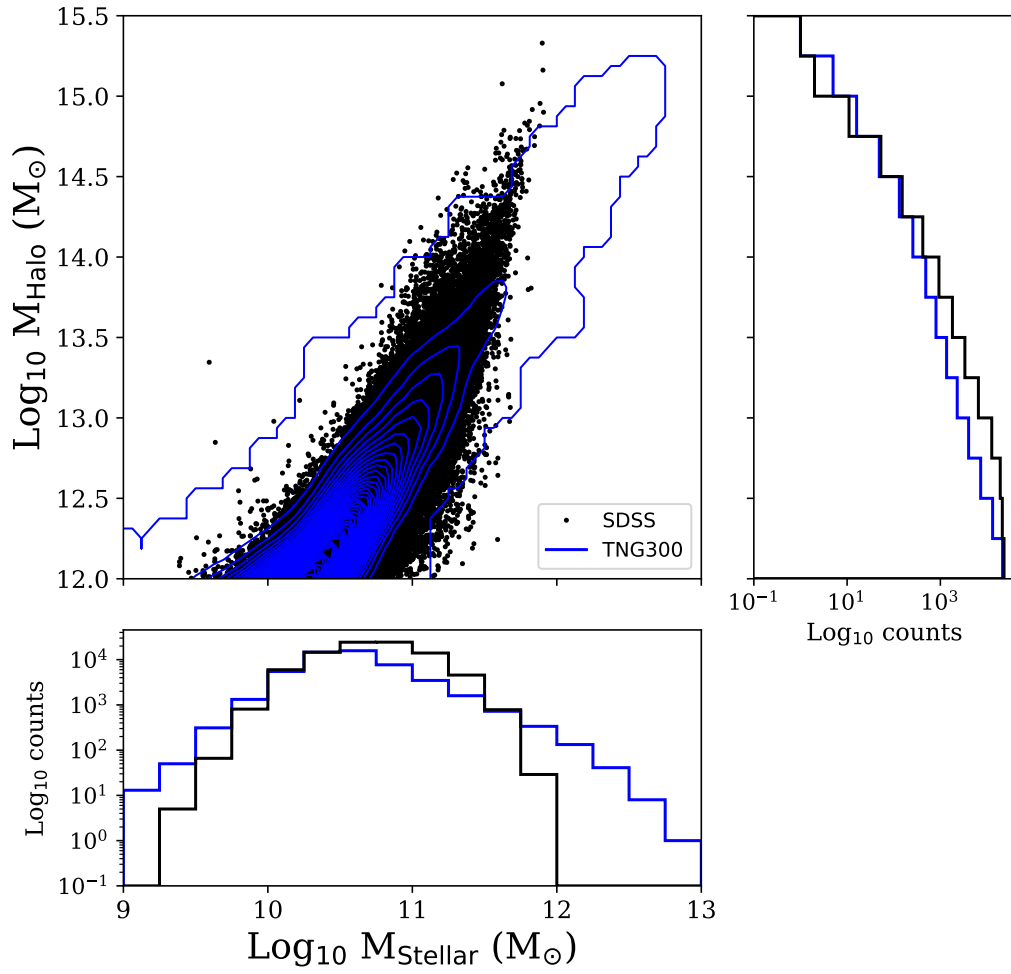


**Figure 2.4.1: Central panel:** The distributions in stellar mass versus halo mass for our SDSS observational sample (black points) compared to the simulated sample from TNG300 (blue contours). **Sub-panels:** The respective distributions in log-space of the two samples in stellar and halo mass in their corresponding colours.

*"Neither high-born nobleman, knight or esquire was here; but many of these humble sons of the hills had a consciousness that the land, which they walked over and tilled, had for more than five hundred years been possessed by men of their name and blood."*

William Wordsworth – A guide through the district of the lakes in the north of England, 1810

# 3

## Results I - The stellar mass assembly of central galaxies in SDSS and TNG

With our sample of SDSS group catalogue galaxies selected and a matched simulation sample, we now present the results of this section of the thesis. Here we present the stellar mass assembly times and trends of both the observed and simulated sample, the similarities and differences in the times and trends between observations and simulations and a further exploration of the simulations and observational sub-samples. This Chapter of the thesis is contained in the paper of [Jackson et al. \(2020b\)](#). Contributions by collaborators to this Chapter are as follows: Dr. Anna Pasquali, Mr Christoph Engler, Dr. Annalisa Pillepich, Dr. Camilla Pacifici and Prof. Eva Grebel for the discussion of tests and plots throughout and the discussion of results.

### 3.1 The Average Assembly Times of SDSS and TNG300 Galaxies

To compare at which epochs our observational and simulated samples assembled most of the stellar mass in their inner regions and how environmental and secular processes may shape these processes, we initially investigate the stellar mass assembly times. As outlined in Section 2.2, the SED fitting process yields estimations for the lookback time at which each galaxy in our observational sample formed 10, 50 and 90 per cent of its stellar mass in the SDSS sample. Like in Figure 2.1.1, we bin in 0.1 dex bins of stellar and halo mass. The results are presented in Figure 3.1.1.

We also test how well TNG300 reproduces the assembly of 10, 50 and 90 per cent of the stellar mass as a function of present-day stellar and halo mass by applying the same binning procedures as for the observational data, to provide a like-for-like comparison: results are

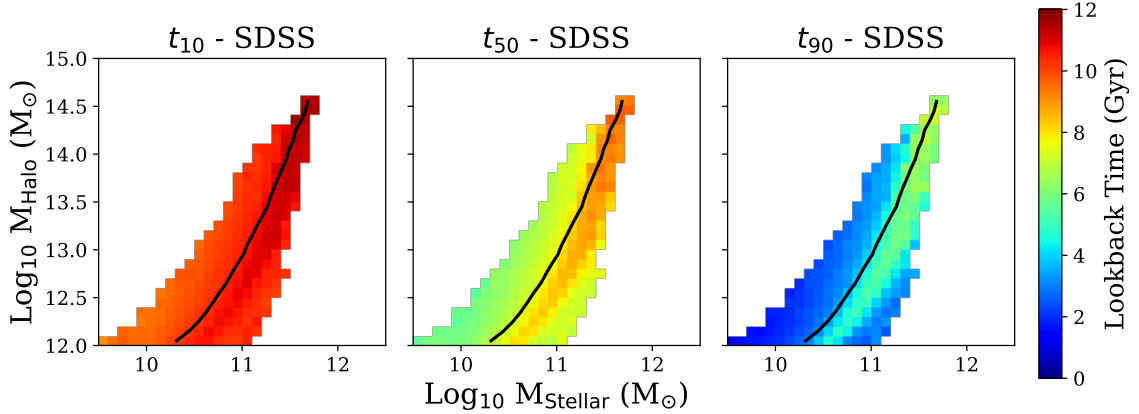


**Figure 3.1.1: Left to right:** The mean lookback times at which 10%, 50% and 90% of the stellar mass was assembled for our SDSS sample of central galaxies at  $z = 0$  in bins of halo and stellar mass. The colour bar gives the lookback time at which these percentages were formed. Going from the left to right of each distribution, we initially see clear downsizing behaviour, whereby more massive galaxies assembled specific percentages of their stellar mass at earlier times. An exception to this trend is a sub-population in the bottom right of the distribution which can be seen to display the opposite trend, i.e. more massive galaxies at fixed halo mass with younger ages. The solid black lines give the median stellar-to-halo mass relation of the sample.

given in Figure 3.1.2.

Figure 3.1.1 shows the mean lookback times at which 10 (left-hand panel), 50 (central panel) and 90 (right-hand panel) per cent of the stellar mass was assembled. We see that the range of assembly times in  $t_{10}$  is relatively small, ranging from 10 Gyr to 12 Gyr. This range increases as we move to  $t_{50}$  (6 - 9 Gyr) and to  $t_{90}$  (2-6 Gyr). There is also a strong dependency of the lookback times on stellar mass, whereby holding the halo mass constant (i.e going from left to right) we observe, on average, a clear case of downsizing. This is in line with previous studies of galaxy assembly (see e.g. Thomas et al. 2005; Gallazzi et al. 2005; Pasquali et al. 2010; Pacifici et al. 2016), whereby massive galaxies form a certain percentage of their stars earlier than less massive galaxies. We also see, however, a simultaneous dependency on the halo mass, whereby galaxies at constant stellar mass (below a stellar mass of  $10^{11} M_{\odot}$ ) but with higher halo masses, display on average younger lookback times, especially  $t_{50}$  and  $t_{90}$ . This reflects the behaviour seen in the sSFRs and Sérsic indices from Figure 2.1.1.

A sub-sample ( $\sim 2$  per cent of our SDSS sample), located in the bottom right corner of the distribution, seems to contradict hierarchical mass assembly behaviour. These galaxies have the highest stellar-to-halo mass ratios ( $M_{\text{Stellar}} \sim 10^{11} M_{\odot}$  and  $M_{\text{Halo}} \sim 10^{12} M_{\odot}$ ), and have younger ages than some less massive galaxies at constant halo mass. This is the same sub-sample which have low Sérsic indices and raised sSFRs in Figure 2.1.1. We investigate this sub-population further in later sections and discuss these results in Section 8.1.1.

We see that the average assembly times are, in general, fairly well reproduced by TNG300, as seen in Figure 3.1.2. Our TNG300 sample generally predicts similar times for the assembly of 10 (left-hand panel), 50 (central panel) and 90 (right-hand panel) per cent of the stellar

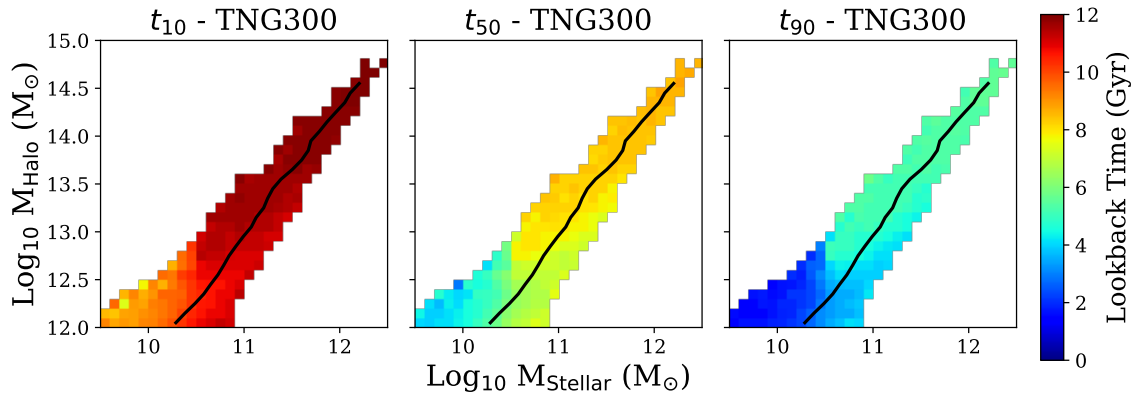


**Figure 3.1.2: From left to right:** The mean assembly times at which 10%, 50% and 90% of the stellar mass was assembled for our TNG300 sample of central galaxies at  $z = 0$  in bins of present-day halo and stellar mass. The colour bar gives the lookback time at which these percentages were formed. The simulation predicts lookback times, in general, that are similar to the observations, however it predicts a different overall behaviour with respect to halo and stellar mass than the observations. The solid black lines give the median stellar-to-halo mass relation of the sample.

mass across most stellar and halo masses. There are some subtle differences, such as at the lowest stellar masses ( $M_{\text{Stellar}} \sim 10^{10} M_{\odot}$ ) in the  $t_{10}$  and  $t_{50}$  times, which tend to be different by  $\sim 0.5 - 1$  Gyr, however these are still within the observational uncertainties. We also see that although the most massive objects in general formed early on in TNG300, the same as in the observations, a significant fraction of the oldest assembled objects appear to have intermediate stellar and halo masses ( $M_{\text{Stellar}} \sim 10^{10.5} M_{\odot}$  and  $M_{\text{Halo}} \sim 10^{13} M_{\odot}$ ). This is in qualitative disagreement with our observational results, where these objects usually have some of the youngest assembly times. These differences in the lookback times can be up to 2-3 Gyr, well outside of the observational errors. We discuss these differences in more detail in further sections.

## 3.2 The Differences in the Lookback Times between SDSS and TNG300

Having qualitatively presented the stellar assembly times of both our SDSS and TNG300 samples in Section 3.1, we now attempt to quantify and compare some of these results. In order to do this we first compare trends in either halo or stellar mass to see how well TNG300 reproduces the SDSS data if only one variable is considered. This is presented in the top row of Figure 3.2.1. The trends of  $t_{10}$ ,  $t_{50}$  and  $t_{90}$  as a function of stellar mass alone are in left-hand panel and halo mass alone in the right-hand panel. The solid lines give the medians of the SDSS data with 16<sup>th</sup> and 84<sup>th</sup> percentiles given by the shaded area and the dotted lines give the median of the TNG300 sample. We see that the trends in the observational sample can be fairly well reproduced by the simulation, as the simulated values are mostly within

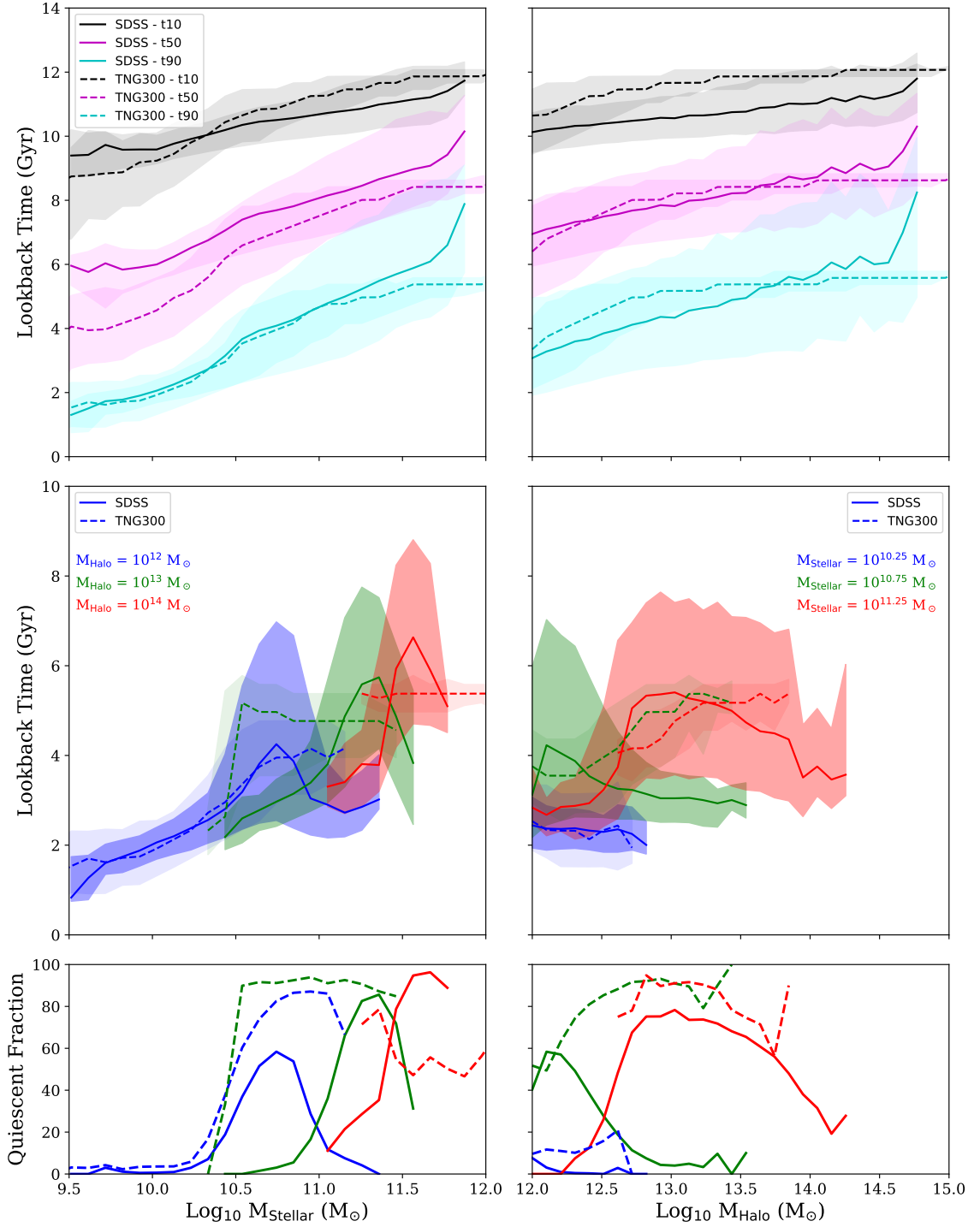


**Figure 3.2.1:** **Top row:** The  $t_{10}$  (black),  $t_{50}$  (magenta) and  $t_{90}$  (cyan) times for our observational sample (solid line) compared to TNG300 (dashed) as a function of stellar mass (left panel) and halo mass (right panel). We see generally good agreement, whereby TNG300 is mostly within the scatter of the observational distribution. **Middle row:** The  $t_{90}$  lookback times as a function of stellar mass (left panel) and halo mass (right panel), split into three different halo/stellar masses. When we account for both halo and stellar mass we see disparities between the observations and simulations, especially at intermediate values. **Bottom row:** The fraction of galaxies that are quiescent ( $\text{Log}_{10} \text{sSFR} < -11 \text{ Gyr}^{-1}$ ) as a function of stellar and halo mass, split into bins in halo/stellar mass as above.

the scatter of the observational sample at almost all stellar and halo masses. We also, once again, see downsizing, whereby less massive galaxies have younger  $t_{10}$ ,  $t_{50}$  and  $t_{90}$  values as a function of both stellar and halo mass. Comparing the top left panel to the top right panel, we see that these trends tend to be stronger (represented by the steeper gradients) in stellar mass than in halo mass for all lookback times. We also note an increase in the scatter of the distributions from an average of  $\sim 2$  Gyr in  $t_{10}$  to  $\sim 4$  Gyr in  $t_{90}$ , as seen above in Section 3.1.

To quantify the effect that accounting simultaneously for stellar and halo mass has on any comparison, and thereby highlighting tensions between the simulations and observations, we took 3 different samples at low ( $M_{\text{Halo}} = 10^{12} M_{\odot}$ ), intermediate ( $M_{\text{Halo}} = 10^{13} M_{\odot}$ ), and high halo masses ( $M_{\text{Halo}} = 10^{14} M_{\odot}$ ) with a bin width of  $\pm 0.2$  dex around the central halo mass and plotted the median, 16<sup>th</sup> and 84<sup>th</sup> percentiles of the  $t_{90}$  values as a function of stellar mass, seen in the left mid panel of Figure 3.2.1. We also take three stellar masses ( $M_{\text{Stellar}} = 10^{10.25}, 10^{10.75}, 10^{11.25} M_{\odot} \pm 0.1$  dex) and plotted the median and 16<sup>th</sup> and 84<sup>th</sup> percentiles of the  $t_{90}$  values as a function of halo mass in the right mid panel. We use  $t_{90}$  as this is the best constrained value of the three lookback times, with the smallest uncertainties.

We first observe a consistent, non-monotonic behaviour in the observational sample (median given by the solid line and 16<sup>th</sup> and 84<sup>th</sup> percentiles shaded) when considering the halo mass sub-samples as a function of stellar mass (mid left-hand panel). We also see that for most stellar and halo masses, TNG300 (median given by the dashed line and 16<sup>th</sup> and 84<sup>th</sup> percentiles shaded) predicts lookback times within the scatter of the SDSS sample. We see, however, that the greatest differences between the simulation and observations are at intermediate stellar and halo mass. This difference can be up to 3 Gyr, significantly outside of the observational errors. At these stellar masses and greater, we also observe subtly different trends compared to those inferred from observations, although the values are within the scatter of the distributions.

In the mid right-hand panel we see the lookback times as a function of halo mass in the 3 different stellar mass bins defined above. We see young lookback times with a flat trend as a function of halo mass for the lowest stellar mass bin. For intermediate stellar masses we see intermediate lookback times, with a slight negative trend between the lookback time and halo mass, i.e. galaxies in more massive haloes have slightly younger ages. This behaviour is repeated in the highest stellar mass bin, except at low halo masses, where the sub-population with the highest stellar-to-halo mass ratios lowers the lookback times. When we compare this to TNG300, we see a good agreement of the lookback times in the lowest stellar mass bin and a reasonable agreement in the highest stellar mass bin between the observations and simulations as a function of halo mass. We see, however, that the halo mass trends in TNG300 are reversed with respect to the observations in the intermediate and high stellar mass ranges ( $M_{\text{Stellar}} \sim 10^{10.75} M_{\odot}, 10^{11.25} M_{\odot}$ ), whereby  $t_{90}$  increases with halo mass at fixed stellar mass. This causes differences of up to  $\sim 3$  Gyr at fixed stellar and halo mass. We also observe that the scatter in  $M_{\text{Halo}}$  at fixed  $M_{\text{Stellar}}$  is smaller than in the observations.

To further investigate the drivers behind these differences in the stellar assembly times when we account for both stellar and halo mass, we investigate the quiescent fraction of galaxies (here defining quiescence as  $\text{Log}_{10} \text{ sSFR} < -11 \text{ yr}^{-1}$ , Pasquali et al. 2019) as this can

cause major differences when comparing the ages of two galaxy populations. The quiescent fraction of galaxies yielded by IllustrisTNG has been previously investigated, reproducing observational results to a good agreement at both  $z = 0$  and  $z \lesssim 2$  (Donnari et al. 2019), however much like the stellar mass assembly times, we want to highlight the effects that stellar and halo mass may have on sub-populations and to reveal more subtle trends.

In Figure 3.2.1, bottom panels, we see that TNG300 (dashed lines) reproduces the observed quiescent fraction (solid lines) well in the domains where the lookback times have some level of agreement in the mid panels, however in the domains where we have differences in the lookback times as both a function of stellar or halo mass, there are major differences in the quiescent fraction. This is best seen in the intermediate halo mass bin in the left-hand panel at intermediate stellar masses, whereby TNG300 predicts that  $\sim 80$  per cent of all galaxies should be quiescent, while in the observations  $< 20$  per cent are, and the lookback times are therefore much higher than expected. This is confirmed by the intermediate stellar masses as a function of halo mass in the right-hand panel, whereby nearly all galaxies in this sub-sample are quiescent compared to  $< 20$  per cent on average for the observations.

### 3.3 The Characteristic Galaxy Properties of TNG300 Galaxies

To investigate possible mechanisms that may give rise to the tensions seen in the assembly times between SDSS and TNG300, especially at intermediate stellar masses ( $M_{\text{Stellar}} \sim 10^{10.5} M_{\odot}$ ), we explored a number of host galaxy properties at  $z = 0$  in TNG300 that were likely to be physically linked to the star formation histories or to the quenched fraction of galaxies. Any behaviour or trends in these properties as a function of both stellar and halo mass may indicate possible drivers of these differences in TNG300. Figure 3.3.1 shows the most relevant properties to this investigation.

In the top left-hand panel we have the sSFR as a function of stellar and halo mass. We see a significant change in the sSFR at stellar masses of  $M_{\text{Stellar}} \sim 10^{10.5} M_{\odot}$  with a very slight halo mass dependence at low halo masses ( $M_{\text{Halo}} \sim 10^{12-12.5} M_{\odot}$ ). In the top right-hand panel, we show the  $g - r$  colour binned in stellar and halo mass. The trends in the colours mirror the trends in the sSFR closely, whereby galaxies with lower sSFR rates have redder colours, as expected. The mean cumulative amount of energy injected into the galaxy from AGN feedback via the thermally injected mode ( $E_{\text{Th}}$ ) is shown in the bottom left-hand panel, compared to the kinetically injected mode ( $E_{\text{Kin}}$ ) in the bottom right-hand panel. We see that the amount of energy supplied by the thermal mode increases approximately with stellar mass relatively smoothly. The mean cumulative energy injected by the kinetic mode, however, shows more similar behaviour to the colours and sSFR at  $M_{\text{Stellar}} \sim 10^{10.5} M_{\odot}$ , with a sharper transition from low to high amounts of energy injected compared to the thermal mode, with a slight halo mass dependence after this point, reflecting the behaviour seen in the assembly times and sSFRs.

We postulate a scenario whereby galaxies in IllustrisTNG reach a critical stellar/halo mass ( $M_{\text{Stellar}} \sim 10^{10.5} M_{\odot}$ ,  $M_{\text{Halo}} \sim 10^{12.5} M_{\odot}$ ) and the kinetic mode AGN feedback starts

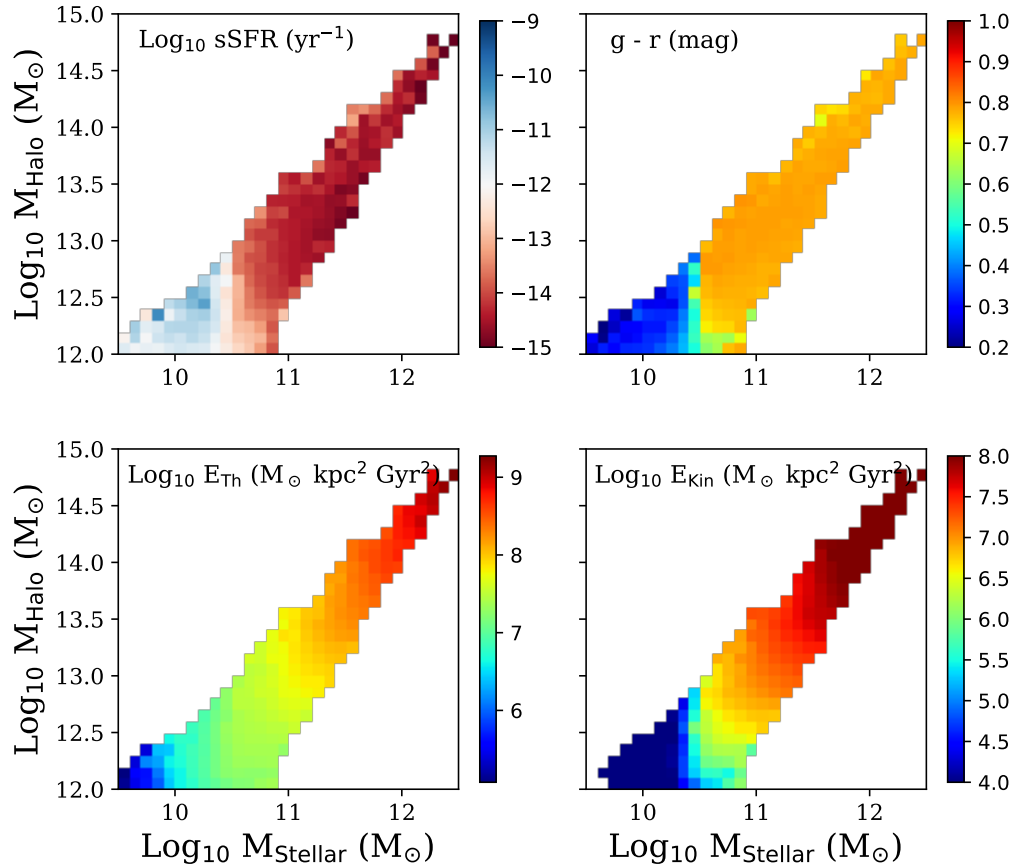


**Figure 3.3.1:** The top left panel shows the mean sSFR and the top right panel shows the mean  $g - r$  colour as a function of both stellar and halo mass in TNG300. The bottom left panel shows the mean cumulative energy injected into the galaxy thermally from AGN feedback, and the bottom right panel shows the same but kinetically. The kinetic mode feedback reflects on average the trends seen in the upper panels and in the assembly times of galaxies in Figure 3.1.2.

to take effect. Taking a scenario with two galaxies of similar halo mass but slightly different stellar masses, we propose that the AGN feedback may rapidly shut down star formation in the slightly less massive galaxy, resulting in old stellar assembly lookback times and higher quenched fraction as seen for intermediate mass galaxies ( $M_{\text{Stellar}} \sim 10^{10.5} M_{\odot}$ ,  $M_{\text{Halo}} \sim 10^{13} M_{\odot}$ ). This means that the second galaxy with slightly more stellar mass is more resistant, due to a larger gravitational potential, and can continue forming stars, albeit likely at a lower rate, thereby lowering the stellar assembly lookback times. Beyond this critical stellar/halo mass ( $\sim 0.5$  dex higher in stellar and halo mass), the kinetic mode AGN feedback dominates, shutting down star formation in most systems and causing lookback times to be even in stellar and halo mass phase space. Further investigation beyond the scope of this research is needed in order to confirm this scenario however.

### 3.4 The Stellar Mass Growth Rate of SDSS Galaxies

In order to investigate the assembly of each present-day stellar and halo mass bin of our observational sample in more detail, with a focus on the galaxy sub-population with the highest stellar-to-halo mass ratios ( $M_{\text{Stellar}} \sim 10^{11} M_{\odot}$  and  $M_{\text{Halo}} \sim 10^{12} M_{\odot}$ ) and with young  $t_{90}$  lookback times, we calculate the mean growth rate of each galaxy per Gyr. This reveals at which epochs certain sub-populations of galaxies experienced greater rates of growth with respect to others, disclosing more detail about the evolution of each sub-population. As outlined in Section 2.2, the SED fitting process also estimates the stellar mass of each individual galaxy in 1 Gyr intervals, ranging from 0 Gyr to 11 Gyr. From this we can define the growth of a galaxy per Gyr as follows:

$$\text{Growth} = \Delta M/M = (M_i - M_{i+1})/M_{i+1} \quad (3.1)$$

where  $M_i$  is the stellar mass of a galaxy at a specific epoch and  $M_{i+1}$  is the stellar mass of the same galaxy 1 Gyr earlier (e.g. when  $M_i = M_{\text{Stellar}}$ , 1 Gyr ago,  $M_{i+1} = M_{\text{Stellar}}$ , 2 Gyr ago).

Applying the same binning procedure in present-day stellar and halo mass as before and calculating the Malmquist weighted means of each bin yields Figure 3.4.1. This shows the mean stellar mass growth of each bin in 1 Gyr intervals, from 11 Gyr ago up to the present day, with the specific epoch given by the labels inset in each plot. We note here that each sub-plot has a separate colour bar, in order to be able to differentiate growth accordingly at various epochs. We see that the average trends in stellar and halo mass in the observational sample from Figure 2.1.1 and Figure 3.1.1 are replicated. At fixed  $M_{\text{Halo}}$  the mass growth slows down as  $M_{\text{Stellar}}$  increases, while at fixed  $M_{\text{Stellar}}$  (where  $M_{\text{Stellar}} < 10^{11} M_{\odot}$ ) the mass growth is stronger in more massive haloes.

The most massive galaxies in this sample ( $M_{\text{Stellar}} \sim 10^{11.5} M_{\odot}$ ,  $M_{\text{Halo}} \sim 10^{14} M_{\odot}$ ) have undergone, relatively, very little growth in stellar mass since early epochs, as expected from the old lookback times in Section 3.1. The sub-population of galaxies with the highest stellar-to-halo mass ratios ( $M_{\text{Stellar}} \sim 10^{11} M_{\odot}$  and  $M_{\text{Halo}} \sim 10^{12} M_{\odot}$ ) and with young  $t_{90}$  lookback

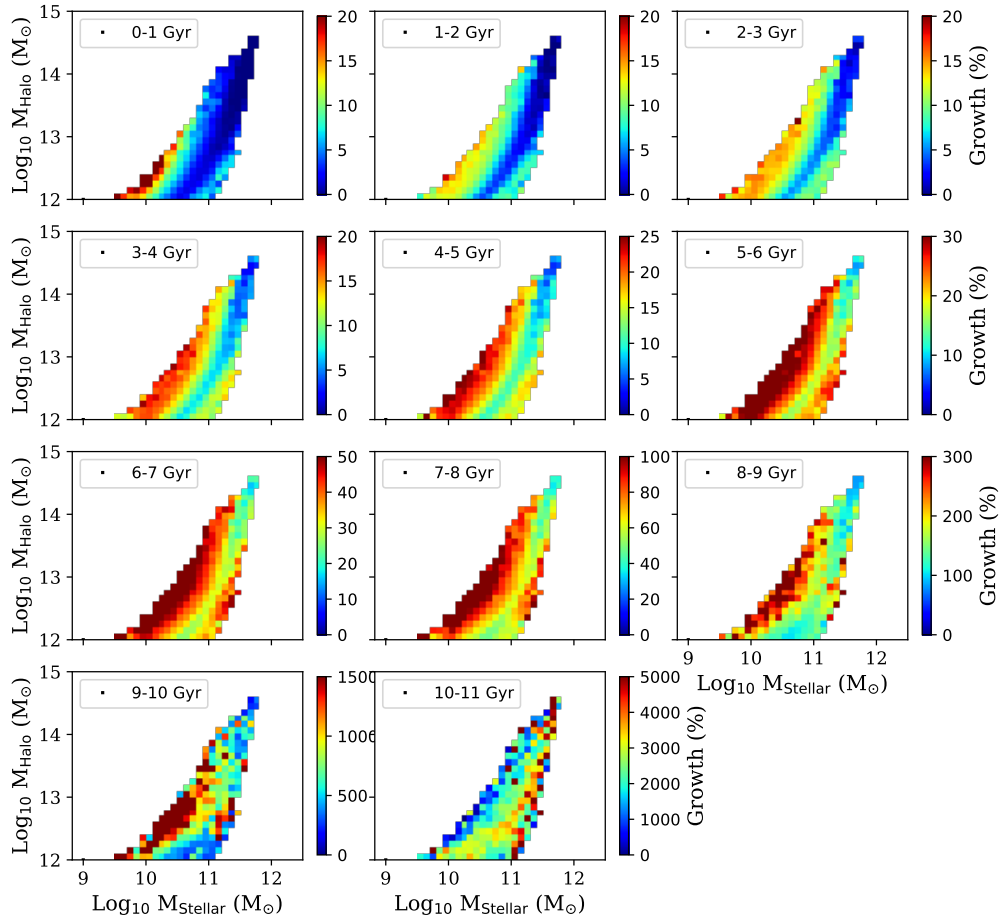


**Figure 3.4.1:** The average percentage growth rate of each SDSS galaxy bin over a Gyr (lookback time given in each panel) as defined in Equation 3.1. We see that the lowest mass galaxies have significantly the highest rate of growth from  $\sim 5$  Gyr ago until the present day. We also see that the galaxies with high stellar-to-halo mass ratios have relatively steady growth rates at all epochs, although significantly less than the lowest mass galaxies from  $\sim 5$  Gyr ago to the present.

times from Figure 3.1.1, appear to have had a fairly steady relative growth throughout cosmic time. The growth rate in stellar mass for this sub-sample in the last 6 Gyr is an average of  $\sim 10$  per cent per Gyr and attains a maximum of  $\sim 25$  per cent per Gyr.

We also see that those galaxies with low stellar mass and low stellar-to-halo mass ratios (i.e. those on the left-hand side of the distribution) have the highest relative growth from  $\sim 5$  Gyr ago until the present day, as expected for low mass star-forming galaxies. We note, however, that this growth rate is still at maximum  $\sim 30$  per cent per Gyr in the last 6 Gyr, and is unlikely to be high enough to shift them towards the median of the distribution in stellar and halo mass phase space.

### 3.5 Assembly Trends Yielded from the EAGLE Simulations

A useful test for the IllustrisTNG simulations is to investigate if other hydrodynamical cosmological simulations yield similar trends in the assembly times, or if not the assembly times, a similar property. Similar trends could indicate a problem altogether for simulations as a whole in their implementation of AGN feedback and the effects it has on galaxy formation and assembly, whereas different trends may indicate a problem specific in the modelling applied in IllustrisTNG. There are a number of different such simulations such as SIMBA (Davé et al. 2019) or HORIZON-AGN Dubois et al. (2014). For this test, we use the Evolution and Assembly of GALaxies and their Environments (EAGLE) simulations (Schaye et al. 2015; Crain et al. 2015).

The EAGLE simulations are a suite of hydrodynamical simulations<sup>1</sup> (Crain et al. 2015; Schaye et al. 2015). The simulations use a version of the GADGET-3 Smoothed Particle Hydrodynamics (SPH) code (Springel 2005), with the cosmological parameters from the Planck mission (Planck Collaboration et al. 2015) implemented, whereby  $\Omega_\Lambda = 0.693$ ,  $\Omega_m = 0.307$ ,  $\Omega_b = 0.04825$  and  $H_0 = 67.77 \text{ km s}^{-1}$ . As with IllustrisTNG, to account for all processes which operate below the numerical resolution limit, the simulations employ sub-grid physics prescriptions relying only on local hydrodynamic properties. This includes schemes covering radiative cooling and photo-ionisation heating (Wiersma et al. 2009a), stellar mass loss (Wiersma et al. 2009b) and stellar feedback (Dalla Vecchia & Schaye 2012), black hole growth and feedback and star formation (Schaye & Dalla Vecchia 2008). These are then calibrated to reproduce the stellar mass function, the black hole mass - bulge mass relation and the galaxy stellar mass - size relation at  $z = 0.1$ . A full description of the simulations can be found in Schaye et al. (2015) and Crain et al. (2015).

We briefly outline the processes star formation and black hole accretion in more detail as they are the most relevant to this work. Star formation is modelled according to Schaye & Dalla Vecchia (2008) as a stochastic process based on the pressure dependent Kennicutt-Schmidt law with a Chabrier (2003) IMF. Black holes are seeded in the densest gas particle in every dark matter halo greater than  $1.48 \times 10^{10} M_\odot$ , which then grow through accretion of other particles. The energy attained via accretion, assuming a radiative efficiency  $\epsilon = 0.1$ , is not released immediately, but stored as an energy reservoir for a period of time given

<sup>1</sup><http://icc.dur.ac.uk/Eagle/>

by an injection probability distribution and then injected into the gas particles surrounding the black hole. This purely thermal feedback differs then from the two-stage feedback in IllustrisTNG outlined above, meaning that any differences in the trends may indicate that the AGN feedback is responsible for tensions between the observations and simulations rather than the simulations as a whole.

The EAGLE simulation suite also has various simulation box sizes, resolutions and physical models (Rosas-Guevara et al. 2016) such as higher AGN heating temperature and increased black hole viscosity. Further details of these variations can be found on the EAGLE database (McAlpine et al. 2016). The standard model referred to hereafter incorporates AGN feedback and standard values for multiple parameters which can be found in Crain et al. (2015) as RefL0100N1504. We note that the box size is significantly smaller than the TNG300, meaning we are only searching for approximate trends, rather than a fully quantitative comparison.

Due to the difference found in simulations and collaborations, not all parameters available in the IllustrisTNG simulations are available in EAGLE, hence we select the parameters as closely as we can. We apply a similar cut in halo mass as for TNG300, which is based on the friends-of-friends algorithm and which corresponds to  $M_{200,\text{mean}}$ . Hence, although not the same, we do not expect this difference in halo mass definition to significantly affect trends, and we select only central galaxies. This yields a total sample of  $\sim 4800$  galaxies, about 10 per cent of the TNG300 sample. We therefore have to be careful of over interpretation with such different sample sizes. We then use the available data for the average stellar ages of each galaxy and bin using the same method as above in stellar and halo mass (0.1 dex bins, minimum of 10 galaxies per bin). The results can be seen in Figure 3.5.1.

We see very similar behaviour as a function of stellar and halo mass in the average stellar ages yielded by EAGLE compared to the assembly time in IllustrisTNG. We see that at low halo masses ( $M_{\text{Halo}} \lesssim 10^{12.5} M_{\odot}$ ), as we increase stellar mass, we observe an increase in the average stellar age, as may be reasonably expected. Immediately above these halo masses ( $M_{\text{Halo}} \sim 10^{13} M_{\odot}$ ), we see an inversion of this behaviour, whereby the age decreases with increasing stellar mass. At the highest halo masses ( $M_{\text{Halo}} > 10^{13} M_{\odot}$ ), we find an even distribution of ages, all of which are old. Interestingly, we also find that some of the oldest objects in the simulations reside at intermediate halo and stellar masses. We conclude then, that it is likely that cosmological hydrodynamical simulations struggle to reproduce the observed trends in stellar mass assembly, and that AGN feedback regardless of its implementation may be over aggressively quenching galaxies around a critical halo mass (i.e. it is not just the implementation scheme of AGN feedback in IllustrisTNG which causes tensions when considering both stellar and halo mass in the assembly of central galaxies).

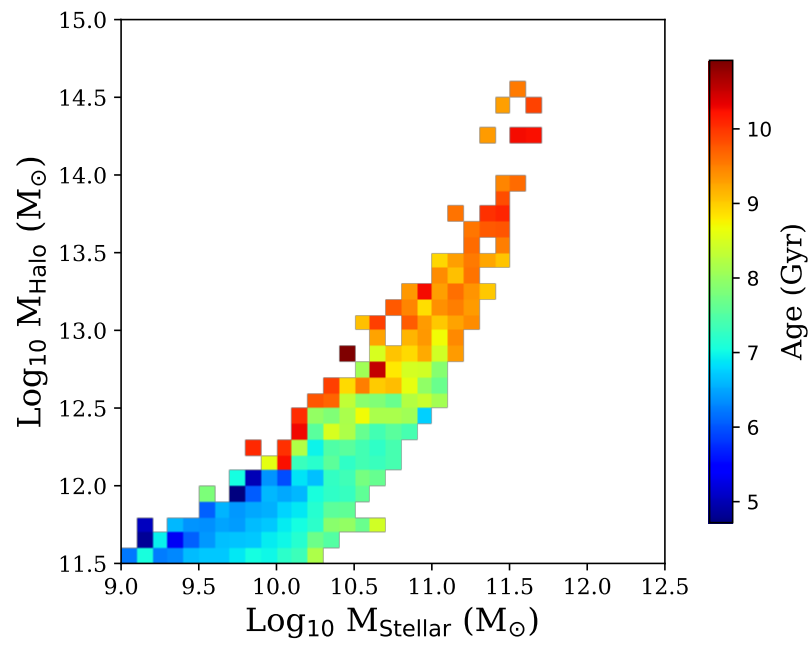


**Figure 3.5.1:** The average stellar age of central galaxies within the EAGLE simulations as a function of stellar and halo mass. We see very similar trends in stellar and halo mass to the stellar assembly times in IllustrisTNG300.

*"Tough work knocks the silliness out of you when you grow up in places like ours. It teaches you to get tougher, or get lost. Them that are all talk are soon found out, left sitting, feeling sorry for themselves, exhausted by mid-afternoon, whilst the older men are grafting away like they have only just started."*

James Rebanks – The Shepherd’s life, 2015

# 4

## Data and Methods for the Size Growth of Central Galaxies

Having studied the stellar mass assembly of a sample of massive, central galaxies in the low-redshift universe, we now turn our attention to the size growth histories of a sub-sample of these galaxies. As we are investigating the likelihood of the minor merger scenario, we want to investigate the satellite galaxy population and the nature of stellar material in the outskirts of galaxies, manifested in LSB features. For this part of this research we present the deep imaging data taken from public surveys and a number of techniques to quantify the properties of the stellar material in these galaxies. This Chapter of the thesis is contained in the paper of [Jackson et al. \(2021\)](#). Contributions by collaborators to this Chapter are as follows: Dr. Anna Pasquali for helping with the visual classification of the galaxy samples and Dr. Surhud More for general advice on the HSC imaging data and data reduction pipeline. Thanks also go to Dr. Song Huang for his advice on accounting for residuals from the sky background subtraction.

### 4.1 The Subaru Hyper-Suprime-Cam Survey and Data

Large scale extragalactic surveys such as the SDSS ([York et al. 2000](#)) have revolutionised our understanding of galaxy evolution by providing a large sample of uniform imaging across a significant area of the sky. The drawback with these samples, however, is that they usually lack the depth of other surveys for more detailed studies such as the Mass Assembly of early-Type GaLaxies with their fine Structures survey (MATLAS survey [Duc et al. 2015](#); [Duc 2020](#)). These types of surveys are usually carried out with larger aperture telescopes. The disadvantage of such deeper observations however is that the coverage of the sky is usually

smaller. The Subaru Hyper Suprime Cam (HSC) - Subaru Strategic Programme (-SSP [Aihara et al. 2018](#)) is one survey that is trying to bridge this gap.

The HSC-SSP is an ongoing survey designed to image significant parts of the sky, in 5 different bands ( $g, r, i, z, y$ ). 1400 sq degrees of the sky are being imaged down to 26.1 mag (wide survey), 27 sq degrees down to a magnitude of 27.1 mag (deep survey) and 3.5 sq degrees down to 27.7 mag (ultra-deep survey) in the  $r$ -band. The camera has a pixel scale of 0.168" ([Miyazaki et al. 2018](#)) and the survey has so far experienced a median seeing in the  $i$ -band of 0.6" ([Aihara et al. 2018](#)). In order to attain a statistically significant sample we used the wide survey of the incremental DR2 (300 sq degrees, [Aihara et al. 2019](#)). The HSC data reduction pipeline ([Bosch et al. 2018](#)) automatically performs sky subtraction, bias, flat field correction and flux calibration. [Huang et al. \(2018a\)](#) injected synthetic galaxies into HSC images, achieving a 13 and 18 per cent precision at a depth of 20 and 25 mag respectively in the  $i$ -band for extended objects when fitting single Sérsic profiles. The HSC fields have been chosen especially for their low levels of extinction along the line of sight, however we still applied a correction for Galactic foreground reddening to each image according to the law of [Cardelli et al. \(1989\)](#), using the extinction maps of [Schlafly & Finkbeiner \(2011\)](#).

To obtain the galaxy sample for this part of the research, we applied the following cuts to our sample of  $\sim 90,000$  SDSS central galaxies from Chapter 2: In order to capture galaxies that have experienced a passive stellar mass evolution over the last few Gyr, and thereby similar systems to those analysed in higher redshift studies, we selected those galaxies contained in the HSC DR2 fields that have a  $t_{90}$  value larger than 6 Gyr (reducing the sample to  $\sim 440$  galaxies). We also selected those galaxies with a spectroscopic redshift of  $0.05 < z < 0.1$  in the group catalogues of [Lim et al. \(2017\)](#), in order to perform the best spatially resolved analysis we could on the individual galaxies themselves, while still retaining a statistically significant sample (reducing the sample to 142 galaxies). We also applied the criterion that each galaxy must have coverage in all 5 bands of HSC ( $g, r, i, z, y$ , reducing the sample to 134 galaxies) and a minimum of 50 bins at a  $S/N > 10$  in its outskirts (beyond the SDSS Petrosian radius of  $\sim 2 R_{\text{eff,SDSS}}$  as given in [Pacifi et al. 2016](#)) as computed by the Voronoi binning (see Section 4.3). Selecting galaxies that have a minimum number of the bins in the outskirts may slightly bias our results, whereby galaxies with little activity are likely to have less light/mass excess in their outskirts and are therefore more likely to be discarded, however we stress that only 4 galaxies are discarded from this specific selection process. Hence, we do not expect our results to be significantly impacted by galaxies discarded due to low numbers of Voronoi bins in their outskirts. Two galaxies contained in the [Kauffmann et al. \(2003\)](#) catalogues defined as AGN or low-ionization nuclear emission-line region (LINER, based on the selection methods of [Baldwin et al. 1981](#)) were also removed so as to avoid radiation from AGN biasing our results.

In the visual classification we also removed galaxies that had problems in the data with at least 1 band, such as missing data, over-saturation of pixels or imaging artefacts (10 galaxies). The final sample contains 118 centrals from the parent sample of  $\sim 90,000$ , hereafter referred to as our passive galaxy sample and shown in the left half of Figure 4.1.1. The morphological splits are described in Section 4.2 and their relative distributions in halo

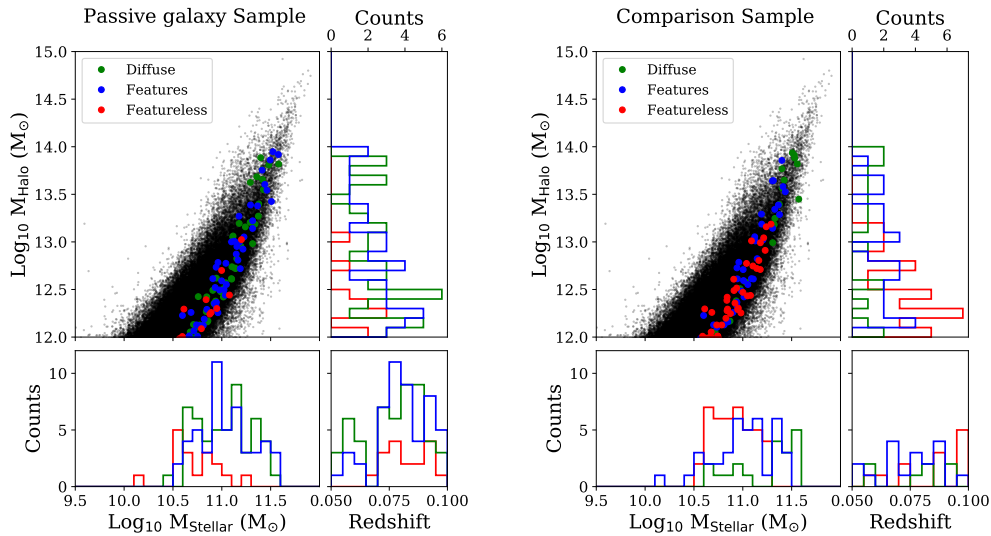


**Figure 4.1.1: Main panel of each half:** The distribution of our observational sample in stellar and halo mass phase space. Black points give the parent sample of  $\sim 90,000$  SDSS central galaxies as detailed in Chapter 2. Blue (green, red) points show galaxies with signs of merger activity (a diffuse stellar halo, no activity) as determined by the visual classification described in Section 4.2. **Side and bottom panel of each half:** The distributions in stellar and halo mass of each classified sub-sample. **Bottom right panel of each half:** The distribution of each sub-sample in redshift.

and stellar mass space are shown in the side and bottom panels of the left half of Figure 4.1.1. The bottom right panel of the left half of Figure 4.1.1 shows the distributions in redshift for later checks in sensitivity biases.

We also selected a comparison sample of 118 galaxies from the same parent sample of central galaxies using the same selection criteria in order to build a full picture of the evolutionary processes we want to investigate. We selected these galaxies to have as small a combined difference in stellar mass ( $< 0.1$  dex), halo mass ( $< 0.1$  dex) and redshift ( $< 0.01$ ) phase space to the passive galaxy sample while avoiding selecting the same galaxy twice. This comparison sample was chosen, however, to have a  $t_{90} < 4$  Gyr, in order to compare relatively young centrals to our older and passive galaxy sample. This sample is seen in the right half of Figure 4.1.1, with the same scheme for the subplots as for the passive galaxy sample in the left half.

We see that each distribution spans a significant range in halo mass ( $\sim 2$  dex) and stellar mass ( $\sim 1.5$  dex). We also notice that those galaxies that display a diffuse stellar halo (see Section 4.2 for more details of the morphological classification) generally occupy the most massive haloes ( $M_{\text{Halo}} \gtrsim 10^{13} M_{\odot}$ ) and those that display no tidal features (featureless) generally occupy the least massive haloes ( $M_{\text{Halo}} \lesssim 10^{13} M_{\odot}$ ). The galaxies that display tidal features, indicative of merger activity (features) display a tendency to occupy more massive haloes, however are distributed across the full range of halo masses. These trends are similar in stellar mass, in agreement with findings from previous studies (Bílek et al. 2020). In their

study, [Bílek et al. \(2020\)](#) find 1.7 times the amount of tidal features above a stellar mass of  $10^{11} M_{\odot}$  than below, which compares to an increase of 1.2 in our sample (a difference of  $1\sigma$ ). This difference may be due to slightly different classification schemes or, more likely, the different data sets, whereby the data of [Bílek et al. \(2020\)](#) is deeper than that used in this study. They also find an increase in some of their features with increasing environmental density, similar to our results. In the bottom right panel, we see a fairly even distribution of all three sub-samples across redshift. The implications of this behaviour are discussed further in [Section 8.2](#).

We also visually classified galaxies into early- and late-type, finding that  $\sim 1$  per cent of our passive galaxy sample is classified as late-type with the rest of the sample classified as early-type. This statistic rises to  $\sim 26$  per cent for our comparison sample, with  $\sim 74$  per cent of galaxies classified as early-type. To reinforce this, we calculated the average Sérsic index of each sample using the catalogues of [Blanton et al. \(2005\)](#) and the bulge-to-total mass ratios using the catalogues of [Mendel et al. \(2014\)](#). We find that the average Sérsic index of the passive galaxy sample is 5.00 with an average bulge-to-total mass ratio of 0.78, compared to an average Sérsic index of 3.14 for the comparison sample with an average bulge-to-total mass ratio of 0.60. This shows that our older, passive galaxy sample is dominated by early type morphologies, which have larger Sérsic indices than the comparison sample.

## 4.2 The Visual Classification Scheme

Visual morphological classification, although with a reasonable degree of subjectivity, has proven to be an extremely useful tool in the study of galaxy evolution, with one of the first and the most used classification systems first developed by [Hubble \(1926\)](#). Morphological classification can be used as an indicator of the current stage of evolution that a galaxy may be at in its lifetime. Similarly, morphological features or disruptions of the stellar material or gas can help indicate if a galaxy may be undergoing environmental processes such as merging or stripping. Today, researchers can use a number of methods: they can either manually classify their own data set or, if it is too large, public schemes such as Galaxy Zoo ([Lintott et al. 2008](#)) have been set up. Machine learning techniques have also been and are being developed for this application (e.g. [Banerji et al. 2010](#); [Hocking et al. 2018](#)).

As both of our samples are relatively small and previous studies in this field have used similar classification schemes, each galaxy was independently visually inspected and classified with the help of different co-authors. Changing the contrast of each image in the *i*-band was used to search for LSB features, with a high level of agreement of the classifications between the different co-authors. The *i*-band was chosen as it has the best median seeing ( $\sim 0.6''$ ) of all HSC bands. We note that there is a degree of subjectivity to this system that needs to be taken into account when drawing conclusions from the results or comparing to previous studies. We classified both the passive galaxy sample and the matched comparison sample into three categories.

In order to quantify the abundance (or lack of) minor merger activity that may be driving the size growth of central galaxies, the first category is those galaxies that display features

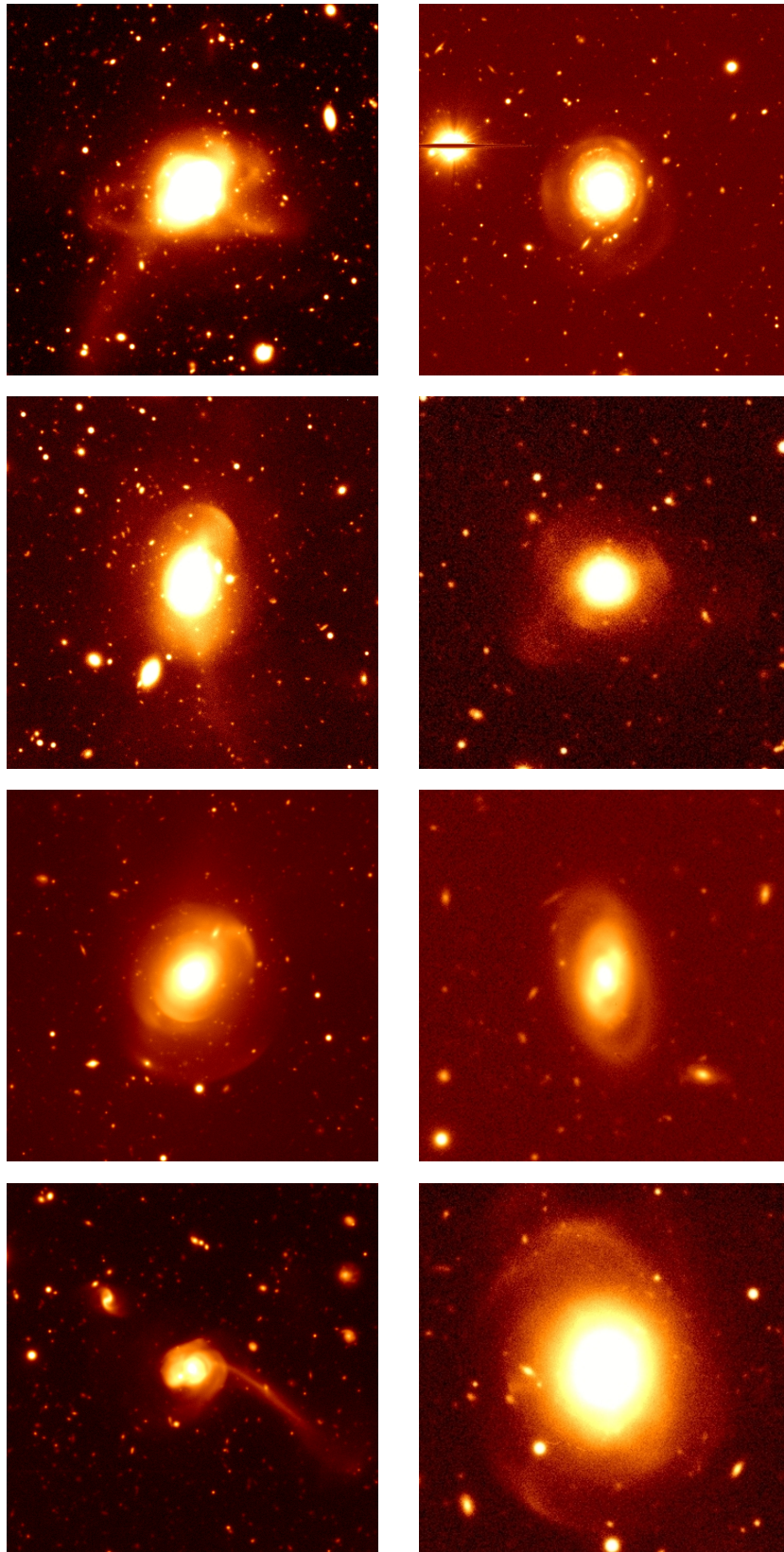


**Figure 4.2.1:** A selection of galaxies taken from the HSC passive galaxy sample and classified in the "features" sub-sample. We see a range of activity. Streams are present in the top-left, top-right, upper mid-left and upper mid-right and bottom right. Shells are present in the upper mid-right and lower mid-left. We see a stellar ring in the lower mid-right, and a minor merger in the bottom right. We also classify umbrellas in the upper mid-left and bottom right.

caused by merger activity. As we are dealing with central galaxies, we expect any features observed to be almost exclusively caused by galaxy interactions with their satellites. This sub-sample was identified in the following ways: galaxies which display shells, those that display a ring of material around the main body of the galaxy, those with streams of material, those that display umbrella-like features (e.g. [Martínez-Delgado et al. 2010](#)), those that have clear distortions to the light distribution and those undergoing a minor merger (when a clear and significant secondary peak/core in the light distribution is seen). Some galaxies may display multiple features. This sub-sample is hereafter referred to as "features", and some examples are given in Figure [4.2.1](#).

The second category is those galaxies with no clear tidal features but that visually exhibit a diffuse stellar halo (hereafter labelled as "diffuse"). These galaxies were classified as such as a clear diffuse stellar halo may indicate past merger activity with the accreted material now settled into a state of relative equilibrium. We note that galaxies that have diffuse stellar haloes but also display clear signs of merger activity are classified into the features sub-sample.

The last category is those galaxies that display neither tidal features nor a diffuse stellar halo (hereafter labelled as featureless). Examples of each of the three categories (features, diffuse and featureless) can be seen in Figure [4.3.1](#).

### 4.3 The Treatment Process of the HSC Imaging Data

In order to analyse the data while accounting for biases and reducing errors we implemented the following procedures on the HSC imaging data presented in Section [4.1](#).

In order to account for the effects of the Point Spread Function (hereafter PSF) over all photometric bands we measured the Full-Width-Half-Maximum (FWHM) for each galaxy in each band as given by the PSF models constructed by the HSC pipeline (see [Bosch et al. 2018](#), for more details). In order to account for the worst PSF across the entire sample, we took the largest FWHM in the entire galaxy sample and convolved each galaxy in each band with the quadrature of the difference between that band and the maximum overall FWHM. We note that this technique has been used in the majority of previous studies investigating similar galaxy properties, but that this technique does not take into account the effects of the wings of the PSF. We address this problem further in Section [5.3](#).

We then assigned a threshold signal-to-noise ( $S/N$ )  $> 3$  per pixel to the imaging data. This  $S/N$  was chosen since, on visual inspection, lower cuts introduce too much contamination from foreground and background objects and higher cuts discard many of the tidal features we observe in the data at low surface brightness. We then used the source detection routine from the *photutils* package in *ASTROPY* in order to locate all pixels associated with each galaxy, including the tidal features. The routine uses an algorithm based on the number of neighbouring pixels also associated with the source to find all pixels associated with a local maximum. Examples of this can be seen in the top two rows of Figure [4.3.1](#), where the top rows show the original *i*-band images from HSC and the second rows show the detected galaxies in the *r*-band surface brightness maps.

Some pixels in our sources have low signal-to-noise, however, just reaching the threshold  $S/N$  of 3 per pixel. These are usually the low surface brightness features we want to quantify. In order to reduce uncertainties in the estimates yielded by the SED fitting process we used Voronoi binning (Cappellari & Copin 2003) to maximise the signal-to-noise of these features, while still preserving the spatial resolution of higher  $S/N$  areas. We took the SDSS Petrosian apertures ( $\sim 2 R_{\text{eff,SDSS}}$ ) for the central areas of our galaxies as this is the aperture used in the study of Pacifici et al. (2016) from which the parent sample is built in Jackson et al. (2020b) and from within which many of the integrated galaxy properties are estimated such as  $t_{90}$ . We then Voronoi binned all pixels inside of this aperture to a constant  $S/N = 50$  per bin, as the signal-to-noise per pixel in these regions is high. For all pixels outside of this aperture, the outskirts of the galaxy, we defined a constant  $S/N = 10$  per bin, as this is a high enough signal-to-noise to reduce uncertainties in the stellar mass estimates while avoiding the washing out of detail that can occur when Voronoi binning at a signal-to-noise of 50. This allowed us to probe features that have a surface brightness as low as  $\sim 28$  mag arcsec $^{-2}$  in the  $r$ -band. We also masked bins with contamination from significant foreground and background objects in order to reduce contamination that could bias our results. We note that this makes up only 1.4 per cent of all bins, and although increases with radius, due to less bins at higher radii, never contributes above 2.5 per cent of all bins, hence we do not expect this to significantly bias our radial profiles. As tidal features are not uniform, we do not attempt to interpolate across neighbouring bins as this method would introduce its own biases to our results.

Total fluxes were then calculated for each Voronoi bin from the imaging data in the following manner: The median flux of each Voronoi bin was calculated and multiplied by the amount of pixels in the Voronoi bin, so as to avoid fluctuations due to contaminating objects that can bias the mean, especially at low surface brightness. Associated errors were calculated using the variance maps added in quadrature with the flux calibration error. The fluxes and associated errors were then converted into magnitudes for colour profiles, with a median error of  $\sim 0.2$  mag, smaller than the scatter in the stacked radial colour profiles of both samples of galaxies. We also calculate the physical area of each Voronoi bin, allowing us to calculate the stellar mass surface density after the SED fitting process outlined in Section 4.4 and surface brightness (we probe features that have a surface brightness as low as  $\sim 28$  mag arcsec $^{-2}$  in the  $r$ -band). We also ran Voronoi binning at constant signal-to-noise ratios of 20 and 30 per bin, to verify if our adaptive Voronoi binning process introduces biases to our results, finding minimal overall differences in the profiles, however the loss of spatial resolution means fewer Voronoi bins, and hence more stochastic fluctuations.

As a final step we also address the issue of sky background subtraction: As outlined in Section 4.1, the HSC pipeline performs automatic sky background subtraction, however there are systematic issues in some bands. In order to circumvent this problem, we collect forced photometry performed using a 1 arcsec aperture on empty parts of the sky from the HSC database. We then calculate the median flux per pixel of the sky background of the nearest 100 points to each galaxy in each band. These median flux per pixel values are then applied to each Voronoi bin, in order to account for systematics in the sky background subtraction. We note that the sky background contributes between 1 and 5 per cent of the integrated flux

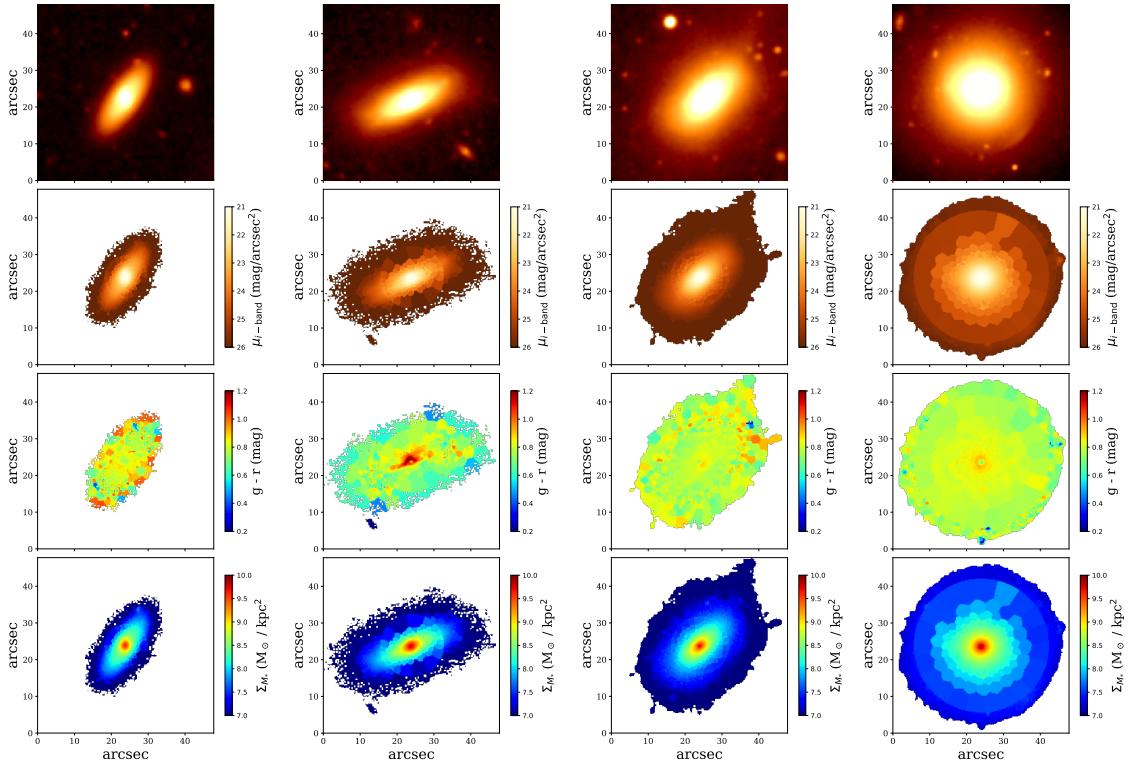


**Figure 4.3.1:** Top to bottom panels of each column: The  $i$ -band image of a galaxy, the Voronoi binned  $r$ -band surface brightness map, the Voronoi binned  $g-r$  colour map and the stellar mass density map as yielded by the SED fitting on the Voronoi binned maps. Left to right: An example of a galaxy classified as displaying no merger activity, a galaxy classified as displaying a diffuse stellar halo, a galaxy with a stream of material to the top right and a galaxy that displays a slight shell structure to the bottom right.

per Voronoi bin, and is smaller than the scatter on the distributions and the uncertainties in the majority of our integrated fluxes.

The results of this process can be seen in Figure 4.3.1, where the third panel shows the corresponding  $g - r$  colour map and the bottom panel shows the corresponding stellar mass surface density map as recovered by the SED fitting process described in Section 4.4. From left to right we see an example of a featureless galaxy, a diffuse galaxy, a galaxy that exhibits a stream and a galaxy that displays a shell (both classified in the Features sub-sample).

## 4.4 The SED Fitting Process with CIGALE

In order to estimate the stellar mass corresponding to each Voronoi bin in our data, we used the SED fitting software CIGALE (Burgarella et al. 2005; Noll et al. 2009; Boquien et al. 2019). We chose CIGALE due to its speed, since due to the resolution and depth of our imaging data, the Voronoi binning process yielded over 500,000 SEDs that needed fitting for each sample. CIGALE can fit SEDs spanning from the UV to the IR range of the electromagnetic spectrum and is based on an energy balance principle, whereby the attenuation due to dust of the UV radiation produced by massive young stars is expected to be re-radiated in the IR part of the spectrum. It also has models to account for AGN emission, dust attenuation, multiple star formation histories and stellar population models.

As we expected these systems to be dominated by old stellar material, however with the possibility of some recent star formation triggered by interactions, we generated models in CIGALE based on double-exponential star formation histories spanning ranges between 2 and 12 Gyr for the main burst. As our passive galaxies are selected to have formed 90 per cent of their stellar mass over 6 Gyr ago (this is between 3 and 4 Gyr for our comparison sample in almost all cases), we limit the additional burst to a contribution of between 0.1 and 5 per cent of the mass with ages ranging between 100 Myr and 2 Gyr. The best-fit SFH contains a 0.1 per cent secondary burst in the overwhelming majority of cases. We then used these star formation histories with the synthetic stellar libraries of Bruzual & Charlot (2003), assuming a Chabrier (2003) IMF and metallicities spanning the full range from  $1/30^{\text{th}}$  solar to 4 times solar in order to generate the model SEDs to fit to the HSC photometry. We neglected AGN contributions to the modelling as we removed AGN from the sample as described in Section 4.1.

We also inserted the  $g$ ,  $r$ ,  $i$ ,  $z$  and  $y$  HSC filter functions into CIGALE and fit the SEDs. The average uncertainties yielded by the SED fitting process for the estimations of stellar masses are of the order of 0.3 dex, which when accounted for in the stellar mass surface densities are, on average, smaller than the scatter in the corresponding radial profiles of our sample of galaxies, meaning that the errors do not significantly bias our results.

Example SEDs of the central regions of two galaxies (i.e. within  $\sim 2 R_{\text{eff,SDSS}}$ ) can be found in Figure 4.4.2 while the SEDs of two Voronoi bins can be found in Figure 4.4.1. In all cases: The top panels of each subplot show the best-fitting model SED (black line), model fluxes (red points) and the observed photometry (magenta open circles). The bottom panels of each subplot show the residuals between the observed and best-fitting model photometry

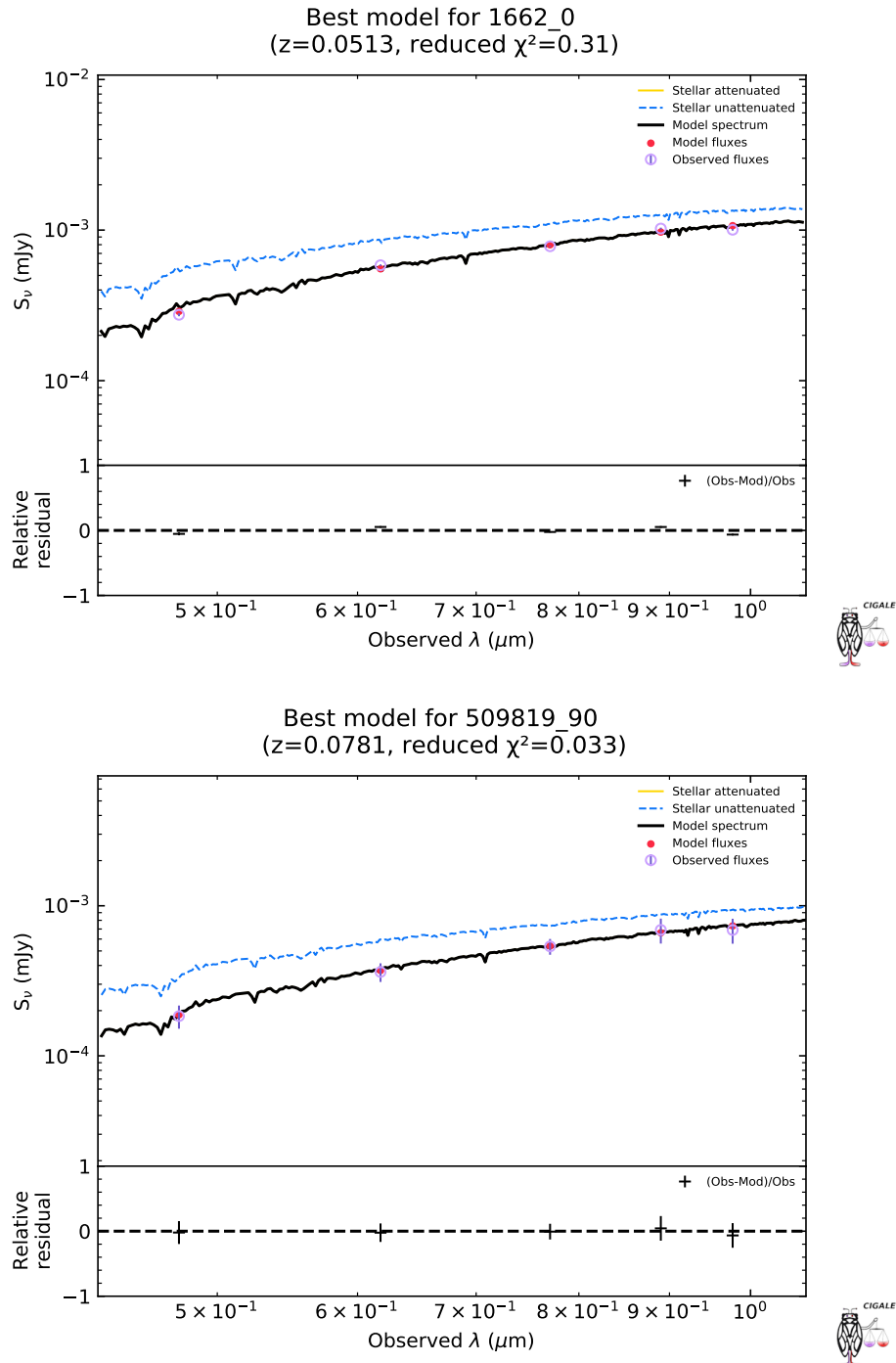


**Figure 4.4.1:** Example SED fits of the HSC photometry of the integrated central regions of two of our HSC galaxies. **Top panel of each sub-plot:** The best-fitting model SED is indicated by the black solid line, the expected model fluxes are indicated by the red points and the observed photometry is represented by the magenta open circles. **Bottom panel of each sub-plot:** The residuals between the expected fluxes from the best-fitting model and the observed photometry.

respectively.

Further checks of the reliability of the SED fitting presented here are discussed in Appendix [A.3](#).

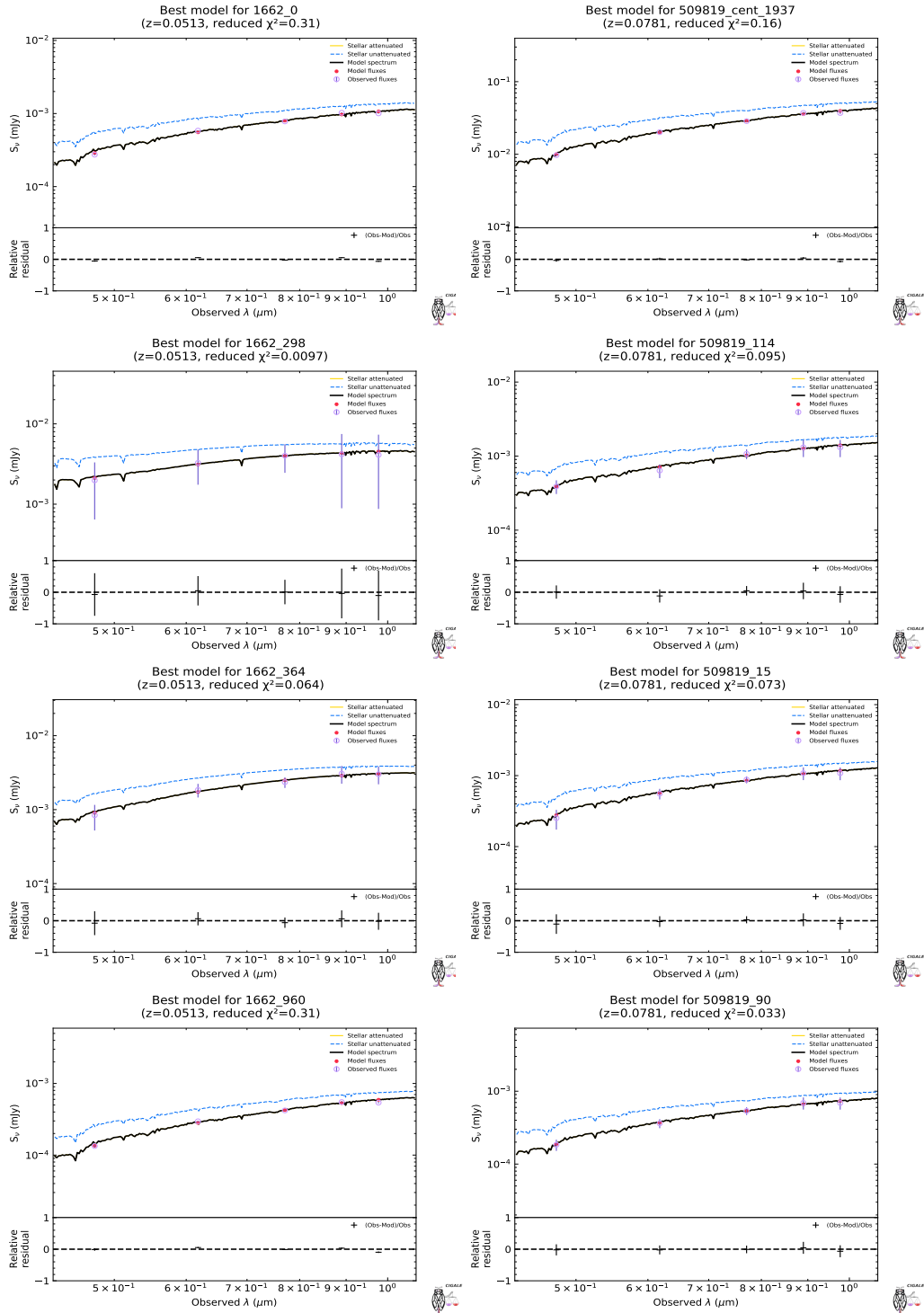


**Figure 4.4.2:** 8 example SED fits of the HSC photometry of random Voronoi bins from two of our HSC galaxies. **Top panel of each of the 8 sub-plots:** The best-fitting model SED is indicated by the black solid line, the expected model fluxes are indicated by the red points and the observed photometry is represented by the magenta open circles. **Bottom panel of each of the 8 sub-plots:** The residuals between the expected fluxes from the best-fitting model and the observed photometry.

*"his Ullswater herd of Holstein Friesian cattle gained an international reputation and produced numerous award-winning animals. One cow, Ullswater Present 9, won three Royal show championships for Mr. Carrick"....."with them a young cowman named Phillip Jackson who was to play a huge part in the success of the herd."*

Obituary of Thomas Carrick, employer of my grandfather Phillip Jackson – Cumberland and Westmoreland Herald, Saturday 13th March 2004

# 5

## Results II - The Size Growth of Central Galaxies Through Radial Profiles

Having presented our data, sample and methods in the previous Chapter, we now present the results in the form of the level of merger/interaction activity, radial gradients of both the passive and comparison samples and a comparison to previous studies. This Chapter of the thesis is contained in the paper of [Jackson et al. \(2021\)](#). Contributions by collaborators to this Chapter are as follows: Dr. Francesco La Barbera for carrying out the convolution of the manually constructed PSFs with the constructed stacked galaxy; Dr. Anna Pasquali, Dr. Francesco La Barbera, Dr. Surhud More and Prof. Eva Grebel for the discussion of tests and plots throughout and the discussion of results.

### 5.1 The Levels of Merger Activity

Figure 5.1.1 shows the statistics yielded by our morphological classification. The left-hand panel shows the split of our passive galaxy sample into those centrals that display tidal features (features) which make up 42.4 per cent of the sample, those that show a diffuse stellar halo (diffuse) that make up 43.2 per cent of our sample, and those that are featureless that contribute 14.4 per cent of our passive galaxy sample. We note that the percentage of galaxies displaying some sort of interaction features is very similar to previous studies such as [Duc et al. \(2015\)](#) (40 per cent).

When we compare these statistics to the comparison sample of younger central galaxies in the central panel we see that the percentage of centrals classified with features remains similar at 39.2 per cent. The percentage of galaxies classified as diffuse, however, drops to 19.1 per cent and the percentage of galaxies classified as featureless increases to 41.7 per

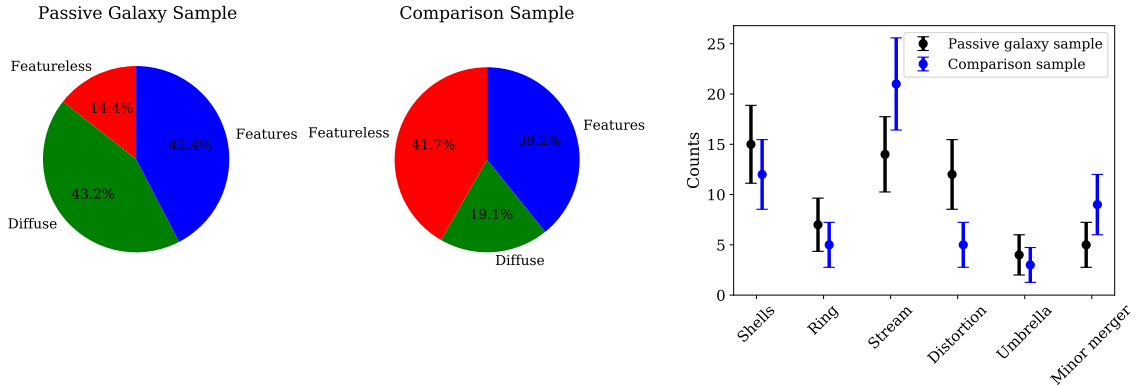


**Figure 5.1.1:** **Left-hand panel:** A pie chart of the percentage of the passive galaxy sample that was classified as either displaying visual signs of merger activity (features), no activity but a diffuse stellar halo (diffuse), or no activity at all (featureless). **Central panel:** The same as the left-hand panel but for our younger comparison sample. **Right-hand panel:** The sub-samples of galaxies that were classified as displaying visual signs of merger activity, split dependent on the type of merger activity.

cent. Assuming Poissonian errors on each sub-sample, we can calculate that the differences in the diffuse and featureless sub-samples seen between the passive and comparison samples are significant ( $> 5\sigma$ ), however are not significant ( $< 1\sigma$ ) in those galaxies classified as exhibiting features. We discuss these differences and possible scenarios for this behaviour in Section 8.2.2.

The right-hand panel shows the further morphological classification we used on the features sub-sample of galaxies. We note that some galaxies may display different kinds of features simultaneously and therefore may count many times in this specific sub-plot. We see a range of different features, from shells and significant distortions in the light distribution to minor mergers and rings. In our passive galaxy sample we see that distortions and shells are the most prevalent signs of merger activity with respect to the comparison sample. The comparison sample, on the other hand, shows an increased amount of streams compared to our passive galaxy sample, with all three signs of merger activity the most prevalent in both galaxy samples. When we calculate the Poissonian errors, we find no significant differences ( $< 1\sigma$ ) in the number of shells, rings and umbrellas, differences above  $1\sigma$  in the number of streams and minor mergers, and differences above  $2\sigma$  in the numbers of distortions. We caution, however, against over interpretation due to relatively small number statistics.

## 5.2 Colour and Stellar Mass Density Profiles of HSC Galaxies

One of the most effective ways to investigate the star formation and assembly histories of galaxies is to plot radial profiles of various properties. This can help reveal possible evolutionary scenarios which a galaxy has undergone. For example, metallicity and age profiles in the central regions may reveal inside-out star formation (e.g. [La Barbera et al. 2011](#)). The outskirts, however, are dominated by ex-situ stars according to simulations ([Davison et al.](#)

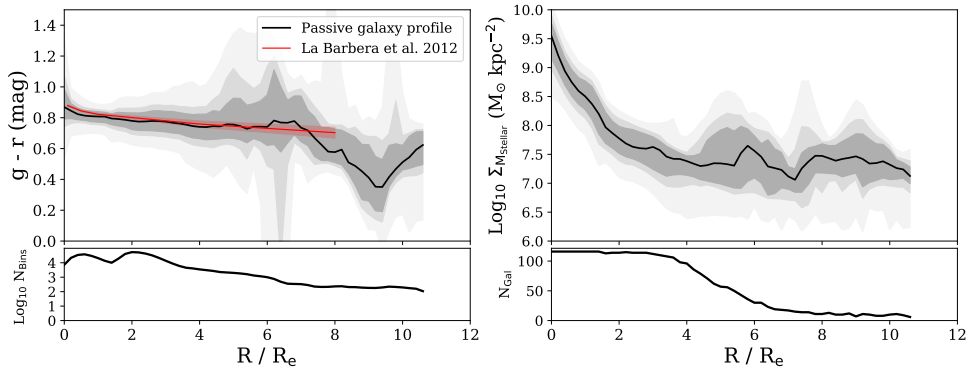


**Figure 5.2.1:** **Top left-hand panel:** The stacked radial profile (in bins of  $0.1 R/R_{\text{eff,SDSS}}$ ) of  $g-r$  colour for the 118 galaxies in our older ( $t_{90} > 6$  Gyr), passive galaxy sample. The solid black line gives the median of the distribution of each bin, while the shaded areas represent the 5<sup>th</sup>, 16<sup>th</sup>, 25<sup>th</sup>, 75<sup>th</sup>, 84<sup>th</sup> and 95<sup>th</sup> percentiles of each stacked bin. For comparison, the results from the study of [La Barbera et al. \(2012\)](#) are given by the solid red line and shaded areas. **Top right-hand panel:** The stacked radial profile (also in bins of  $0.1 R/R_{\text{eff,SDSS}}$ ) of the stellar mass surface density with corresponding percentiles, normalised by the integrated stellar mass within  $1 R_{\text{eff,SDSS}}$ . **Bottom left and bottom right panels:** The logarithm of the number of Voronoi bins and the number of galaxies as a function of radius respectively.

2020). Radial profiles out to large  $R_{\text{eff,SDSS}}$  therefore reveal the nature of accreted material ([La Barbera et al. 2012](#); [Hirschmann et al. 2015](#); [Davison et al. 2020](#)), which is the aim of this part of this study. We utilise this technique to explore the nature of the stellar material in the outskirts of our galaxy sample through the colour and stellar mass surface density profiles of the accreted material in both the passive and comparison galaxy samples.

From the Voronoi binning process we calculated an average distance for each Voronoi bin to the centre of the galaxy. Using these radii measurements, we then stacked every Voronoi bin from every galaxy in our passive galaxy sample in bins of  $0.1 R/R_{\text{eff,SDSS}}$  and constructed distributions of  $g-r$  colour and stellar mass surface density. We use the effective radius as measured by SDSS  $R_{\text{eff,SDSS}}$ , in order to be able to better compare these results to previous studies. We note that when we measure the light profiles from our HSC data, we find an average 10 per cent difference in the measured effective radii from our data and those measured from SDSS, which is in agreement with previous studies using similar datasets ([Duc et al. 2015](#)). Therefore, we do not expect biases in the results presented here from using  $R_{\text{eff,SDSS}}$ . We also add the constraint that each bin of  $0.1 R/R_{\text{eff,SDSS}}$  requires 100 Voronoi bins, to reduce statistical biases due to stochastic fluctuations. We note that very few Voronoi bins ( $< 0.1$  percent) contains pixels in multiple radii. From the distribution in each bin we calculate the median of each bin, and the 5<sup>th</sup>, 16<sup>th</sup>, 25<sup>th</sup>, 75<sup>th</sup>, 84<sup>th</sup> and 95<sup>th</sup> percentiles to construct our stacked radial profiles. In order to account for different stellar masses biasing results, we also weight each estimation in stellar mass density by the total stellar mass of its parent galaxy within  $R_{\text{eff,SDSS}}$  of each galaxy following previous studies (we note that normalising by 2 or 3  $R_{\text{eff,SDSS}}$  has a negligible difference on the results).

The top left-hand panel of [Figure 5.2.1](#) shows the  $g-r$  colour profile of our passive

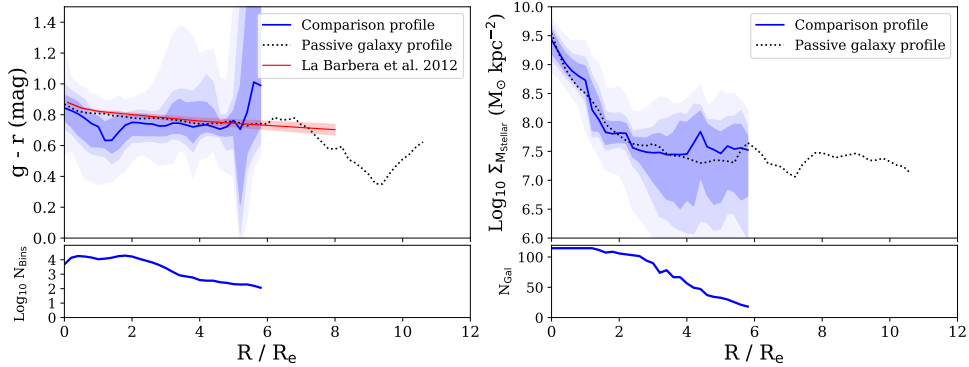


**Figure 5.2.2: Top left-hand panel:** The stacked radial profile (in bins of  $0.1 R/R_{\text{eff,SDSS}}$ ) of  $g - r$  colour for the 118 younger ( $t_{90} < 4$  Gyr) galaxies of the comparison sample. The solid blue line gives the median of the distribution of each bin, while the shaded areas represent the 5<sup>th</sup>, 16<sup>th</sup>, 25<sup>th</sup>, 75<sup>th</sup>, 84<sup>th</sup> and 95<sup>th</sup> percentiles of each stacked bin. For comparison, the results from the study of [La Barbera et al. \(2012\)](#) are given by the solid red line and shaded areas and the median of the passive galaxy sample is given by the black dotted line. **Top right-hand panel:** The stacked radial profile (also in bins of  $0.1 R/R_{\text{eff,SDSS}}$ ) of the stellar mass surface density with corresponding percentiles, normalised by the integrated stellar mass within  $1 R_{\text{eff,SDSS}}$ . The median of the passive galaxy sample is given by the black dotted line. **Bottom left and bottom right panels:** The logarithm of the number of Voronoi bins and the number of galaxies as a function of radius respectively.

galaxy sample. The black solid line shows the median value of the distribution in each bin of  $R/R_{\text{eff,SDSS}}$ , the dark grey shading shows the 25<sup>th</sup> and 75<sup>th</sup> percentiles, the mid grey the 16<sup>th</sup> and 84<sup>th</sup> percentiles and the light grey the 5<sup>th</sup> and 95<sup>th</sup> percentiles. We see a slight decrease of the order of 0.1 dex in the  $g - r$  colour in the inner  $2 R_{\text{eff,SDSS}}$ , with a very narrow distribution. As we go beyond this radius towards  $6 R_{\text{eff,SDSS}}$ , the  $g - r$  colour still declines, becoming bluer by another 0.1 dex, however the distribution experiences much greater range (up to  $\sim 0.5 - 1$  magnitude). Beyond  $8 R_{\text{eff,SDSS}}$ , the stellar material is bluer, reaching a median  $g - r$  colour of 0.4 mag.

On closer inspection of the maps and imaging data of the galaxies predominantly contributing at these radii, this material is dominated by incoming streams and from satellite galaxies in the process of minor mergers. We investigate this further in Section 5.4. We also observe similar gradual decline of  $\sim 0.1$  mag in various other colour profiles such as ( $g - i$ ,  $r - i$ ,  $i - z$ ) within  $6 R_{\text{eff,SDSS}}$ , however beyond this the  $r - i$  and  $i - z$  colour profiles continue to gradually decline rather than dropping  $\sim 0.4$  mag. We postulate that this is likely due to the material being slightly bluer due to dwarf galaxies with bluer stellar populations being accreted onto the central galaxy.

We compare these colour profiles to a previous study carried out by [La Barbera et al. \(2012\)](#). In their work they investigate the colour profiles of 674 massive early-type galaxies, with stellar masses between  $10^{10.5}$  and  $10^{11.8} M_{\odot}$ , and contained in the SDSS and United Kingdom Infrared Deep Sky Survey (UKIDSS) out to  $8 R_{\text{eff,SDSS}}$ . Their results are represented by the solid red line for the median and the red shading indicating the 16<sup>th</sup> and 84<sup>th</sup> percentiles. We find good agreement between our results and those from [La Barbera et al.](#)

(2012) as the values are well within the scatter of our distribution at almost all radii.

The top right-hand panel of Figure 5.2.1 shows the stellar mass surface density profile as yielded by the estimates of stellar mass from CIGALE. Once again the median of each distribution in a bin of  $0.1 R/R_{\text{eff,SDSS}}$  is represented by the black solid line with the 5<sup>th</sup>, 16<sup>th</sup>, 25<sup>th</sup>, 75<sup>th</sup>, 84<sup>th</sup> and 95<sup>th</sup> percentiles given by the various shading levels. We see a fairly smoothly declining profile within  $\sim 3 R_{\text{eff,SDSS}}$ , as expected, but beyond this radius we observe a flattening of the average stellar mass density profile, with some bumps. This behaviour occurs not only in the median values of the distribution but also in various percentiles of the distribution. This indicates that significant stellar material is present in the observed tidal features we see in the imaging and specifically detect and isolate using our method in Section 4.3.

The bottom right panel of Figure 5.2.1 shows the number of Voronoi bins per radius bin in log-space and the bottom right panel shows the amount of galaxies contributing Voronoi bins to each radius bin as a function of radius.

Figure 5.2.2 shows the same radial profiles for our comparison galaxy sample, with the median (in bins of  $0.1 R/R_{\text{eff,SDSS}}$ ) represented by the solid blue line and the shaded regions indicating the 5<sup>th</sup>, 16<sup>th</sup>, 25<sup>th</sup>, 75<sup>th</sup>, 84<sup>th</sup> and 95<sup>th</sup> percentiles, the same as for our passive galaxy sample in Figure 5.2.1. The median  $g - r$  colour for our passive galaxy sample is given by the dotted black line for comparison. We see in the top left panel of Figure 5.2.2 slightly bluer average colours of the order of  $\sim 0.1$  mag in the central regions of our galaxies up until  $\sim 5 R_{\text{eff,SDSS}}$ . Beyond this point, we observe a slight spike, whereby material is redder than our passive galaxy sample or the measured profiles of La Barbera et al. (2012, given by the solid red line). We note, however, that the profile beyond this point relies on a lower number of Voronoi bins, which introduces large variations. These spikes are predominantly driven by streams of accreted material and minor merger remnants, similar to the passive galaxy sample.

The stellar mass density profile of our comparison sample is presented in the top right panel of Figure 5.2.2. We observe similar behaviour to our passive galaxy sample (median represented by the dotted black line), whereby we observe a steeply declining profile in the inner parts of the galaxy before a flattening of the profile at larger radii with some bumps (median represented by the solid blue line with shaded regions showing the various percentiles of the distribution). This profile does not extend out as far as our passive galaxy sample due to lower numbers of Voronoi bins. As for Figure 5.2.1, the bottom left panel shows the logarithm of the number of Voronoi bins per galaxy radius and the bottom right panel shows the number of galaxies.

### 5.3 The Profiles Yielded from Stacked Imaging

Some previous works have carried out similar studies of the growth processes of massive galaxies, including the stellar mass content of their outskirts such as that of van Dokkum et al. (2010). In their study, they took imaging data from a number of surveys such as SDSS and their own NEWFIRM Medium Band Survey. They then stacked the galaxy images

in bins of redshift and constructed normalised, radial profiles of the stellar mass density. Their profiles showed an increase in the average stellar mass density in the outskirts of their sample with decreasing redshift, which drives the increase in effective radius and thereby the measured size of their galaxy sample. These profiles, however, are smooth in contrast to our passive galaxy and comparison galaxy profiles. This is because averaging, either through stacking or isophotal analysis, washes out or dampens the signal of specific merger features which generally have an asymmetric orientation on the sky compared to the host galaxy. To check if this hypothesis holds, we employed similar processes. We stacked our galaxy images and ran source detection, followed by Voronoi binning and SED fitting to see if we replicate similar trends to [van Dokkum et al. \(2010\)](#).

We took the galaxy images convolved to the worst seeing (as described in Section 4.3 in each band) and magnified each image to the median redshift of 0.086 using IRAF<sup>1</sup> in order to bring each galaxy onto the same physical spatial scale while conserving the flux (i.e. the sum of the total fluxes in all of the old and new pixels is equal). We normalised each flux value by the integrated stellar mass, like in [van Dokkum et al. \(2010\)](#), corrected for redshift dimming, and then stacked all images in each band, taking the median for each stacked pixel. We then applied the same Voronoi binning procedure as before, measured the  $g$  and  $r$  colours, and fitted the photometry for each Voronoi bin with an SED to yield stellar mass estimates for the stellar mass surface density profiles. We then constructed similar radial profiles as the previous section.

In order to compare these stacked image profiles with our radial profiles from Section 5.2, we also multiplied the effective radii of each galaxy by the same magnification factors yielding a median angular effective radius of 3.4 arcsec. The results are shown in Figure 5.3.1, with the solid black line representing the median with the accompanying grey shaded areas representing the same percentile limits as in Figures 5.2.1 and 5.2.2.

As stated earlier, the wings of the PSF may also have an effect on surface brightness profiles, and thereby on the colour and stellar mass surface density profiles. To investigate the effect this may have on our results, we constructed full PSFs to be convolved with our stacked galaxy image. For each galaxy in our sample we attempted to select a field star in the vicinity that was suitably isolated and reasonably bright. Altogether we found 95 suitable field stars from 118 galaxies, choosing at random one of the 95 stars as a replacement for those galaxies without a star. As the radial profiles extend to  $\sim 10 R_{\text{eff,SDSS}}$ , we cut out stellar images in each of the HSC bands which extend to these angular scales ( $\sim 30$  arcsec radius). We magnified each PSF image in the same way as its corresponding galaxy, then stacked and normalised the PSF images in each band to produce a final median PSF in each band. This constructed PSF decreases 5 orders of magnitude between the centre and a radius of 10 arcsec, qualitatively similar behaviour to previous studies investigating the effects of PSFs in detail (e.g. [Sandin 2014](#)). Beyond this radius we observe some minor bumps of 0.2 or 0.3 dex, however these peaks are still  $\sim 5$  orders of magnitude smaller than the central regions.

We then took the stacked galaxy images in each band, fitting each with a two-component profile containing a bulge and disk contribution in two dimensions. This fitting process

<sup>1</sup><http://ast.nao.edu/data/software>

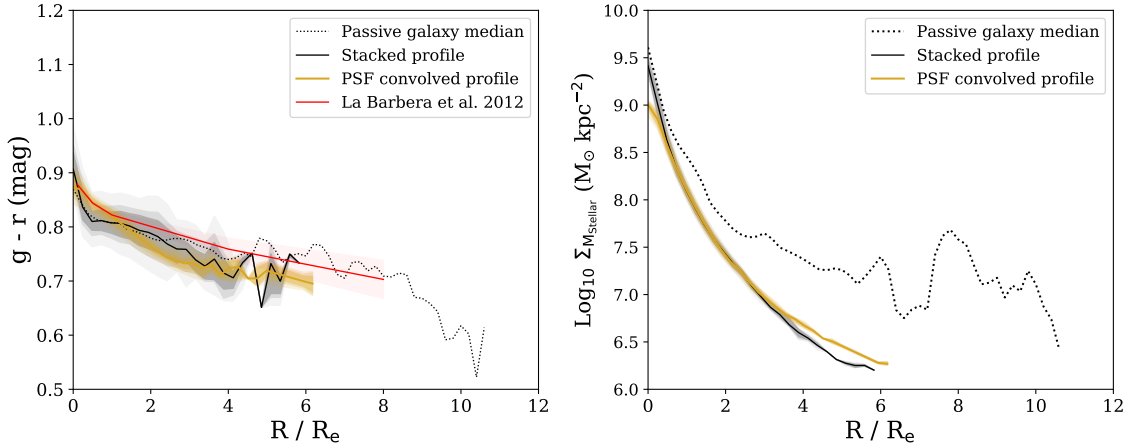


**Figure 5.3.1:** **Left-hand panel:** The  $g-r$  colour profile for our stacked galaxy. The solid black line indicates the median of the profile, with the various shadings representing the 5<sup>th</sup>, 16<sup>th</sup>, 25<sup>th</sup>, 75<sup>th</sup>, 84<sup>th</sup> and 95<sup>th</sup> percentiles of each stacked bin. The golden lines represent the stacked galaxy profile when convolved with the constructed PSF. For comparison the results of [La Barbera et al. \(2012\)](#) are indicated by the solid red line and shading and the dotted black line represents the median profile from our passive galaxies in [Figure 5.2.1](#). **Right-hand panel:** The stellar mass surface density profile for our stacked galaxy (black line) with respective percentiles and for the accounting of the constructed PSF (golden line). For comparison the observed profile in [Figure 5.2.1](#) is shown by the black dotted line.

yielded a bulge-to-total luminosity fraction of 0.85, slightly higher than our average bulge-to-total mass fraction of 0.78 measured in our sample. We find the bulge component has a Sérsic index of 8.0, whereas the disk component is fixed at an index of 1. Once again, these are slightly higher than the average values ( $n = 5.00$ ) retained from the catalogues. These slight differences are likely due to the different depths of the data from the study of ([van Dokkum et al. 2010](#)) and this one, the treatment of the PSF and slight differences in the fitting algorithms, even though both fit two dimensional bulge and disk models.

We then convolved each fitted profile with the constructed PSFs in each band, to produce final images of the stacked and PSF convolved galaxy. We ran the same process of Voronoi binning and SED fitting using `CIGALE` in order to estimate stellar mass surface densities, and subsequently used these to construct the profiles seen in [Figure 5.3.1](#). The solid golden line represents the median in each bin of  $0.1 R/R_{\text{eff,SDSS}}$  and accompanying shaded areas are as in previous figures.

We observe little difference in the  $g-r$  colour profiles in both the stacked galaxy profile (median given by the solid black line and accompanying grey shaded areas showing the various percentiles) and when convolved with the constructed PSF (median given by the golden line with corresponding shaded areas showing the various percentiles), with differences less than 0.1 mag at almost all radii. The stacked galaxy stellar mass density profile appears as a smooth decline out to  $\sim 6 R_{\text{eff,SDSS}}$ , similar to previous works. As may be expected due to the smoothing of the PSF wings, we see a deficiency of stellar mass surface density of roughly 0.5 dex in the central regions of the galaxy and some excesses of 0.2 dex in the

outskirts beyond  $5 R_{\text{eff,SDSS}}$  compared to the stacked galaxy profile. When the total stellar mass is computed by integrating the stellar mass density profiles, the differences in the total stellar mass are less than 1 per cent. We come to the conclusion that although PSF effects may contribute minorly to the stellar mass density seen in the outskirts of galaxies using our techniques from Section 4.3, they are not the main driver, meaning that the bumps seen in the stellar mass density profiles are driven by the tidal features we specifically detect.

Using the median redshift and effective radius of our sample, we can calculate an approximate median physical effective radius of our stacked profile of 5.9 kpc. We can therefore approximately compare our stellar mass surface density profile of the PSF corrected stacked (golden) sample to that of [van Dokkum et al. \(2010\)](#). We choose physical radii of 10, 20 and 30 kpc: [van Dokkum et al. \(2010\)](#) find stellar mass densities of  $\sim 10^8$ ,  $10^{7.2}$  and  $\sim 10^7 M_{\odot} \text{ kpc}^{-2}$  at 10, 20 and 30 kpc respectively, that compares to our results of  $\sim 10^{7.5}$ ,  $10^{6.8}$  and  $10^{6.5} M_{\odot} \text{ kpc}^{-2}$  at 10, 20 and 30 kpc respectively. We therefore see very similar behaviour in our profiles compared to [van Dokkum et al. \(2010\)](#), however a systematic offset of  $\sim 0.5$  dex, which may be due to different data sets (i.e. SDSS and NEWFIRM imaging data compared to HSC) or the different methods used to treat the data, such as that the study of [van Dokkum et al. \(2010\)](#) assume a [Kroupa \(2001\)](#), whereas we assume a [Chabrier \(2003\)](#) in our SED fitting.

## 5.4 The Profiles of Interaction Sub-samples

In order to further investigate the nature of the bumps in the passive galaxy stellar mass density radial profiles, we split the sample by the morphological classifications, namely the features, the diffuse, and the featureless sub-samples outlined in Section 4.2. We then plot the same radial profiles as in the two previous sections.

We see in the top left-hand panel of Figure 5.4.1 that all sub-samples have extremely similar  $g - r$  colour profiles inside  $\sim 4 R_{\text{eff,SDSS}}$ , decreasing from  $\sim 0.9$  mag in the centre to  $\sim 0.8$  mag by  $4 R_{\text{eff,SDSS}}$ . The featureless galaxies (solid red line for the median, 16<sup>th</sup> and 84<sup>th</sup> percentiles are shaded) do not extend out beyond this radius. The diffuse galaxies (solid green line for the median, 16<sup>th</sup> and 84<sup>th</sup> percentiles are shaded) increase in  $g - r$  colour by 0.1 mag to  $\sim 0.9$  mag beyond this radius. The features sub-sample (solid blue line for the median, 16<sup>th</sup> and 84<sup>th</sup> percentiles are shaded) dominates the sample number counts at high radii, and follows a similar profile to the overall passive galaxy sample (dotted black line for the median).

We see that the stellar mass surface density profiles for all sub-samples in the top right-hand panel of Figure 5.4.1. We see a fairly smooth decrease of the stellar mass surface density in the central regions, until  $\sim 3 R_{\text{eff,SDSS}}$ . For the featureless sub-sample, this trend appears to generally decrease, but cuts off at  $4 R_{\text{eff,SDSS}}$ , meaning that they do not contribute to the flattening of the stellar mass surface density profiles we observe. For the diffuse sub-sample, we see a flattening off of the profile beyond  $3 R_{\text{eff,SDSS}}$ , until a truncation in the stellar mass surface density at  $6 R_{\text{eff,SDSS}}$ . The features sub-sample (solid blue line for the median, 16<sup>th</sup> and 84<sup>th</sup> percentiles are shaded) shows very similar behaviour to the

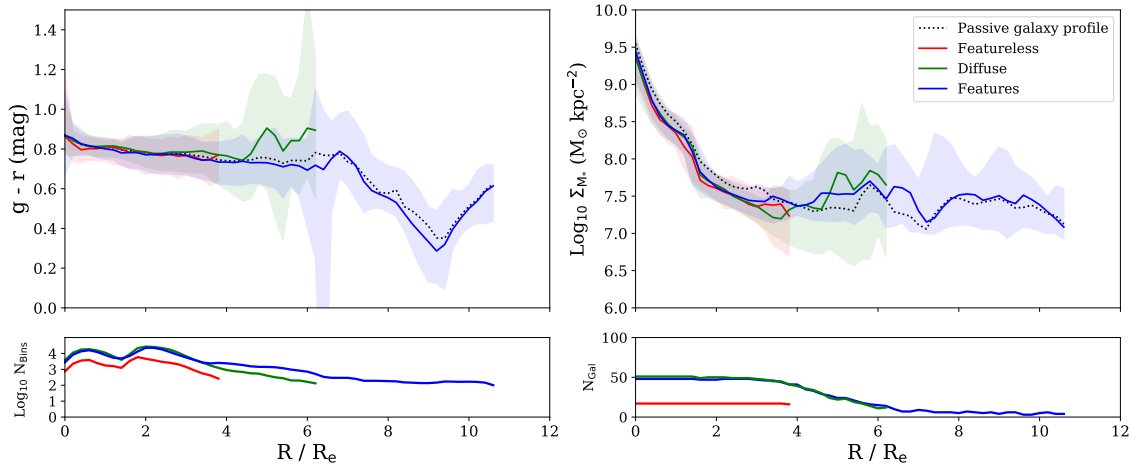


**Figure 5.4.1: Top left-hand panel:** The  $g - r$  colour profiles of those galaxies that display signs of merger activity (features, median represented by the blue solid line and 16<sup>th</sup> and 84<sup>th</sup> percentiles represented by the blue shaded region), those that do not display clear signs of merger activity but a diffuse stellar halo (diffuse, median represented by the green solid line and 16<sup>th</sup> and 84<sup>th</sup> percentiles represented by the green shaded region) and those that display no merger activity or diffuse halo (featureless, median represented by the red solid line and 16<sup>th</sup> and 84<sup>th</sup> percentiles represented by the red shaded region). **Top right-hand panel:** The stellar mass density profile for each of the three aforementioned sub-samples. **Bottom left and bottom right panels:** The logarithm of the number of Voronoi bins and the number of galaxies as a function of radius respectively for each sub-sample.

diffuse sub-sample, initially flattening off at  $3 R_{\text{eff,SDSS}}$ . However, beyond  $6 R_{\text{eff,SDSS}}$ , this sub-sample dominates the excess material we detect, remaining flat with some bumps. On visual inspection, these bins are dominated by galaxies that are undergoing minor mergers or have stellar streams. This shows that the stellar material in the outskirts of our passive galaxy sample is dominated by the tidal features seen in these galaxies that are indicative of recent galaxy interactions and/or mergers. As for Figures 5.2.1 and 5.2.2 the bottom left and bottom right panels show the logarithm of the number of bins and the number of galaxies.

We see that in both the passive galaxy sample and the comparison sample there is significant overlap in redshift between the three sub-samples and that any differences in the average redshift are minimal ( $\Delta z < 0.002$ ). We also searched imaging data from the HSC ultra deep survey fields for galaxies in both samples which we classified as featureless. Although only 6 galaxies were available in these fields, none displayed any low surface brightness features when using imaging two orders of magnitude deeper. We argue that this shows that we are not significantly redshift or sensitivity biased in our morphological classification.

In summary: using our method of specifically detecting and isolating low redshift, massive central galaxies, and their surrounding LSB features, we find a number of results. We firstly find widespread minor merger activity, across all galaxy types. We also find similar  $g - r$  colour profiles to previous studies in the central regions of our galaxy sample and at large radii we find much greater variance in the colour of the stellar material in LSB features. When we construct stellar mass surface density profiles using our method, we find

expected smooth and steep declines in the central regions with a flattening at outer radii, indicating the presence of significant stellar mass. When splitting by interaction types, we find that the galaxies which display minor merger activity are responsible for the majority of the stellar mass in the outskirts of galaxies. We also find that previous methods cannot quantify the properties due to the techniques used. We discuss these results and present our interpretation on how this material connects to the minor merger growth scenario further in Section 8.2.2.

*"Most people, after one success, are so cringingly afraid of doing less well that they rub all the edge off their subsequent work."*

Beatrix Potter (author of the tales of Peter Rabbit) -  
1866 to 1943

# 6

## Data and Methods for the Radial Gradients of Central Galaxies

Having now constrained the stellar mass assembly of a sample of low redshift, massive, central galaxies and taken a sub-sample of these galaxies and quantified their merger activity and LSB features, we now turn our attention to the stellar population properties of a further subset of these galaxies. We present the IFU data, the stellar population models and the stellar population fitting and techniques in this Chapter. This Chapter is contained in the study of Jackson et al. (in prep.). Contributions by collaborators to this Chapter are as follows: Dr. Anna Pasquali and Dr. Francesco La Barbera for discussion of the `STARLIGHT` fitting code and suggestions for manually correcting bad fits; Ms Alina Böcker for the advice on the pPXF fitting process and for fitting the resulting age and metallicity grids with empirical models in order to estimate the in- and ex-situ fraction of stellar material from her own method presented in [Boecker et al. \(2020\)](#).

### 6.1 The SAMI Survey and Data

The Sydney - Australian Astronomical Observatory Multi-Object Integral Field Spectrograph (SAMI) Galaxy Survey ([Croom et al. 2012](#); [Bryant et al. 2015](#)) is a spatially resolved, extragalactic IFU spectroscopic survey. The survey has observed  $\sim 3000$  nearby ( $z \lesssim 0.1$ ) galaxies using the 4 meter Anglo-Australian Telescope at the Siding Spring Observatory. Spectra are available in both the blue (3650 - 5800 Å) and red parts (6240 - 7460 Å) of the optical spectrum, with dispersions of  $1.05 \text{ Å pixel}^{-1}$  and  $0.596 \text{ Å pixel}^{-1}$  and a FWHM of  $\sim 2.6 \text{ Å}$  and  $1.6 \text{ Å}$  respectively. Each IFU bundle contains 61 fibres, each spanning a 1.5 arcsec diameter, and are arranged in a configuration that has a  $\sim 15$  arcsec sky coverage. The

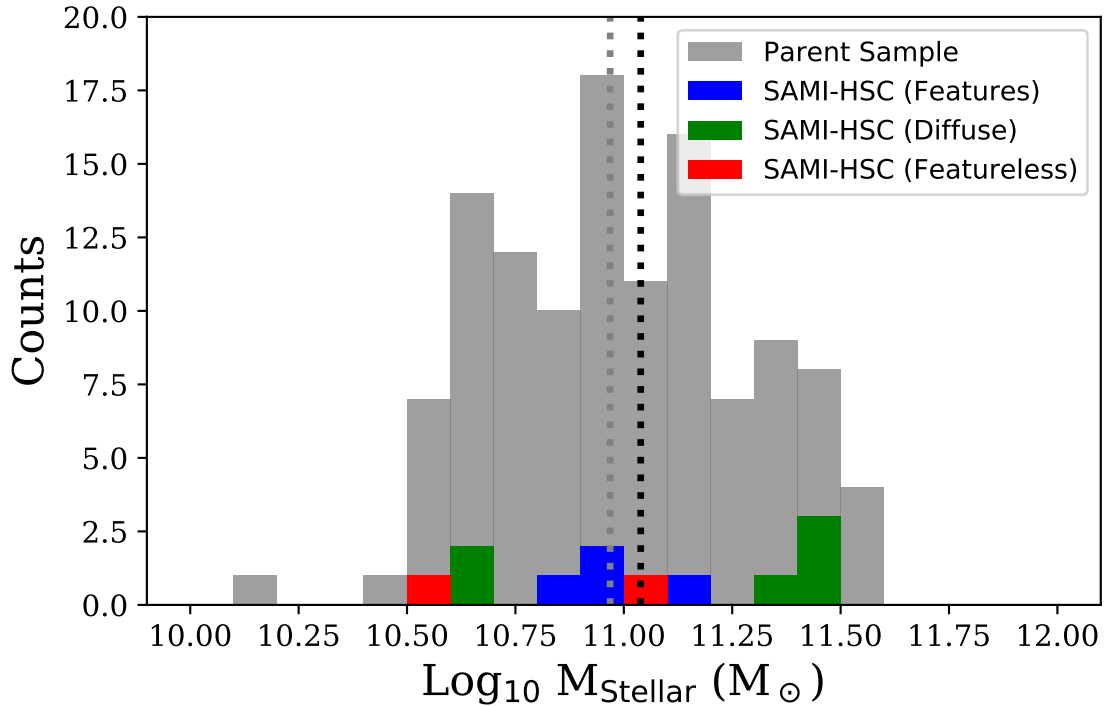


**Figure 6.1.1:** The distribution in stellar mass of the parent sample taken from part II of this work (Chapter 4, grey histogram) and the sub-sample used for part III of this work split into the three morphological classes described in Section 4.2 (referred to as the SAMI-HSC sample, coloured histograms). We see that the SAMI-HSC sample covers a wide range of stellar masses with a median stellar mass less than 0.1 dex more than the original HSC parent sample.

SAMI survey is designed to observe target galaxies with a broad range of stellar masses ( $10^{7.6} < M_{\text{Stellar}} < 10^{11.6}$ ), morphologies (late-type galaxies through to early-type galaxies) and environments (from field to cluster environments).

We take the parent sample of galaxies from both the passive and comparison galaxy samples in Chapters 4 and 5. We then cross-matched this parent sample of 236 galaxies with the catalogues contained in the SAMI IFU survey DR2 (Scott et al. 2018) using a 5 arcsecond matching radius in right ascension and declination. We note that no extra galaxies are contained in the DR3, as this data release focuses almost exclusively on cluster environments not contained in the HSC fields.

This final sample, hereafter known as our SAMI-HSC sample, is presented in Figure 6.1.1. The SAMI-HSC sample contains 15 galaxies, 11 of which are contained in the older, passive sample and 4 of which are in the younger comparison sample. 14 out of the sample were visually classified in Section 4.2 as displaying early-type morphologies (E or S0) and only one with a late-type morphology. 6 of these galaxies were further visually classified as displaying some form of interaction signatures (such as tidal streams, shells etc.), 7 were classified as

displaying no features but a diffuse stellar structure in the outskirts and 2 were classified as showing no signs of interaction or diffuse stellar structure. These sub-samples are labelled as features, diffuse and featureless respectively, the same as in Chapters 4 and 5. The distribution in stellar mass of the parent sample (grey) and our SAMI-HSC sample split by the interaction morphologies outlined above and in Section 4.2 (coloured histograms) can be seen in Figure 6.1.1. We see that our SAMI-HSC sample covers almost the full range of stellar masses of the parent sample from  $10^{10.5} - 10^{11.5} M_{\odot}$ , with a median stellar mass of  $10^{11.05} M_{\odot}$ , less than 0.1 dex greater than the median of the parent sample.

Following the procedure of Ferreras et al. (2019), we selected the standard SAMI IFU datacubes, correcting the spectrum of each spaxel for the radial velocities of the stellar populations as derived by van de Sande et al. (2017a,b) and the redshift to bring each spectrum to rest-frame wavelengths. Reddening due to dust in the Milky Way foreground was corrected as advised in the data sets using the extinction law of Cardelli, Clayton & Mathis (1989). We then grouped spaxels according to the circular annuli for the SAMI data (see Green et al. 2018; Scott et al. 2018, for more details) of which there are 5 for each galaxy, and stacked the spectra, summing the fluxes and calculating the error by adding the noise in quadrature from the provided variance spectra. We exclude annuli under a  $S/N$  of 20 (similar to Gallazzi et al. 2005) in order to minimise the uncertainties in the stellar population fitting process outlined in the following section and to remove poor fits to the data. This removes 16 out of the 75 original annuli, almost exclusively the outer annulus, from our sample leaving 59 spectra from 15 galaxies.

## 6.2 Stellar Populations and STARLIGHT

In order to estimate the stellar properties of the stacked annuli spectra from our SAMI-HSC sample, we use Simple Stellar Population (SSP) model predictions using the Medium-resolution Isaac Newton Telescope library of empirical spectra (MILES, Sánchez-Blázquez et al. 2006; Vazdekis et al. 2010; Falcón-Barroso et al. 2011). This library contains  $\sim 1000$  stars with spectra taken from the 2.5 metre Isaac Newton telescope in the optical range of 3525 - 7500 Å with a FWHM of 2.5 Å.

We selected the MILES models based on the BaSTI isochrones with the base models, whereby  $[\text{Mg}/\text{Fe}] = 0.0$ , and assuming a Chabrier (2003) IMF. Following the study of Ferreras et al. (2019), we restricted the range of the ages of the models to between 1 and 14 Gyr, in 1 Gyr intervals, as the majority of our galaxies are old ( $t_{90} > 6$  Gyr). The IFU spectra also cover only the central regions of each galaxy, which we expect to have old stellar ages and be metal-enriched. We included, however, an additional population with an age of 100 Myr, in case the interactions that some of the galaxies in our sample are undergoing due to minor mergers have triggered some minor star formation. We also constrained the metallicity values of the models to  $[\text{Z}/\text{H}] = [-0.96, -0.66, -0.35, -0.25, +0.06, +0.15, +0.26]$ , as from previously derived relations between stellar mass and metallicity in other studies, we do not expect the majority of the stellar material in our sample to be metal-poor (Gallazzi et al. 2005, 2020). We then convolved the MILES spectra to the resolution of the SAMI data,

with an added component corresponding to a velocity dispersion of  $100 \text{ km s}^{-1}$  so as to account for any extra systematic biases.

We use the STARLIGHT code (Cid Fernandes et al. 2005; Mateus et al. 2006; Asari et al. 2007) in order to find the best combination of model spectra. STARLIGHT retrieves the SFH of galaxies by fitting the observed flux spectrum, together with the associated errors on the flux, with a mixture of  $N$  SSPs from the bases described above and estimating the best weighted combination of the input models. From the best weighted combination of fits, a light-weighted age, metallicity and stellar mass can be estimated.

For the fitting process, we masked the standard SDSS emission line regions of Ne[III] and O[III] (at  $\lambda \sim 3870$ , and  $4990 \text{ \AA}$  respectively) and significant sky lines in the rest-frame spectra ranging between  $\sim 5100$  and  $5300 \text{ \AA}$  depending on the redshift of the galaxy. This reduces emission lines biasing the stellar population estimates. We limit the fit of the rest-frame spectra between the wavelengths of  $3800 \text{ \AA}$  and  $5400 \text{ \AA}$  (or the end of the spectrum if it does not have wavelength coverage up to this wavelength) in order to avoid slight problems with the flux calibration observed at the blue end of each spectrum. We use the standard set up for most of the parameters in the fitting configuration (see e.g. Cid Fernandes et al. 2005, for more details). We select the Cardelli et al. (1989) extinction law for consistency between the models and observations and an intermediate set up for the number of Markov Chains = 7 and First Fits = 5 (as standardised in Cid Fernandes et al. 2005), as a setup with more chains yields no significant improvement on the estimation of the stellar population parameters while adding significant computation time. We re-fit four of our spectra manually in the wavelength range  $4000 \text{ \AA} - 5200 \text{ \AA}$ , due to significant systematic residuals found between the observed spectra and best-fit models at both the blue and red ends of the respective spectra.

An example fit can be found in Figure 6.2.1, with further example fits of different annuli found in Figure 6.2.2. In the top panel of Figure 6.2.1, we show the normalised flux as a function of wavelength of the observed spectra (black solid line) and the best-fitting model (red solid line). The shaded grey regions represent the masked regions. The mid panel of Figure 6.2.1 shows the residuals between the observed spectrum and the best-fitting model (black points), with the red line representing zero difference. The bottom panel of Figure 6.2.1 shows some of the parameters and estimates of the fits such as the signal-to-noise, the estimated age, the estimated metallicity etc. The same applies for each sub-plot of Figure 6.2.2 where from top left to bottom right we have different galaxies (first number of each title) and different annulus (ranging from 0 for the central annulus to 4 for the furthest possible annulus, indicated by the second number). The bottom right subplot of Figure 6.2.2 also includes one of the galaxies which had to be fit manually between  $4000$  and  $5000 \text{ \AA}$  due to flux calibration issues at the red and blue ends of the spectrum.

As STARLIGHT does not provide an error on each estimate of the stellar population properties, we estimate the uncertainties on our fits in the following manner: We take the residuals between the observed and best-fitting spectra and randomly assign these residuals additively to the flux at a different wavelength (excluding the masked regions in the whole process). This also has the advantage of negating any systematic biases contained in the observed spec-

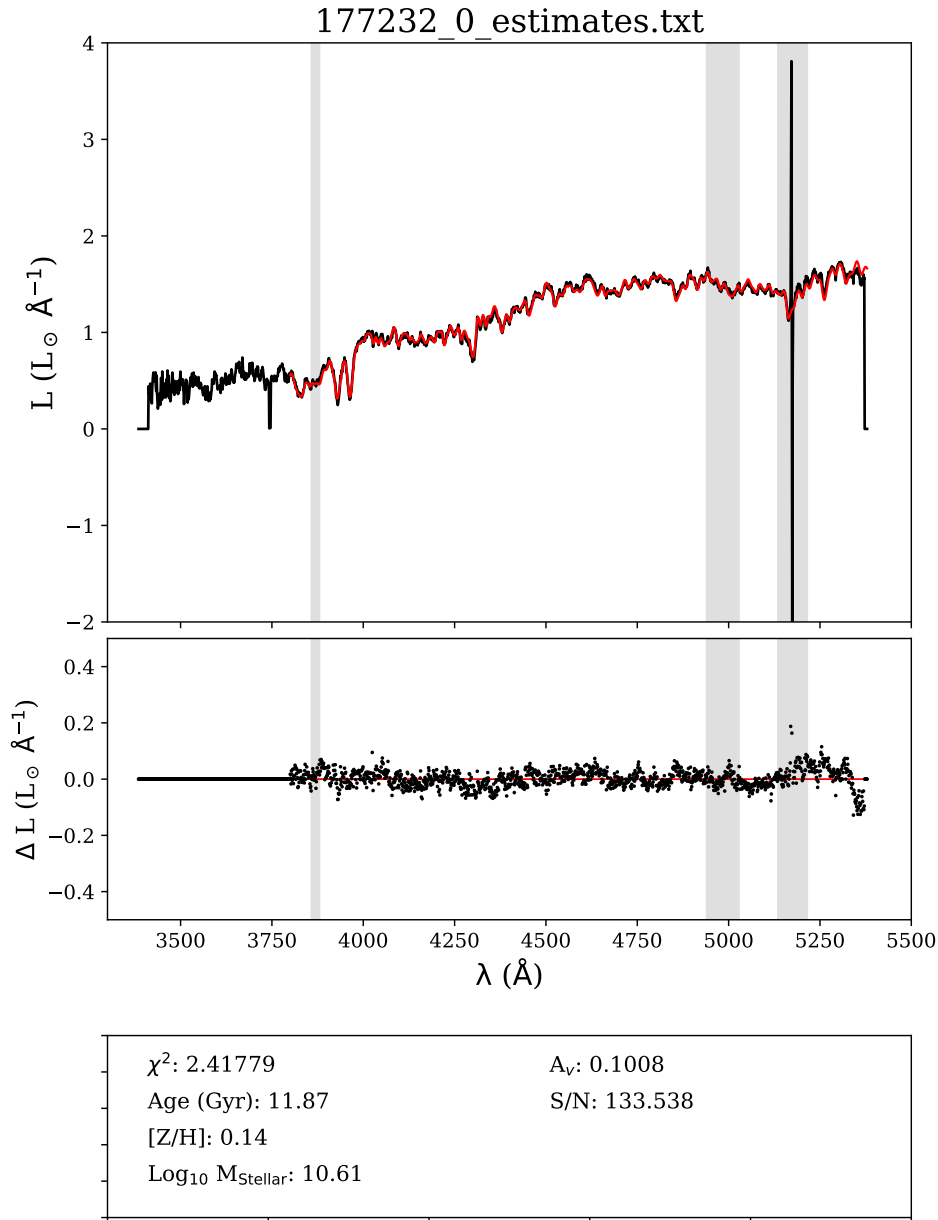


**Figure 6.2.1:** An example full spectrum fit from STARLIGHT on one of the galaxy annuli. **Top panel:** The normalised, observed spectrum is indicated by the black solid line, with the best-fitting spectrum represented by the red solid line. The shaded regions indicate masked regions in the fitting procedure. **Middle panel:** The residuals of the fit are indicated in black, with the red line representing 0 difference and the shaded regions indicating the masked regions in the fit. **Bottom panel:** The estimation of the stellar population properties such as the stellar mass, light-weighted stellar age, metallicity, and internal extinction as modelled by a Calzetti et al. (2000) extinction law.

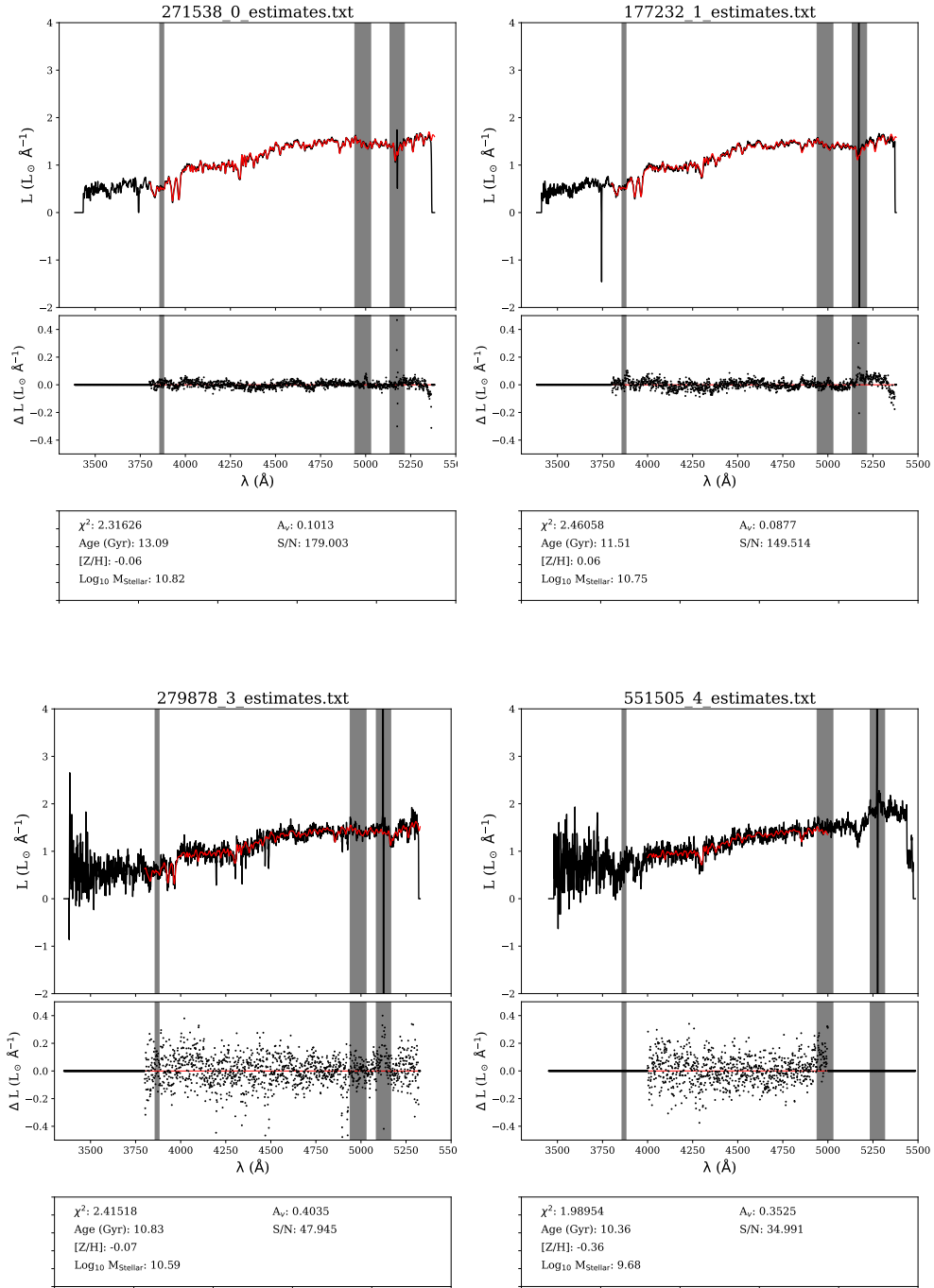


**Figure 6.2.2:** 4 further examples from STARLIGHT of fits for various galaxies (denoted by the first number in the title) at different annuli (indicated by the second number in the title). The scheme for each panel in each subplot is the same as in Figure 6.2.1. The bottom right panel shows one of the annuli for which we had to manually fit between 4000 and 5000  $\text{Å}$  due to flux calibration issues at the blue and red ends of the spectrum.

tra from the flux calibration. We repeat this process 100 times, and fit each of the 100 spectra again to extract the estimates on the weighted best-fitting age and metallicity. From these 100 estimates, a probability distribution can be built and the  $1\sigma$  scatter on the distributions used as the uncertainties on the estimates of age and metallicity.

### 6.3 The In- and Ex-Situ Fractions of Stars (via [Boecker et al. 2020](#))

As outlined in Section 1.3, significant progress has been made in the realm of simulations on studying the fraction and distribution of in- and ex-situ stars within a large sample of galaxies ([Oser et al. 2010, 2012](#); [Hirschmann et al. 2015](#); [Davison et al. 2020](#); [Remus & Forbes 2021](#)). Relatively little progress, however, has been made so far in observations. This is due to the thorough mixing of in- and ex-situ stars and the multiple degeneracies this can cause.

Multiple techniques, such as the use of kinematic modelling ([Zhu et al. 2020](#)), surface brightness profile decomposition ([Spavone et al. 2017](#)) or the accretion of globular clusters ([Kruijssen et al. 2019](#)) are currently being developed with the potential to overcome some of these problems. The technique which we use for this research is presented in the study of [Boecker et al. \(2020\)](#), which we outline here, however refer the reader to the study of [Boecker et al. \(2020\)](#) for further details.

In the technique presented by [Boecker et al. \(2020\)](#), each galaxy (or IFU annulus in the case of this study) spectrum is initially fitted using the The Penalized Pixel-Fitting code (pPXF [Cappellari 2017](#)) in conjunction with the MILES stellar population library ([Sánchez-Blázquez et al. 2006](#); [Vazdekis et al. 2010](#); [Falcón-Barroso et al. 2011](#)). This is a similar process to that described in Sections 1.1 and 6.2. An example is presented in the top panel of Figure 6.3.1, whereby the black line represents the observed spectrum and the red line represents the best-fitting model. The grey shaded areas in Figure 6.3.1 indicate masked regions not used in the fitting process and the green points show the residuals of the fit. The fitting process yields the weighted fractions of the best-fitting combination of stellar populations in age and metallicity phase space. The distribution of the weighted fractions, however, can be sparsely populated due to a number of issues such as the degenerate nature of stellar populations or noise driven biases. To circumvent issues such as these, pPXF has the option to apply a suitable regularisation matrix for the spectral fitting. This has the effect that the weights of neighbouring stellar populations are smoothed out (see [Boecker et al. 2020](#), and references therein for more details). This provides a more accurate, realistic and continuous distribution of stellar population estimates in age and metallicity, as can be seen in the mid panel of Figure 6.3.1, whereby we have the best-fitting combination of stellar populations in age and metallicity space and are colour coded by the weighted fraction of each population (colour bar to the right of the main panel).

To link the regularised, weighted grids in age and metallicity phase space produced by the fitting process to sources of ex-situ material, a number of empirical models are implemented. These models assume, to first order, a leaky box model to describe the metallicity distribution

function and the age - metallicity relation (AMR) of the galaxy population.

The chemical enrichment of the models is described as a function of the mass-dependent metallicity yield and gas fraction. The mass-dependent metallicity yield is based on the positively correlated trends presented in [Leaman et al. \(2013\)](#) at the low stellar mass end before a turnover at a critical stellar mass to account for the flattening of the mass - metallicity relation at stellar masses  $\sim 10^{10} M_{\odot}$ . The gas fraction, on the other hand, is dependent on the time by which the galaxy has formed its in-situ stars, denoted as the formation time. The formation time is itself dependent on the final stellar mass of the galaxy and allows for various lengths of the in-situ burst. The constructed empirical models are then compared to the regularised grid of ages and metallicities yielded by the fitting of the observed spectra. This is also seen in the mid-panel of [Figure 6.3.1](#), where the various coloured lines indicate different satellite galaxy masses, corresponding to the colour bar above the panel.

The fractions of ex-situ stars are then estimated by integrating the estimates of the weighted mass fractions contained underneath the constructed empirical models (i.e. we integrate the area under each curve in increasing stellar mass successively to estimate the total fraction delivered by satellites of a certain stellar mass and below) and multiplying by the total stellar mass of the galaxy. In this way, a cumulative fraction of stellar mass delivered by satellites of a certain stellar mass can then be estimated. An example of the results of this process are seen in the bottom panels of [Figure 6.3.1](#), whereby the bottom left panel shows the cumulative fraction of the total stellar mass contributed to by a satellite of a given stellar mass. The bottom right panel shows the amount of galaxies needed to account for the accreted mass (i.e. the mass function of galaxies which contribute to the ex-situ stars in each galaxy annulus). The grey line in each panel shows the cut-off point ( $N_{\text{Sat}} = 1$ ) at which all mass above this point must be in-situ, as satellite galaxies above this point would deliver too much mass for the scenario to be physically viable. The grey line in the bottom left panel of [Figure 6.3.1](#) shows the cumulative estimate of the total fraction of stars accreted. The point at which the satellite function intersects the  $N_{\text{Sat}} = 1$  line in [Figure 6.3.1](#) indicates the mass of the most massive accreted satellite. Further examples of the fitting process for a variety of annuli are given below in [Figure 6.3.2](#), although we remove the mass function, as we do not utilise this estimate in this work.

For our work here, we assume the same IMF and isochrones as for our fitting with STARLIGHT in [Section 6.2](#) to avoid biasing our results, however due to the regularisation techniques we cannot avoid using the full MILES spectral library (i.e. not just the specific age and metallicity ranges). [Boecker et al. \(2020\)](#) have shown, however, that this does not have a significant effect on the average estimates of the ages and metallicities. We discuss systematics in the fitting process further in [Section 8.3](#) and present a comparison of different fitting methods in [Appendix A.4](#).

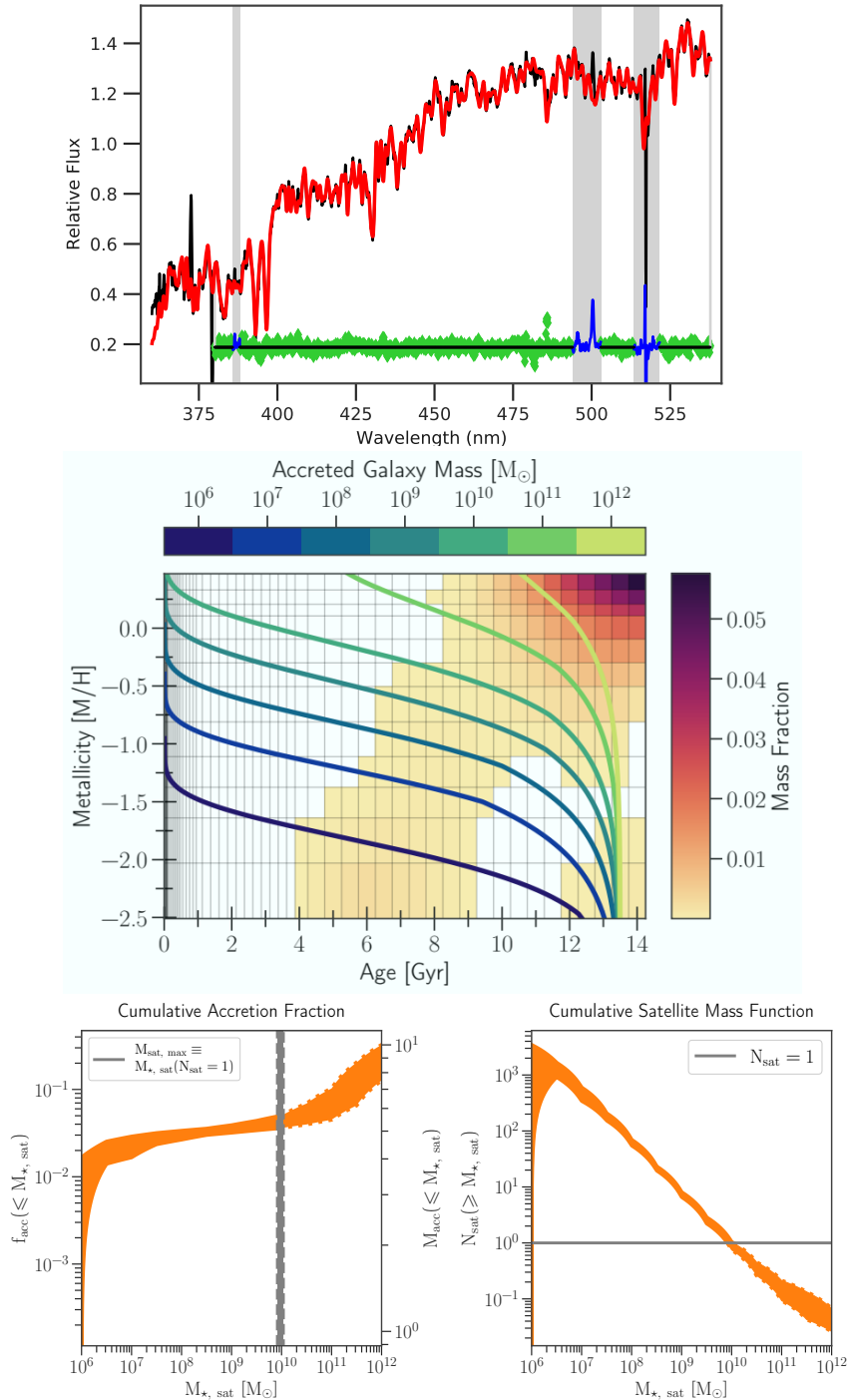


**Figure 6.3.1:** An example of the various stages of the fitting process utilised to estimate the in- and ex-situ fraction of stars for our galaxy annuli. **Top panel:** The fitting of the spectra using pPXF, whereby the observed spectra is represented by the black line and the best-fitting model as yielded by pPXF is represented by the red line. Masked areas not used for the fits are represented by the grey shaded areas and the residuals of the fit are indicated by the green points. **Middle panel:** The weighted fractions of the best-fitting combination of stellar population as a function of age and metallicity are indicated by the colour bar to the side. The constructed empirical models of satellite galaxies to estimate the accreted fractions are represented by the coloured lines, corresponding to the colour bar immediately above the subplot. **Bottom left panel:** The ex-situ weighted fraction of stars as a function of the satellite mass. The grey line gives the cumulative total accretion fraction. **Bottom right panel:** The mass function of satellite galaxies which account for the fractions in the bottom left panel. The point at which the mass function intersects the  $N_{\text{Sat}} = 1$  line yields an estimate on the largest accreted satellite.

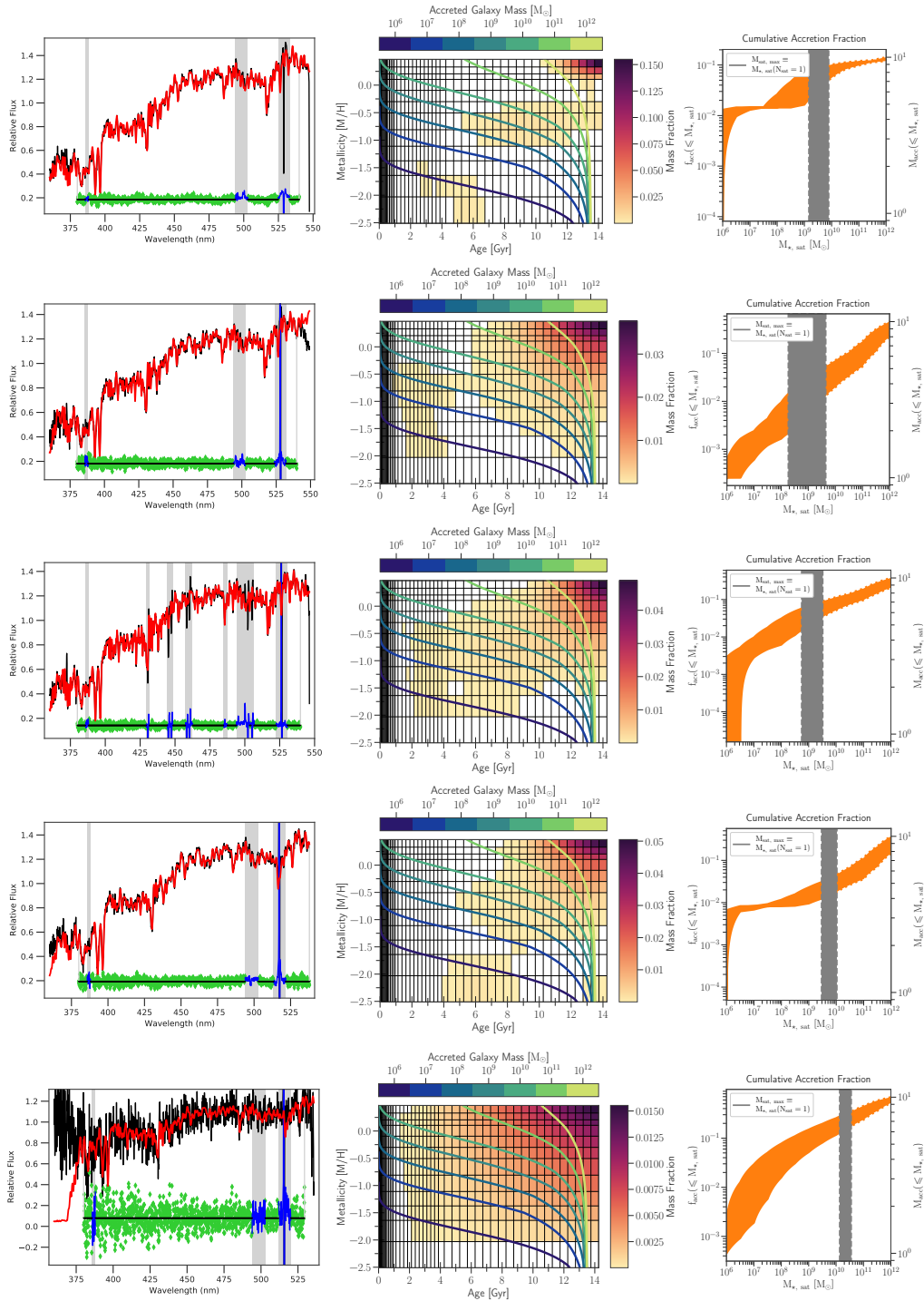


**Figure 6.3.2:** Further examples of the process utilised to estimate the in- and ex-situ fraction of stars. Each row represents the fitting process for a different galaxy and annulus. **First panel of each row:** The fitting of the observed spectra (black solid line) with pPXF, resulting in the weighted combination of the best-fitting models (red solid line). The grey shaded areas indicated masked areas not used for the fitting process and the green points represent the residuals between the observed spectra and fits. **Middle panel of each row:** The weighted fractions of the best-fitting combination of stellar models (colour coded on the right), with the constricted empirical models of satellite galaxies indicated by the coloured lines (colour bar at the top). **Right-hand panel:** The ex-situ cumulative fraction of stars as a function of satellite mass, obtained by integrating the area under each of the empirical models. The total ex-situ fraction is calculated by the intersection of the orange and grey lines.

*"But soon as Luke, full ten years old, could stand  
Against the mountain blasts; and to the heights,  
Not fearing toil, nor length of weary ways,  
He with his Father daily went, and they  
Were as companions, why should I relate  
That objects which the Shepherd loved before  
Were dearer now? that from the Boy there came  
Feelings and emanations—things which were  
Light to the sun and music to the wind;  
And that the old Man's heart seemed born again?  
Thus in his Father's sight the Boy grew up:  
And now, when he had reached his eighteenth year,  
He was his comfort and his daily hope."*

William Wordsworth - Michael. A pastoral Poem.  
1909.



## Results III - The Stellar Population Radial Gradients of Central Galaxies

Having set out our methods into researching the stellar populations of low redshift, massive, central galaxies, we now present the results in the form of radial gradients. We will also examine how these may or may not link to the interaction classification of each galaxy. We will also present the in- and ex-situ stellar mass fraction of the sample. This Chapter is contained in the study of Jackson et al. (in prep.). Contributions by collaborators to this Chapter are as follows: Dr. Anna Pasquali, Dr. Francesco La Barbera and Ms Alina Böcker for the discussion of tests and plots throughout and the discussion of results.

### 7.1 The Age and Metallicity Profiles of SAMI-HSC Galaxies

As outlined in the introduction of this thesis (Chapter 1), radial gradients of stellar population properties, such as age or metallicity profiles, may reveal much about a galaxy's assembly and evolution. However, due to the limited amount of galaxies we used in this analysis, a significant scatter in the profiles in age and metallicity is present. The problems associated with low sample statistics and therefore stochastic fluctuations are further exacerbated by a limited number of annuli per galaxy, as outlined in Section 6.1, whereby galaxies have between 3 and 5 annuli, each at various radii with respect to other galaxies. When binning in radius and calculating average values of age and metallicity to provide an average profile, the average trend is driven by stochastic fluctuations, rendering a comparison to other studies hard.

In order to give a better indication of our SAMI-HSC galaxy sample and the average trends, we first plot the individual profile of each galaxy in age and metallicity. We then

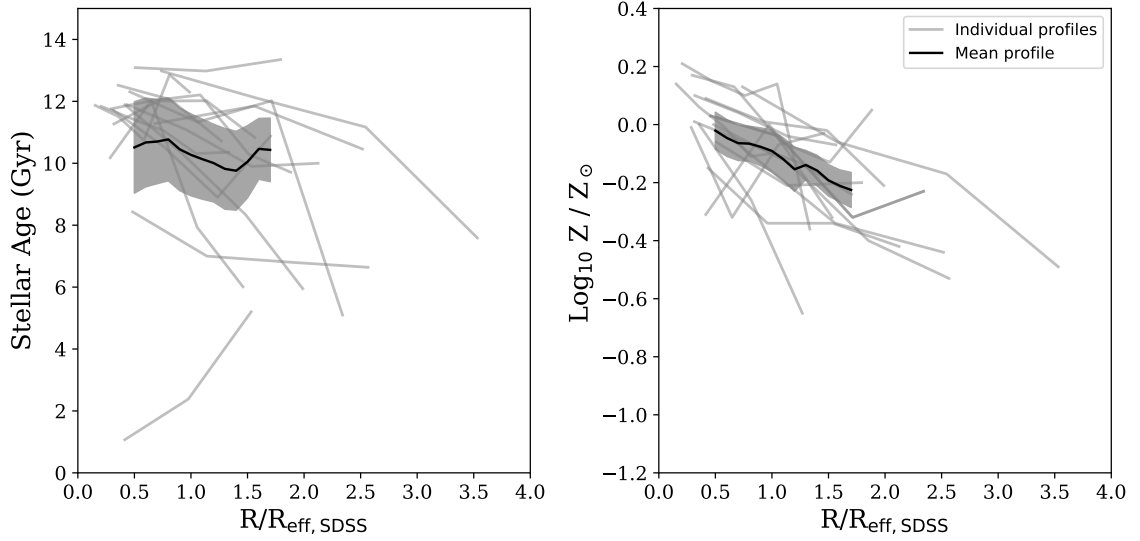


**Figure 7.1.1:** **Left panel:** The light-weighted stellar age profiles of our individual SAMI-HSC galaxies (indicated by the grey lines) compared to the interpolated average (solid black line) and the scatter in each bin in radius (shaded areas). We see a fairly flat gradient in stellar age. **Right panel:** The estimated metallicity gradients of our individual SAMI-HSC galaxies and interpolated average (scheme same as for the stellar ages). We see a smoother profile and a slight decrease in the metallicities, with a lower relative scatter in the profile compared to the stellar age profiles.

linearly interpolate each profile in age and metallicity in bins of  $0.1 R/R_{\text{eff,SDSS}}$  and calculate the mean, requiring at least half of all galaxies to contribute to the mean at any one point. The corresponding error is calculated as the sum of the quadrature of the associated errors divided by the square root of the number of errors in that bin. These average trends are indicated by the solid line in each panel of Figure 7.1.1, with the scatter indicated by the shaded regions.

We see in the left hand panel of Figure 7.1.1 that the average light-weighted stellar age of our sample is fairly flat at  $\sim 10.5$  Gyr with variance between 10 and 11 Gyr. These variations, however are much smaller than the uncertainties, which can be of up 1.5 Gyr. We see in the right-hand panel of Figure 7.1.1 that the average logarithmic metallicity decreases from  $\sim 0.0$  or approximately solar at  $0.5 R_{\text{eff,SDSS}}$  to  $\sim -0.3$  at  $2 R_{\text{eff,SDSS}}$ . We also see a slightly smoother behaviour in the average metallicity profile than for the age profiles and a relatively smaller uncertainties of  $\sim 0.05 - 0.1$  dex.

Comparing to previous studies, flat age and shallowly declining metallicity gradients are expected in galaxies in the stellar mass range of our SAMI-HSC sample (Sánchez-Blázquez et al. 2014; Goddard et al. 2017a). We take the study of Goddard et al. (2017b) for comparison. In their study, Goddard et al. (2017b) find light-weighted age gradients of  $-0.07 \pm 0.01$  per  $R_{\text{eff}}$  and light-weighted metallicity gradients of  $-0.13 \pm 0.01$  per  $R_{\text{eff}}$ . In comparison we find a gradient of  $\sim -0.05$  per  $R_{\text{eff}}$  (calculated from a drop from 10.51 Gyr to 10.43 Gyr in the light-weighted stellar ages between  $0.5$  and  $2 R/R_{\text{eff,SDSS}}$ ). When considering

the errors on our mean stellar age gradient, however, the trend of [Goddard et al. \(2017b\)](#) is well within the scatter of our observed sample. We observe a gradient in the light-weighted stellar metallicities of  $\sim -0.13$  per  $R_{\text{eff}}$  (calculated from a drop from  $-0.02$  to  $-0.22$  between  $0.5$  and  $2 R/R_{\text{eff,SDSS}}$ ). This is in agreement with the expected decrease from the trends found in [Goddard et al. \(2017b\)](#). We caution for these results and the following sections, however, about over interpretation of these trends due to the small size of our SAMI-HSC galaxy sample.

## 7.2 The Stellar Mass Density Profiles of SAMI-HSC Galaxies

One of the main points of focus in Chapter 5 was the stellar mass surface density profiles of galaxies within HSC, as estimated using multi-band imaging data from HSC in conjunction with SED fitting using CIGALE. We showed that the central regions of our galaxy sample display a fairly smooth, steeply declining profile, before specifically detected and isolated merger features cause a flattening of the stellar mass surface density profiles beyond 3 effective radii with some excesses/bumps. As STARLIGHT yields an estimate for the stellar mass, using the distances of the galaxies and the pixel coverage of each spectra we can also calculate an estimated stellar mass surface density profile for each galaxy. These individual profiles can then be compared to the mean profile, calculated in the same manner as the profiles in Section 7.1, and the median profile of our SAMI-HSC galaxies taken from the SED fitting process of Chapter 4. This is shown in the left-hand panel of Figure 7.2.1.

We first note a significant variance in the individual profiles, given by the grey lines in Figure 7.2.1, although all profiles show a declining behaviour. When we plot our interpolated average, indicated by the solid black line with corresponding uncertainties indicated by the shaded regions, we see a smooth declining behaviour from  $\sim 10^9 M_{\odot} \text{ kpc}^{-2}$  at  $0.5 R_{\text{eff,SDSS}}$  to  $\sim 10^8 M_{\odot} \text{ kpc}^{-2}$  at  $2 R_{\text{eff,SDSS}}$ . This is in good agreement with the estimations yielded by the SED fitting on the Subaru-HSC imaging data presented in Chapter 5, whose median is indicated by the solid red line with corresponding  $1\sigma$  shaded regions. We see that the average profile as estimated by STARLIGHT is always within the scatter of the HSC profile, and the differences in the estimation vary between  $0.1$  and at most  $\sim 0.3$  dex, similar to or within the uncertainties of the estimations themselves by both photometric SED fitting or full spectral fitting ( $\sim 0.2$  dex uncertainties). The similar behaviour of the two average profiles and the differences between the SED fitted values and STARLIGHT estimates being within the uncertainties means that we are confident that our fitting of the full spectra to estimate the stellar population properties of our SAMI-HSC is robust. We present further checks in Appendix A.4.

Another parameter which can reveal much about a galaxy's state is the line-of-sight velocity dispersion, usually denoted as  $\sigma$  or  $\sigma_{\text{LOS}}$ . Large velocity dispersions can be due to either increased stellar mass/stellar mass densities or older stellar populations, or can be indicators of interactions. Hence, we plot  $\sigma$  as a function of radius in the same manner as the age, metallicity and stellar mass surface density. This shown in the right-hand panel of Figure 7.2.1. We observe a wide range of values in the individual profiles, which are repre-

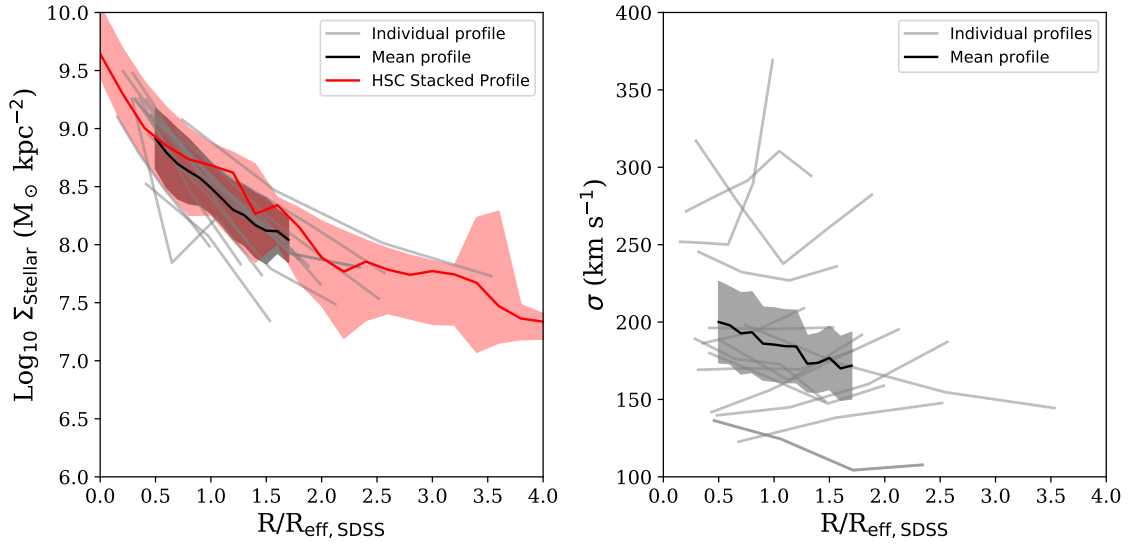


**Figure 7.2.1:** Left-hand panel: The stellar mass surface density profiles as estimated by STARLIGHT of individual SAMI-HSC galaxies (grey lines) and the interpolated average (black solid line with corresponding scatter shaded). The median profile as determined by SED fitting of HSC imaging data, from Section 5.2, is given by the solid red line with corresponding  $1\sigma$  scatter indicated by the shaded areas. Right-hand panel: The line-of-sight velocity dispersion profiles of individual galaxies (thin grey lines) and the interpolated average given by the solid black line with scatter given by the shaded grey area.

sented by the thin grey lines. We also observe a slight decrease in the  $\sigma$  interpolated average from 200 to 170  $\text{km s}^{-1}$ . This is likely due to the decreasing stellar mass surface density.

### 7.3 The Stellar Population Profiles of Interaction Sub-Samples

With the estimations of the age and metallicity profiles presented for the full SAMI-HSC sample and having shown that the stellar mass surface density profiles in agreement with alternative methods from Section 5.2, we now turn our attention to how the stellar population profiles depend on morphology. We split our sample of 15 galaxies according to our morphological classification scheme presented in Section 4.2. As a reminder, these galaxies are classified according to if they display tidal features indicative of ongoing interactions due to minor mergers (features, 6 galaxies represented by the blue lines), display no features but a diffuse stellar halo (diffuse, 7 galaxies represented by the green lines) or no features or stellar halo at all (featureless, 2 galaxies represented by the red lines). As these sub-samples are small, especially the featureless sub-sample, we refrain from drawing strong conclusions from the following comparisons. We instead describe the trends and interpret these as hints of possible general behaviour. Greater samples would be needed to confirm or rule out these postulations.

We plot the individual profiles (thin lines with corresponding colours) in stellar mass surface density, stellar line-of-sight velocity dispersion, light-weighted stellar age and light

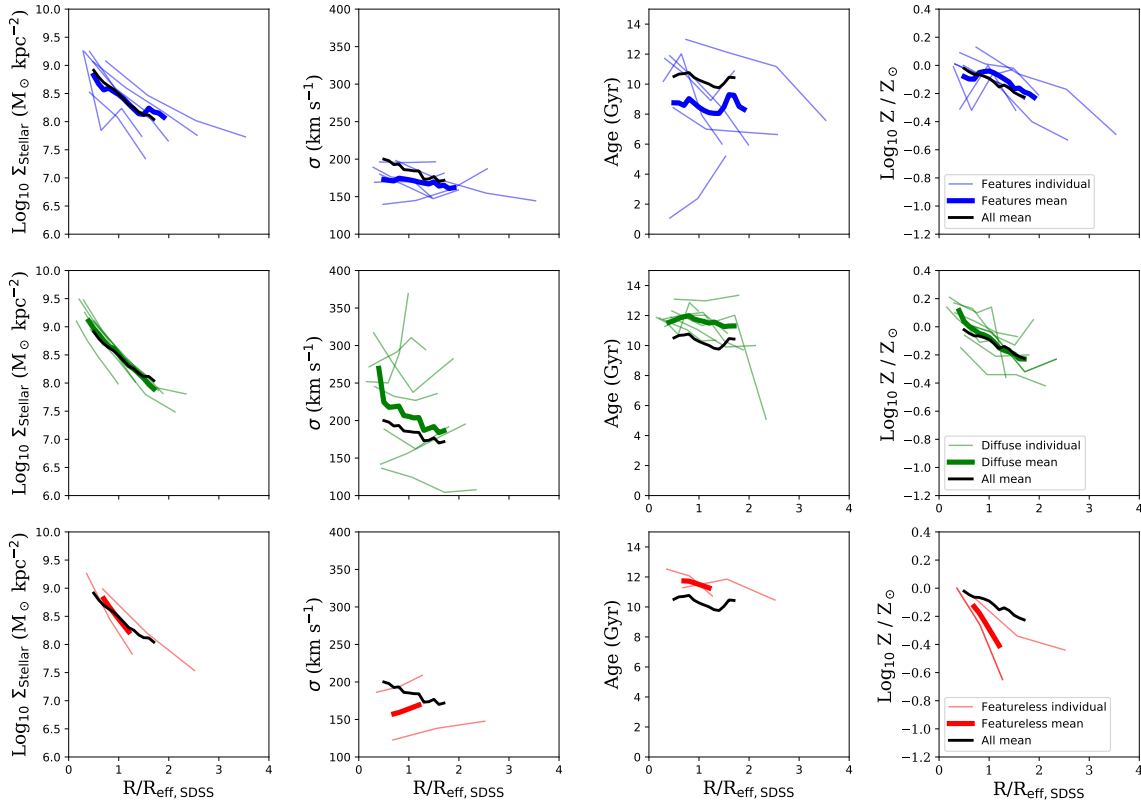


**Figure 7.3.1: Top to bottom:** The radial profiles of the sub-sample which display interaction features caused by minor mergers (features), the sub-sample which display no features but a diffuse stellar halo (diffuse) and the sub-sample which display neither features nor a diffuse stellar halo (featureless). **Left to right:** The stellar mass surface density profiles, the stellar line-of-sight velocity dispersion profiles, the light-weighted stellar age profiles and the light-weighted metallicity profiles. In each plot the individual profiles are indicated by the thin coloured lines, the interpolated average by the thick coloured lines and the average of the full SAMI-HSC sample by the thick, black line.

weighted metallicity as a function of effective radius in subsequent panels going from left to right in Figure 7.3.1. Inspecting the panels from top to bottom in Figure 7.3.1 shows each of the three sub-samples (features - blue, diffuse - green and featureless - red). In order to compare the behaviour of each sub-sample to the average trends presented above in Sections 7.1 and 7.2, we plot the interpolated average of the full SAMI-HSC sample in black. We also calculate an interpolated average for each sub-sample, represented by the thick line of corresponding colour, to contrast differences more easily. We also still apply the requirement that at least half of the galaxy sample (in this case each sub-sample) contributes to each interpolated average.

Initially considering the features sub-sample in the top row of Figure 7.3.1, we observe an average stellar mass surface density profile similar to that of the full SAMI-HSC sample. We note a significantly greater variety in the stellar mass surface density profiles despite

similar numbers compared to the diffuse sub-samples and a slight increase in the outskirts, however this is not significant enough to fully interpret. This may indicate that the minor merger activity may be actively perturbing the stellar mass surface density profiles of our sample. The velocity dispersion profiles are, on average, fairly flat and slightly below the average of the full SAMI-HSC sample, however these differences are minor ( $25 \text{ km s}^{-1}$ ) and only in the very central regions of the sub-sample. We see stellar age profiles which are, on average, slightly younger than the full SAMI-HSC sample by between 1 and 2 Gyr, flat and with a greater scatter than the diffuse sub-sample. The metallicity profiles are slightly metal-enriched compared to the average profile of the full sample, however these differences are less than 0.05 dex and not significant.

Considering the diffuse sub-sample of galaxies in the middle row of Figure 7.3.1, we observe stellar mass surface density profiles very similar to the average of the full SAMI-HSC sub-sample. We also see much less variation in the individual profiles compared to the features sub-sample, indicating that these objects are much more uniform. We see, however, a much greater variance in the stellar velocity dispersion profiles which are on average greater by  $25 \text{ km s}^{-1}$  than the average found for the full SAMI-HSC sample. The age profiles of the diffuse sub-sample are flat and above the average of the full SAMI-HSC sample by between 1 and 2 Gyr, while the average metallicity profile displays no significant difference from the average of the full SAMI-HSC sample.

We finally consider the featureless sub-sample, presented in the bottom row of Figure 7.3.1, although with caution as two galaxies are not enough to draw conclusions from. These two galaxies appear to closely follow the average trend of the full SAMI-HSC sample in stellar mass surface density. They appear to have increasing velocity dispersions with increasing radius, opposite to the full SAMI-HSC sample. They also appear to be older than average by between 1 and 2 Gyr at all radii, with a shallow decrease in light-weighted stellar age with increasing radius, and metal-poor, with both objects metal deficient at all radii compared to the average trend by between 0.1 and 0.5 dex.

In summary: The features sub-sample appears significantly younger than average, with a significantly greater scatter in light-weighted stellar age and stellar mass surface density than other sub-samples. The diffuse sub-sample seems to contain fairly uniform and average objects in metallicity and stellar mass surface density, however appear slightly older than the average for the entire sample. The featureless objects appear older and metal-poorer than average. These trends, however, may also be driven by differences in stellar mass between the different sub-populations due to trends in stellar mass and stellar population properties (Gallazzi et al. 2005, see e.g.). Hence, in the next section, we investigate if our results are intrinsic or driven by stellar mass differences.

## 7.4 Stellar Mass vs Intrinsic Differences in Stellar Populations

In order to investigate whether stellar mass is biasing any possible differences in the stellar population profiles we observe, we need to compare the estimations of age, metallicity and velocity dispersion as a function of stellar mass for each annulus. This is seen in Figure 7.4.1.

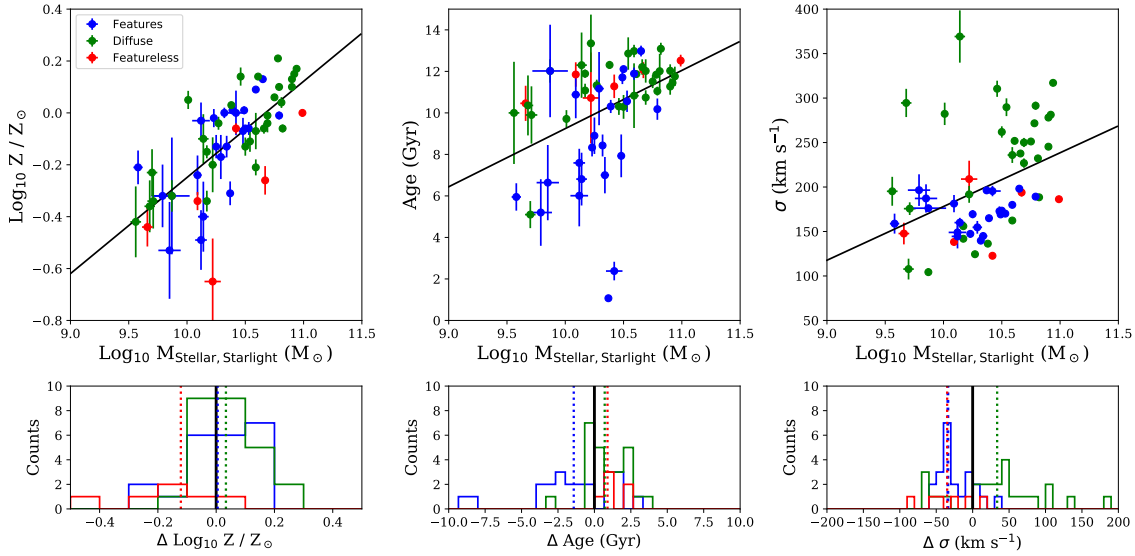


**Figure 7.4.1: Top panels left to right:** The stellar mass versus the metallicity, stellar age and stellar velocity dispersion estimations for each IFU annulus within each of the three interaction sub-samples (features - blue, diffuse - green and featureless - red). The black solid line gives the least squares best-fit for each trend for all galaxies. **Bottom panels left to right:** The differences between the best-fit and each annulus estimation represented by the corresponding histogram for each column (median for each sub-sample indicated by the dotted line).

The top left-hand panel shows the estimations of stellar mass versus stellar metallicity. We see a fairly tight correlation between mass and metallicity altogether (least squares fit given by the solid black line), with significant differences only found in the featureless sub-sample. We quantify these differences by calculating the difference between each estimation and the least squares best-fit estimation at the same stellar mass, and plot as a histogram in the bottom left panel. We see that the diffuse and features sub-samples show a median difference significantly smaller than 0.1 dex, hence are not different from each other.

We see in the bottom left histogram, however, that the median metallicity of the featureless sub-sample lies 0.13 dex below the average trend. This is slightly greater than the average uncertainties on the metallicity estimations, although the small sample size is susceptible to stochastic fluctuations. This is in agreement with the trends in the metallicity profiles presented above in Section 7.3, however we note that the average differences in the featureless sub-sample are smaller here (0.13 dex) compared to the 0.1 - 0.5 dex in the profiles. This greater difference in the featureless sub-sample metallicity profiles compared to the median, than the expected mass-matched metallicity deficiency means that although intrinsic differences are responsible, low stellar masses are also likely to be playing a role here.

The top mid panel of Figure 7.4.1 shows the estimations of stellar mass versus light-weighted stellar age with the corresponding differences indicated by the histograms in the bottom mid panel. We see that the medians of the featureless and diffuse sub-samples lie

0.9 and 0.7 Gyr above the average trend, however these are still within the uncertainties on the estimations. The median difference of the features sub-sample is located 1.4 Gyr below the average trend, hence although a difference is found, these are only hints, rather than significant results. These differences, however, are of similar values to the differences found in Section 7.3, showing that the main driver of the differences in the stellar age profiles are intrinsic rather than due to differences in the stellar masses of the sub-samples.

The top right-hand panel of Figure 7.4.1 shows stellar mass versus velocity dispersion, with the corresponding differences to the average trend found in the histogram in the bottom right-hand panel. We see differences in the medians of  $\sim 35 \text{ km s}^{-1}$  for the diffuse sub-sample and  $\sim -35 \text{ km s}^{-1}$  for the features and featureless sub-samples, once again reflecting the trends seen in Section 7.3.

We therefore conclude that although differences in the stellar mass of the different interaction sub-samples may drive small differences in the stellar populations, the differences found in the radial gradients in Section 7.3 are likely to be intrinsic (i.e. different interaction sub-samples are intrinsically different in their stellar populations). We caution once again, however, that the small nature of our samples and sub-sample mean these results should be interpreted carefully.

## 7.5 The In- and Ex-situ Fractions of SAMI-HSC Galaxies

Having established that our estimates of the properties of the stellar material in our SAMI-HSC galaxy sample are not systematically biased by stellar mass differences in each sub-sample but that any differences in stellar age and metallicity are intrinsic, we now investigate if these differences are imprinted on the fraction of in- to ex-situ stellar material. We take the estimated ex-situ fraction of stars for each annulus, as outlined in Section 6.3, and first investigate the trends found in all galaxies in order to establish the average trend of the full SAMI-HSC sample. As in previous sections of this chapter, we initially plot all separate profiles, followed by an interpolated mean to provide an idea of the average of the sample. This can be seen in Figure 7.5.1.

We first observe a general trend in the individual profiles, whereby the central regions of each galaxy are dominated by in-situ stellar material. The values of ex-situ stellar material within  $\sim 1 R_{\text{eff,SDSS}}$  range between 4 to 20 per cent, with most values below 10 per cent. This indicates that the central regions of these massive galaxies are, on average, extremely in-situ dominated. As we increase the radius of most galaxies, we see an increase in the ex-situ fraction of stellar material, with an increasing scatter, ranging from between 10 to 80 per cent at  $1.5 R_{\text{eff,SDSS}}$ , although all values but one are between 10 and 40 per cent.

These trends are reflected in the interpolated average, where at  $0.5 R_{\text{eff,SDSS}}$ , we observe an average ex-situ fraction of 4 per cent. This increases steadily to an ex-situ fraction of 18 per cent at  $1.5 R_{\text{eff,SDSS}}$ . The drop observed in the interpolated average after this point is driven by the lack of galaxies contributing to the average profile rather than the trends seen in the individual profile and hence should not be interpreted in these overall trends. We discuss this behaviour in more detail, including that these values are more likely to be lower

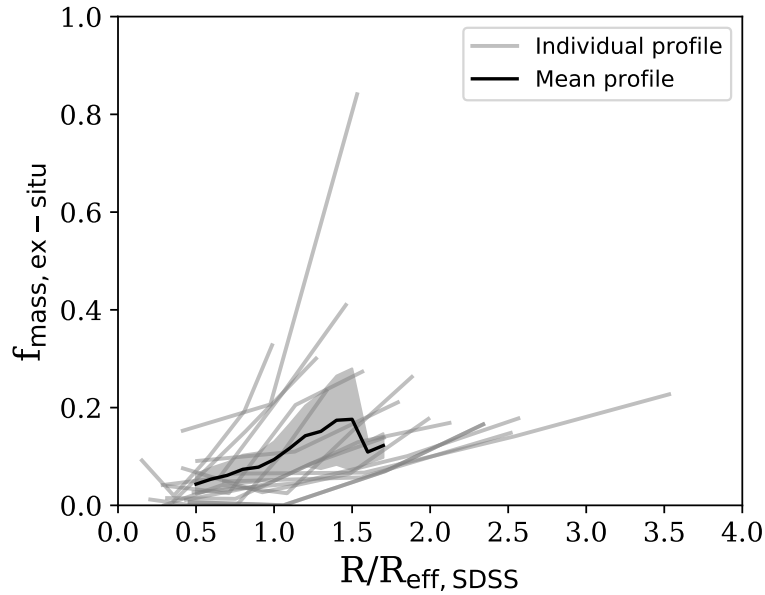


**Figure 7.5.1:** The fraction of ex-situ stars as a function of radius for our entire SAMI-HSC galaxy sample. The grey thin lines indicate each of the 15 individual profiles, the black thick line gives the interpolated median, which is calculated in the same way as previous sections in this chapter, with the associated error indicated by the grey shaded regions. We see an increase in the ex-situ fraction of stellar material with increasing material in nearly all cases.

limits on the fraction of ex-situ stellar material, in Section 8.3.

Having established the average trends for the entire SAMI-HSC sample, we then split by interaction class and plot the ex-situ fraction as a function of radius in the same way as for the stellar ages, metallicities etc. in Section 7.3. This can be seen in Figure 7.5.2, whereby from left to right we observe the ex-situ fraction of stars as a function of radius for the features sub-sample (blue), diffuse sub-sample (green) and featureless sub-sample (red). In the same manner as for Figure 7.3.1, we plot the individual profiles as thin lines in each respective colour, the interpolated median as the thick line in each respective colour, and the interpolated mean of the entire SAMI-HSC sample in black, in order to compare how the trends in each sub-sample compare to the general population.

We observe no significant difference in all sub-samples of the interpolated mean compared to the average of the population, with differences of  $\sim 2$  per cent between the average of each sub-sample and the average of the SAMI-HSC sample at most points (at maximum 5 per cent). This is within the uncertainties calculated for the average profile at most radii. We do notice, however, that the features sub-sample displays a higher variation in the individual profiles than the diffuse sub-sample, although once again this behaviour is weak. We discuss this further in Section 8.3.

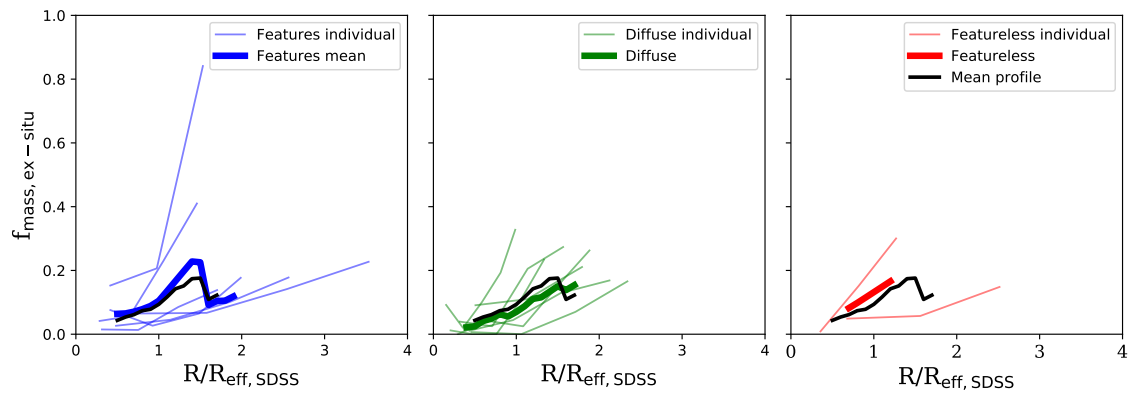


**Figure 7.5.2:** The fraction of ex-situ stars as a function of radius for each of the three interaction classes in our SAMI-HSC galaxy sample (features - blue in the left-hand panel, diffuse - green in the middle panel, and featureless - red in the right-hand panel). The respectively coloured thin lines in each panel indicate the individual profiles of the galaxies contained in each sub-sample, the interpolated mean for each sub-sample is represented by the respective thick, coloured line and the black line gives the interpolated median of the entire SAMI-HSC sample. We see a range of behaviours in the individual profiles of each sub-sample, however no significant difference in the interpolated average between each sub-sample. We do see, however, a possible hint of a larger scatter in the individual profiles of the features sub-sample.

*"Although we, as people, move around, go on adventures and explore the world around us, a lot of us, especially those of us who have grown up on and been a part of the land, are just as hefted as the sheep on the land and fells around us."*

Jeremy Jackson (my father) - 2020

# 8

## Discussion

In this research, we (my collaborators and myself) have investigated for the first time from beginning to end, the stellar mass assembly and growth processes of low redshift, massive, central galaxies.

We initially investigated the stellar mass assembly of a sample of such galaxies and linked their average assembly histories and characteristic present-day properties to the environmental and secular processes that have influenced these characteristics. We found secular effects to be the main driver of the stellar mass assembly of galaxies, with environmental processes playing a subtle role. We found slight tensions when comparing observations to the simulations, which we postulated was due to over-aggressive AGN feedback. We also found a sub-population of galaxies which displayed behaviour not expected from a downsizing scenario, with younger lookback times than galaxies with lower stellar masses. The subtle role of the environment and the possible reasons for the behaviour of the aforementioned sub-sample will be the subject of Section 8.1.

We then investigated the possible size growth processes of a sub-sample of these galaxies. We attempted to find signs of minor mergers of galaxies, which is the expected driver of the size growth of massive galaxies, with deep multi-band optical imaging contained in the Subaru HSC survey. We visually classified these objects according to their LSB features, finding widespread interaction activity at similar levels to previous studies. We created a method to specifically detect the galaxy and these surrounding features and ran SED fitting to estimate the colours and stellar mass densities of the material. We found a flattening of the stellar mass surface density profiles due to this specifically detected material (and how methods used in previous studies may wash out the signatures of this material). In Section 8.2, we will discuss these results and provide the direct link of this material to the surrounding satellite population and the implications of this result for the size growth via minor merger

scenario.

Finally, we investigated the imprints of these processes on the stellar populations of a further sub-sample of these galaxies with data coverage in the SAMI IFU galaxy survey in Chapter 7, which we referred to as our SAMI-HSC sample. We used full spectral fitting codes in conjunction with the MILES empirical stellar library in order to estimate properties of the stellar populations. We found gradients in stellar age and metallicity in approximate agreement with previous studies, stellar mass surface densities in agreement with the estimates yielded by photometric SED fitting in previous sections of this work, and an increase in the ex-situ fraction with increasing radius. We also found hints of differences in some gradients of age and metallicity when split by interaction class, and that these differences are intrinsic to the galaxy rather than driven by differences in the stellar masses of the sub-samples. In Section 8.3 we will shortly discuss the pitfalls associated with the estimations of the ex-situ stellar fraction. We will also discuss the drivers of the differences we see. We will then discuss the significance of the differences in the various interaction classes and how this ties into the work carried out using the HSC imaging data in Chapter 5 and possible sources of the intrinsic differences.

I also include an outline of possible future directions for this research and the techniques contained within it in Section 8.4.

Parts of this Chapter are contained in the studies of [Jackson et al. \(2020b\)](#), [Jackson et al. \(2021\)](#) and Jackson et al. (in prep). Contributions by collaborators to this Chapter are as follows: Dr. Anna Pasquali, Dr. Francesco La Barbera, Mr Christoph Engler, Dr. Annalisa Pillepich, Ms Alina Böcker, Dr. Surhud More, Dr. Rory Smith and Prof. Eva Grebel for the discussion of tests, plots and tables throughout and the discussion of results and interpretations.

## 8.1 Discussion I - Interpreting the Stellar Mass Assembly of Central Galaxies

### 8.1.1 Trends in the Formation Times: Stellar Mass vs Halo Mass

While investigating the stellar mass assembly of low redshift, massive, central galaxies, we have seen that a number of interlinked galaxy properties display the same average trends as a function of stellar and halo mass, such as the Sérsic index, sSFR, lookback times and growth rates. Figures 2.1.1, 3.1.1, and 3.4.1 show that all of these galaxy properties have a strong dependency on stellar mass, consistent with previous studies which claim that stellar mass is the dominant driver in galaxy assembly and evolution. This can be seen in Figure 3.2.1, where the stellar mass assembly lookback times display steeper trends with stellar mass than with halo mass. We see that, in general, more massive galaxies (at constant halo mass) assembled certain percentages of their stellar mass earlier. This result follows previous studies which find downsizing, whereby more massive objects assemble specific percentages of their stellar mass at earlier cosmic times than less massive objects ([Cowie et al. 1996](#); [Thomas et al. 2005](#); [Pacifci et al. 2016](#)).

We also see, however, that there are secondary dependencies on halo mass, albeit subtler than the trends in stellar mass. If we hold stellar mass constant (in the regime that  $M_{\text{Stellar}} < 10^{11} M_{\odot}$ ), those galaxies which reside in more massive haloes tend to have younger lookback times which are reflected in their higher growth rates, higher sSFRs and lower Sérsic indices. One scenario could be that the more massive halo has a larger gravitational potential and is able to cool hot accreted gas more efficiently for steady star formation, presented as the "hot-mode" accretion in [Katz et al. \(2003\)](#) and [Kereš et al. \(2005\)](#), or recycle earlier accreted hot gas easier (e.g. [O'Donnell et al. 2020](#)). A second scenario could be that higher mass haloes contain more satellites, which could supply gas to their centrals via interactions and mergers in order to sustain their star formation (e.g. [De Lucia & Blaizot 2007](#); [Jackson et al. 2020a](#)). These scenarios are likely to become clearer in further studies over the coming years utilising multi-wavelength data to investigate the nature of gas accretion across multiple environments.

### 8.1.2 High Stellar-to-Halo Mass Objects: The Exception to Downsizing

The exception to the observed downsizing and environmentally driven behaviours is a sub-population of objects ( $M_{\text{Stellar}} \sim 10^{11} M_{\odot}$  and  $M_{\text{Halo}} \sim 10^{12} M_{\odot}$ ) with high stellar-to-halo mass ratios, which constitute  $\sim 2$  per cent of our entire sample and drive the non-monotonic trends seen in the lookback times when comparing different halo masses as a function of stellar mass (Figure 3.2.1). We postulate that these objects are massive spirals in the field with a relatively quiet accretion history. The characteristic low Sérsic indices indicate late-type morphologies, while the higher sSFRs show that star formation is not yet quenched in these systems, a phenomenon that is fairly rare in galaxies with stellar masses of  $10^{11} M_{\odot}$ . According to the group catalogues, they are also located on average in haloes with no companions, supporting the idea that they may not have been morphologically transformed due to a lack of interactions, at least in recent times. To test this hypothesis, we also visually inspected 50 of these objects selected at random using SDSS imaging data, finding no significant signs of interactions, very few neighbours and mostly disk-like structure in the majority of these objects.

When we observe their growth from epoch to epoch in Figure 3.4.1, we see that they have a fairly constant and steady growth history. They do not grow as quickly at early epochs and as slowly at later epochs as the most massive galaxies, however not as quickly as the least massive galaxies at low redshift. They instead display an intermediate relative value at almost all epochs. We postulate that this steady growth is most likely driven by one of two scenarios. The first is steady gas accretion from the surrounding environment either via filaments or minor mergers, similar to the "cold mode" presented in [Kereš et al. \(2005\)](#). The second is the cooling of recycled internal gas which has already been accreted at much earlier times such as postulated in [O'Donnell et al. \(2020\)](#). Such galaxies have been studied, albeit in individual cases or small samples in [Ogle et al. \(2016\)](#) and [Ogle et al. \(2019\)](#), where they also propose that these objects could be sustained by the cooling and recycling of already accreted gas.

We postulate that this rare population is likely to exist in TNG, albeit at much lower

numbers. From Figure 3.2.1, by tracking our lowest stellar mass population as a function of halo mass (blue lines, mid left-hand panel), we see that this sub-population is not as prominent in TNG300. This is likely due to volume driven effects (the smaller the volume of the sample, the less likely we are to find peculiar objects statistically) as these galaxies are extreme and only make up 2 per cent of our observational sample.

### 8.1.3 Connecting the Oldest Galaxies and High Redshift, Compact Objects

We now turn our attention to the most massive and oldest objects in our sample. Taking values from Figure 3.2.1, we see that the most massive galaxies have a median  $t_{90}$  value of 6 Gyr, with some  $t_{90}$  values reaching 8 Gyr. This shows that these galaxies have passively evolved since between  $z = 0.7 - 1.1$ . When we quantify the  $t_{50}$  values of these objects, which is a proxy for the stellar ages, we find values of 8 - 11 Gyr. This corresponds to redshifts of 1.1 - 3. The  $t_{90}$  values are slightly below the original study of Daddi et al. (2005), whose passive galaxies were located at  $z = 1.4 - 2.5$ , however we stress that different samples and techniques prevent a fully quantitative comparison.

Daddi et al. (2005) also estimate average stellar ages of 0.5 - 1.5 Gyr for their sample, placing the average stellar age of their sample at a redshift between  $z = 2 - 4$ , somewhat in line with our own  $t_{50}$  values. This shows that the most massive galaxies in our sample were likely quiescent at these higher redshift epochs ( $z > 1$ ) and are most likely similar to the massive, compact objects found in the study of Daddi et al. (2005). This poses the likely scenario that these objects were also compact at these redshifts.

## 8.2 Discussion II - Interpreting LSB Material around Central Galaxies

With the connection of the stellar mass assembly history of low redshift, massive, central galaxies and the high redshift compact objects drawn, we now need attempt to put the results from Section 5 into context of the two-phase growth scenario.

### 8.2.1 Comparison of the Colour Profiles to SDSS Satellites

In Section 5.2, we showed that tidal features due to accreted material can be quantified in colour and stellar mass surface density. These tidal features are reflected as a flattening in the outskirts of stellar mass surface density profiles ( $\gtrsim 3 R_{\text{eff,SDSS}}$ ) when trying to specifically detect and quantify these features. We see from Sections 5.3 and 5.4 that PSF effects, although shifting some of the stellar mass surface density from the centres of the radial profiles to the outskirts, cannot account for the levels of stellar mass surface density at radii of  $\gtrsim 3 R_{\text{eff,SDSS}}$ . We have also seen that the stellar mass surface densities are driven predominantly by galaxies that show features, hence signs of merger activity, with some minor contributions by galaxies which display a diffuse stellar halo.

In order to link this LSB material we have detected and quantified in the outskirts of these central galaxies to the minor merger driven growth scenario of massive galaxies, we

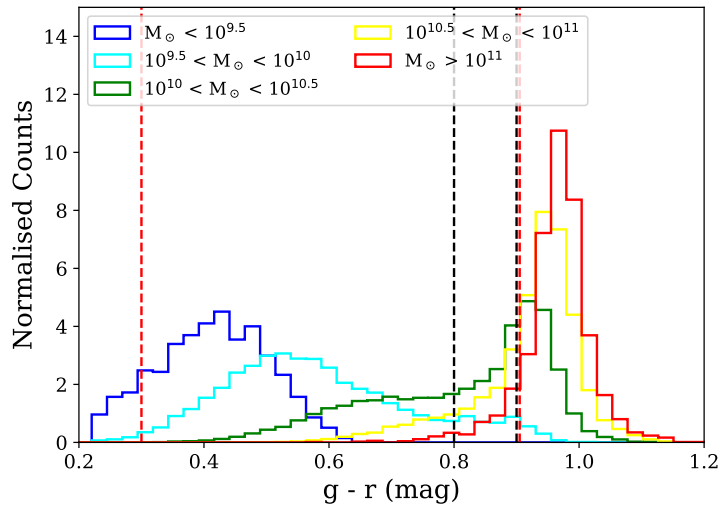


**Figure 8.2.1:** The distribution in  $g-r$  colour of satellites taken from SDSS catalogues in bins of 0.5 dex in stellar mass. The dashed black and red lines mark the approximate colour limits of the bulk of stellar material in the centre ( $< 2 R_{\text{eff,SDSS}}$ ) and outskirts ( $> 2 R_{\text{eff,SDSS}}$ ) of our passive galaxy radial profiles respectively.

directly compare the colours of various populations of satellite galaxies. To do this, we take the SDSS catalogues of [Lim et al. \(2017\)](#) and select only satellite galaxies, defined as those galaxies in a halo that are not designated as the central galaxy of that halo, across the same redshift range as our passive galaxy sample ( $0.05 < z < 0.1$ ). We then calculate the  $g-r$  colour of each satellite from the SDSS photometry and bin in intervals of 0.5 dex in stellar mass. The distributions can be seen in [Figure 8.2.1](#). We see the well-known trend whereby more massive galaxies tend to be on average redder in their  $g-r$  colour.

The median  $g-r$  colour profile in the inner parts of our passive galaxy sample decreases from 0.9 to 0.8 mag between 0 and  $6 R_{\text{eff,SDSS}}$  (indicated by the black dashed lines in [Figure 8.2.1](#)), with an average scatter of  $\sim 0.1$  mag. As we increase the radius beyond  $6 R_{\text{eff,SDSS}}$ , we observe a range of median  $g-r$  colours, from  $\sim 0.4$  to 0.8 mag, with increased scatter in the  $g-r$  colour range  $\sim 0.5$  mag. The approximate boundaries of the profiles in these regions ( $> 6 R_{\text{eff,SDSS}}$ ) are indicated by the red dashed line in [Figure 8.2.1](#). The comparison sample displays similar behaviour in the nature of the stellar material inside of  $6 R_{\text{eff,SDSS}}$ , with median  $g-r$  colours ranging between 0.9 and 0.7 mag, however with greater scatter ( $\sim 0.3$  mag). The profiles in the outer regions exhibit a greater range of  $g-r$  colours between 0.2 and 1.2 mag, probably because of stochasticity due to the small sample and of the merger activity.

When we compare to the distribution of SDSS satellites in [Figure 8.2.1](#), we see that those satellite galaxies ranging in stellar mass  $M_{\text{Stellar}} < 10^{10.5} M_{\odot}$  have the most similar colours to the LSB material. Some of the redder material may be linked to higher mass satellites, however this is not the majority of the material beyond  $6 R_{\text{eff,SDSS}}$ . If we account for a possible

contribution from redder, in-situ stars with similar colours to the profiles within  $6 R_{\text{eff,SDSS}}$ , we would expect the accreted material to have even bluer average colours. This would shift potential accreted satellite galaxies to even bluer colours and, on average, smaller stellar masses.

### 8.2.2 Interpretation of the Merger Activity and Radial Profile Excesses

We showed in the previous section that the material in the outskirts of our galaxy samples has similar  $g - r$  colours to satellite galaxies ranging in stellar mass  $M_{\text{Stellar}} < 10^{10.5} M_{\odot}$ . We now take this a step further by inspecting the plausibility of the minor merger scenario to deliver the amount of stellar material. We conduct this by quantifying the total stellar mass of this material in both our passive and comparison galaxy samples. A large percentage of the stellar mass contained in the outskirts may indicate different origins of this material.

We first isolate the features and diffuse sub-samples of galaxies in both the passive and comparison galaxy samples. We then calculate the average stellar mass per galaxy contained in a bin of  $1 R/R_{\text{eff,SDSS}}$  from the estimates of stellar mass yielded by the SED fitting process. We then work out the percentage stellar mass that each bin in  $1 R/R_{\text{eff,SDSS}}$  contributes to the total stellar mass contained on average in one galaxy. The integrated or total stellar masses can be seen in Table 8.2.1 for the passive galaxy sample and Table 8.2.2 for the comparison galaxy sample.

We first see that for both our passive and comparison galaxy samples, those galaxies that display features show a larger stellar mass contribution in their outskirts. The integrated stellar mass in these regions, however, is relatively small. In the passive galaxy sample this totals a stellar mass outside of  $2 R_{\text{eff,SDSS}}$  of  $10^{10.4} M_{\odot}$  (equating to  $\sim 9$  per cent) for those galaxies which display features and  $10^{10.3} M_{\odot}$  (equating to  $\sim 8$  per cent) for our diffuse sub-sample. In the comparison sample, the stellar mass contained outside of  $2 R_{\text{eff,SDSS}}$  is  $10^{10.1} M_{\odot}$  both for galaxies that exhibit features and for those that have a diffuse halo (or  $\sim 6$  and  $5$  per cent respectively).

Taking the median integrated stellar mass estimates at all radii (denoted as "Total") from both Table 8.2.1 and 8.2.2 of  $\sim 10^{11.3-11.4} M_{\odot}$  and convolving them with the standard definition of a minor merger as  $1:4 < \mu < 1:100$  (as in Hirschmann et al. 2015), we get an average stellar mass of the accreted satellites of  $\sim 10^{9.3-10.8} M_{\odot}$ . Comparing this figure to the integrated stellar mass in the outskirts (outside of  $2 R_{\text{eff,SDSS}}$ ) of  $10^{10.2-10.4} M_{\odot}$ , we see that minor mergers are capable of delivering the amount of stellar mass required to explain the stellar material found in the outskirts.

The amount of mass required to be accreted is, however, also likely to be smaller than this estimate, as not all stars at these radii are ex-situ. Davison et al. (2020) find that some in-situ stars exist at these radii using simulations, whereby the ex-situ fraction of stars in galaxies of stellar mass  $10^{10} M_{\odot} - 10^{11} M_{\odot}$  is  $\sim 25$  per cent at  $2 R_{\text{eff,SDSS}}$ , and up to 40 per cent at  $4 R_{\text{eff,SDSS}}$ . This is increased to 65 and 70 per cent, respectively, for galaxies of stellar masses of  $10^{11} M_{\odot} - 10^{12} M_{\odot}$ . This significantly lowers the required mass to be delivered by the satellite galaxies by 30 - 60 per cent.

**Table 8.2.1:** The total stellar mass in bins of  $1 R/R_{\text{eff,SDSS}}$  of the HSC passive galaxy sample

Radius ( $R_{\text{eff,SDSS}}$ )	Passive (features)		Passive (diffuse)	
	$\text{Log}_{10} M (M_{\odot})$	per cent	$\text{Log}_{10} M (M_{\odot})$	per cent
Total	11.41	-	11.42	-
$< 1 R_{\text{eff,SDSS}}$	11.30	77.71%	11.33	80.65%
1 - 2 $R_{\text{eff,SDSS}}$	10.52	12.75%	10.49	11.68%
2 - 3 $R_{\text{eff,SDSS}}$	10.18	5.88%	10.11	4.96%
3 - 4 $R_{\text{eff,SDSS}}$	9.72	2.08%	9.69	1.85%
4 - 5 $R_{\text{eff,SDSS}}$	9.30	0.77%	9.12	0.51%
5 - 6 $R_{\text{eff,SDSS}}$	9.04	0.42%	8.84	0.27%
6 - 7 $R_{\text{eff,SDSS}}$	8.55	0.14%	8.26	0.08%
7 - 8 $R_{\text{eff,SDSS}}$	8.49	0.12%	-	-
$> 8 R_{\text{eff,SDSS}}$	8.53	0.13%	-	-

**Table 8.2.2:** The total stellar mass in bins of  $1 R/R_{\text{eff,SDSS}}$  of the HSC comparison galaxy sample

Radius ( $R_{\text{eff,SDSS}}$ )	Comparison (features)		Comparison (diffuse)	
	$\text{Log}_{10} M (M_{\odot})$	per cent	$\text{Log}_{10} M (M_{\odot})$	per cent
Total	11.31	-	11.38	-
$< 1 R_{\text{eff,SDSS}}$	11.22	79.95%	11.29	81.88%
1 - 2 $R_{\text{eff,SDSS}}$	10.45	13.62%	10.49	12.87%
2 - 3 $R_{\text{eff,SDSS}}$	9.98	4.58%	9.85	2.96%
3 - 4 $R_{\text{eff,SDSS}}$	9.34	1.07%	9.42	1.10%
4 - 5 $R_{\text{eff,SDSS}}$	8.91	0.40%	9.34	0.90%
5 - 6 $R_{\text{eff,SDSS}}$	8.66	0.22%	8.58	0.16%
6 - 7 $R_{\text{eff,SDSS}}$	8.26	0.09%	8.51	0.13%
7 - 8 $R_{\text{eff,SDSS}}$	7.85	0.03%	-	-
$> 8 R_{\text{eff,SDSS}}$	7.91	0.04%	-	-

Another factor to account for in this type of comparison is the survival time of various merger features. A recent study by [Mancillas et al. \(2019\)](#) used  $N$ -body simulations to compare the formation of merger features or tidal activity to observational data and calculated the average survival time for these types of features. They estimated a survival time of  $\sim 2$  Gyr for tidal tails,  $\sim 3$  Gyr for streams and  $\sim 4$  Gyr for shells. They do not, however, state how this relates to the surface brightness that these features are detectable at. As the study uses surface brightness limits of 29 and 33 mag arcsec $^{-2}$ , we assume that these times will be longer than what we would expect with our imaging, which only goes down to  $\mu_{r\text{-band}} \sim 28$  mag arcsec $^{-2}$ . As our passive galaxies are selected to have assembled 90 per cent of their stellar mass over 6 Gyr ago, this means that the features are extremely unlikely to be due to major mergers, as a major merger with a stellar mass ratio of at least 1 to 4 would deliver more than 10 per cent of the stellar mass observed today. Any activity therefore can not be older than this time, agreeing with the hypothesis that these tidal features caused by minor mergers.

To summarise: The average stellar mass per galaxy contained in the outskirts of our sample, mainly in the form of tidal and merger features is of the order of  $10^{10.2-10.4} M_{\odot}$ . The ex-situ mass contained here is likely to be lower as not all stars at these radii ( $> 2 R_{\text{eff,SDSS}}$ ) are ex-situ (simulations predict anywhere between 25 to 80 per cent [Davison et al. 2020](#); [Remus & Forbes 2021](#)). The colour of this material is similar to the average SDSS satellite population with stellar masses  $M_{\text{Stellar}} < 10^{10.5} M_{\odot}$ . This leads to the plausible scenario that this material was accreted from the surrounding satellite population. These results, combined with the widespread merger activity we see ( $\sim 40$  per cent in both samples) quantitatively strengthen the scenario in which minor mergers drive the size growth of central galaxies observed in previous studies (e.g. [van Dokkum et al. 2010](#); [van der Wel et al. 2014](#)).

### 8.2.3 Comparison to HSC studies and Difference in Activity Levels

We can also compare some of our results to those found in previous studies of massive galaxies in HSC. [Huang et al. \(2018b\)](#) investigated the stellar mass surface density profiles of massive ( $M > 10^{11.4} M_{\odot}$ ) galaxies by fitting concentric ring models to HSC imaging data and performing SED fitting. Their profiles are fairly smooth compared to our own, in line with the expectations outlined in Section 5.3. They find stellar mass excesses of up to 0.1 - 0.2 dex (corresponding to masses of up to  $10^{11} M_{\odot}$  or roughly 10 per cent, however in more massive galaxies than in our sample) due to low surface brightness material in the outskirts of galaxies due to low surface brightness material when comparing their profiles to cModel photometry. Their profiles for individual galaxies can extend up to 100 kpc, much further than our sample, however we stress that this is probably due to our  $S/N$  cut of 3 per pixel and our lower mass galaxy sample.

We finally postulate that although the levels of merger activity are fairly constant across our two samples, as our passive galaxy sample is older than our comparison sample, these galaxies have had more time to allow features to settle into a state of equilibrium and hence form a diffuse stellar halo, accounting for the difference in the percentage of diffuse to featureless galaxies classified in the passive galaxy and comparison samples.

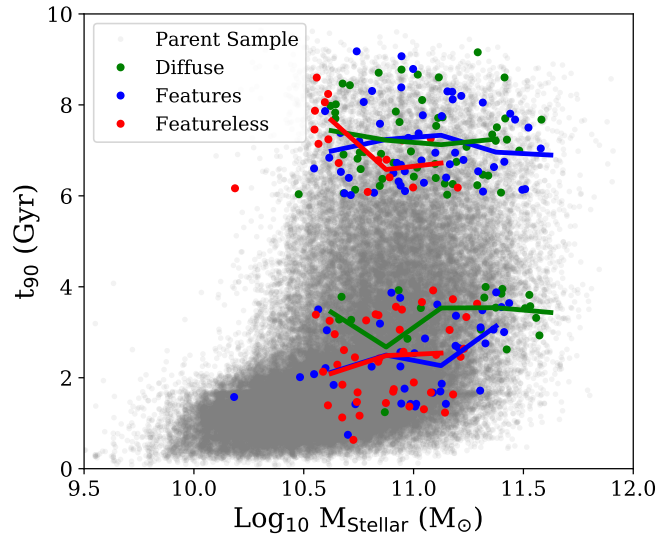


**Figure 8.2.2:** The lookback times at which a galaxy formed 90 per cent of its stellar mass ( $t_{90}$ ) as a function of stellar mass for each of the three interaction classes (features - blue, diffuse - green and featureless - red) in both the passive and comparison sub-samples. Average values of  $t_{90}$  as a function of stellar mass for each sub-sample are given by the respective coloured lines. We see that in general the features sub-sample covers the whole range of  $t_{90}$

Indeed this can be seen in Figure 8.2.2, where we plot the stellar mass versus lookback time at which each galaxy formed 90 per cent of its stellar mass for each sub-sample (features - blue, diffuse - green and featureless - red) in both the comparison and passive galaxy samples. We also bin in 0.25 dex bins in stellar mass and calculate the mean lookback time, represented by the corresponding coloured lines. We see that the features sub-sample covers the largest range of lookback times and stellar masses, indicated by the averages which are in the mid-ranges of each parent sample. We also see a preference for featureless galaxies to be located in the mid-range of the younger comparison sample, however those that are contained in the older passive sample, display younger ages (1 Gyr younger than the features or diffuse sub-samples). Conversely, in the younger comparison sample, we observe that the diffuse galaxies are on average 1 - 1.5 Gyr older than the features and featureless sub-samples.

We connect these older times to the state of equilibrium postulated earlier in this Chapter. Hence, we get a three-stage scenario: The first stage is where galaxies assemble the bulk of their stellar mass but have undergone relatively fewer minor mergers, hence are younger and featureless (although still larger than higher redshift galaxies). In stage two galaxies then undergo continually more minor mergers, revealed by the increasing amount of detectable interaction features, which builds up the outskirts of their stellar material and growing in size. This is followed in stage three by the material settling into equilibrium as the galaxy gets older, settling into our diffuse category. This scenario then provides a growth in size via minor mergers.

### 8.3 Discussion III - Interpreting the Stellar Populations of Central Galaxies

So far in this discussion, we have collected our results from Chapters 3 and 5 and presented arguments for the minor merger scenario driving the growth of massive galaxies in the Universe. We also saw hints of the imprints that these processes may leave on the stellar populations of their host galaxies in Chapter 7. There are, however, some points that need to be taken into consideration before we may draw conclusions about different interaction classes displaying different behaviour in their stellar population gradients.

#### 8.3.1 Upper Limits on the Fractions of Ex-Situ Material

One of the major problems in the determination of the ex-situ fraction of stars using the method presented in [Boecker et al. \(2020\)](#) is the use of smoothing in the regularisation. In short, the usual method of fitting the best combination of model stellar populations in pPXF (or indeed most fitting codes) usually leads to just a few of the models with certain ages and metallicities being combined. In reality, star formation histories are much more continuous. As mentioned in Section 6.3, to provide a more realistic estimation of the star formation history and stellar population, pPXF has a built in method to apply a smoothing technique between neighbouring models in age and metallicity space (or regularisation). However, smoothing too heavily can systematically bias the fitting process. Although this effect is minimal in the majority of the spectra used in this work, it can be more significant in spectra with lower signal-to-noise, the case for some spectra in the outskirts of our galaxies.

Biasing the model weightings towards older stellar ages and higher metallicities has the effect of underestimating the ex-situ fraction of stars. This is because when the empirical models of satellites are applied, the weights under each successive curve of constant satellite stellar mass are lower. Consequently, when the area underneath each curve of constant stellar mass for each satellite is integrated to work out the ex-situ fraction of stellar material delivered by satellites of that stellar mass, the result is biased towards lower values. A fully consistent treatment of the fitting process, however, is beyond the scope of this thesis. For this reason, the results presented in Section 7.5 should be treated purely as a lower limit on the ex-situ fraction of stellar material, especially at the highest radii.

Although the fitting process needs refining, we still include a qualitative comparison here to studies using simulations to determine the ex-situ fraction of stars to give an approximate idea of the values and trends (we note that this field is just emerging now and should be treated with a great deal of caution). For this purpose we use the studies of [Davison et al. \(2020\)](#) and [Remus & Forbes \(2021\)](#), noting that different sample selections, mass ranges and measurement techniques mean that a fully quantitative comparison is rendered useless. As both studies use simulations, the definition of  $R_{1/2}$  or  $R_{0.5}$  is used, denoting the radius within which half of the stellar mass is encapsulated, compared to our definition of  $R_{\text{eff,SDSS}}$ , of the half-light radius. The approximate comparison is given below in Table 8.3.1 to give a rough idea of different behaviours and values.

**Table 8.3.1:** The percentage of ex-situ stellar mass at various radii from this work and the two simulational studies of Davison et al. (2020) and Remus & Forbes (2021).

Study	0.5 $R_{\text{eff,SDSS}/0.5}$	1 $R_{\text{eff,SDSS}/0.5}$	1.5 $R_{\text{eff,SDSS}/0.5}$
This work (all galaxies)	4%	9%	18%
Remus & Forbes (2021)	40%	80%	90%
Davison et al. (2020) $10^{10} < M_* < 10^{11}$	19%	21%	25%
Davison et al. (2020) $10^{10} < M_* < 10^{11}$	65%	66%	67%

We see that our estimated values of the ex-situ fraction of stellar material are significantly below all estimates from the simulations, although for the lower mass sample from Davison et al. (2020), this difference is much smaller. We also note the wide difference in the estimated fractions, whereby even the highest mass galaxy sub-sample of Davison et al. (2020) is between 25 and 15 per cent different to the estimates of Remus & Forbes (2021). We also see very steady increases of the ex-situ fraction in Davison et al. (2020), of at most a few per cent, compared to the very rapid increase in the fraction of ex-situ stellar material seen in Remus & Forbes (2021). In summary: We estimate lower fractions of ex-situ stellar material as a function of radius (4 - 20 per cent) than the simulations (20 - 90 per cent), however with steeper or shallower increases compared to different studies. We also conclude that because this field of research is extremely new, more detailed studies with closer matching needs to be carried out in the future.

### 8.3.2 The Driver of Intrinsic Differences in Stellar Populations

In Section 7.4, we showed that the differences seen in the gradients of age and metallicity in Figure 7.3.1 were not driven by differences in the stellar mass distribution of each sub-sample, but are intrinsic. This means that the differences in our three sub-samples are driven by one of two options: different interaction morphologies or different assembly histories.

In order to better constrain possible drivers of the age and metallicity differences, we take a closer look at the assembly histories of these galaxies. We therefore plot the  $t_{90}$  values of our SAMI-HSC sample versus stellar mass, similar to Figure 8.2.2. This is shown in Figure 8.3.1.

Similar to Figure 8.2.2, we see the parent sample of SDSS catalogue galaxies in grey, and the interaction classes in their respective colours (features - blue, diffuse - green and featureless - red). We see that all of the diffuse galaxies are contained in the passive galaxy sample ( $t_{90} > 6$  Gyr), and on average older than the features and featureless galaxy samples. Similarly, we see that the features sub-sample spans a greater range of  $t_{90}$  values than the other sub-samples.

This has implications for our results and postulations presented in Chapter 7. Although we find some differences in the age gradients, and that these are not biased by the stellar mass, we may still be biased by our sample selection. We calculate a mean  $t_{90}$  value of the diffuse sample of 7.8 Gyr, compared to 4.9 Gyr for the features sample and 5.3 Gyr for the featureless sample. This difference of 3 Gyr in the  $t_{90}$  values between the diffuse and features sub-sample is similar to the differences in the age gradients in Section 7.3.

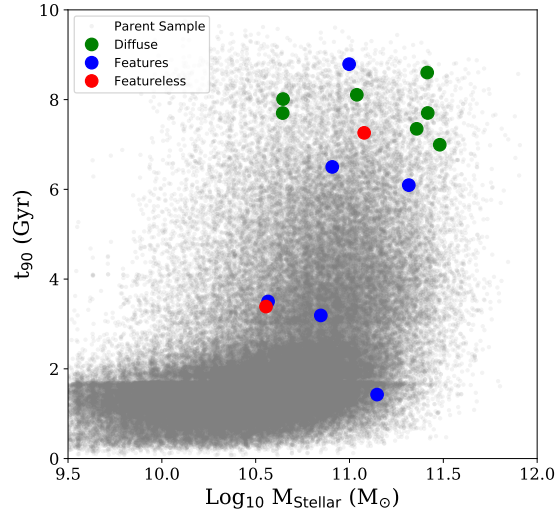


**Figure 8.3.1:** The lookback times at which a galaxy formed 90 per cent of its stellar mass ( $t_{90}$ ) as a function of stellar mass for each of the three interaction classes (features - blue, diffuse - green and featureless - red) in our SAMI-HSC sample.

This difference in the  $t_{90}$  values, therefore, likely explains the differences in the age gradients of our three sub-samples. Hence two galaxies of the same stellar mass and  $t_{90}$  value, but different interaction morphologies, have the same stellar population properties. The differences we see in stellar population gradients are therefore likely to be driven by the assembly histories, rather than the morphological classification.

A similar level of caution to Chapter 7 needs to be taken in interpreting these results, as the sample sizes are extremely small. We therefore state once again that this is a pioneering analysis, and will be better served with future surveys and data releases where bigger sample sizes will be available to employ such techniques on, some of which are outlined in the next section.

## 8.4 Discussion IV - Future Outlooks for Central Galaxies

Having established the stellar mass assembly and size growth processes of low redshift, massive galaxies and the possible consequences that these processes have on stellar population gradients, we highlight the potential future directions of this research. Some of these stages are already being planned and highlighted initially here as the data is currently available. Others that we mention later, however, are speculative, and based on obtaining observing time with the appropriate instruments at cutting-edge facilities currently available or future telescopes currently under construction.

Initially the focus of future studies should be to repeat and refine the processes developed in this thesis and outlined in Chapter 4 using the impending Data Release 3 (DR3) from the Subaru-HSC survey. DR3 is the last data release from the HSC survey and will contain the

continued 5 band coverage of  $\sim 1500$  sq degrees of the sky. This is 5 times the sky coverage as the currently available DR2 ( $\sim 300$  sq degrees), meaning sample sizes could be increased up to around 600 galaxies for both the passive and comparison galaxy samples ( $\sim 1200$  altogether). This increase in statistics in the galaxy sample is likely to enable coverage to higher radii than possible in this thesis, as well as an added reduction in possible stochastic fluctuations, meaning that the colour and stellar mass surface density profiles are better constrained.

The main part of the methods presented in Chapter 4 that could be refined includes the masking of foreground and background objects, which rather than being carried out manually, should be automated for such a large sample of galaxies. This may also provide a cleaner and more uniform masking for each set of images. Similarly, a semi-parametric method to automatically classify the morphologies and interaction classes of galaxies could be explored.

The increase in the amount of galaxies in the HSC data would also impact the amount of galaxies available in the deep and ultra-deep fields (as a reminder, we only use the wide survey). These data sets probe 2 magnitudes deeper than the data used in this thesis, meaning even more merger features should be detectable and quantifiable. This could also be used to test studies such as that of [Mancillas et al. \(2019\)](#), to find how the percentage of LSB features varies with surface brightness limits of the data. A study of this type would also help constrain the abundance of ultra-low surface brightness features.

The increase in the amount of galaxies available with HSC imaging would also have a knock-on effect for the amount of galaxies available with corresponding IFU data in surveys such as SAMI or MaNGA. The work carried out here in Chapters 6 and 7 contains only 15 galaxies, with different interaction class sub-samples containing between 2 and 7 galaxies. A five-fold increase in the amount of galaxies available for this type of analysis ( $\sim 75$  galaxies with  $\sim 10$ , 35 and 30 galaxies in different sub-classes) would mean that any differences in the stellar population gradients between different interaction classes (as possibly hinted here) could be confirmed or otherwise. This would provide more solid evidence for the theory postulated by [Remus & Forbes \(2021\)](#), whereby the merger history of a galaxy is imprinted as variations on the stellar population gradients.

Similarly, considering SAMI IFU data only (or conversely MaNGA IFU data), a much wider study of the radial gradients of in- and ex-situ stellar material should be carried out. As outlined in Chapters 1 and 6, much work is starting to emerge from simulations in this field, however a large-scale study of a statistically significant sample of galaxies outside of the local volume is yet to be carried out. With  $\sim 3000$  and  $\sim 10,000$  galaxies available in each survey respectively, biases due to low number statistics are virtually eliminated. This test especially would make a very significant contribution to the field of galaxy evolution in the astronomical community.

Similarly important, although in the pursuit of harder evidence for minor mergers as the drivers of the size evolution of massive galaxies, are two sets of possible observations to be made. The first is with one of the currently available cutting-edge instruments: the European Southern Observatory's (ESO) Multi Unit Spectroscopic Explorer at the Very Large

Telescope (commonly known as VLT-MUSE or MUSE). The second is with a telescope currently under construction and expected to provide a significant leap forward in observations: the European Extremely Large Telescope (E-ELT).

VLT-MUSE is possibly the best IFU instrument currently available, with a field-of-view of 1 arcminute, a spatial scale of 0.2 arcsec and a limiting magnitude of 26.7 in the *i*-band at a resolving power of 180 (mostly comparable to Subaru HSC and the galaxies of interest). Coupled with an 8 metre-class telescope at the Paranal observing site, this combination of instrument and telescope will ensure deep observations for relatively low exposure times. MUSE also has a wavelength coverage of  $\sim 4600 - 9300 \text{ \AA}$  making it possible to use for stellar population fitting of nearby galaxies. A study utilising data of this quality should be able to observe an entire galaxy, including the LSB features. By fitting the IFU data with stellar populations and using the techniques presented in this thesis in combination with deep HSC imaging data, a wide range of properties of the stellar material such as stellar age, stellar mass, metallicity,  $\alpha/\text{Fe}$  and star formation rate could be determined. This could then lend even more solid evidence to the minor merger scenario for the growth of massive galaxies than presented here.

Conversely to studying galaxies in more detail in the local universe, another technique is to search for and quantify similar LSB features at higher redshifts. This could provide evidence that minor merger activity is abundant at multiple redshifts and thereby a continuous process driving the steady size growth of massive galaxies. The E-ELT is set to be a 40 metre-class telescope on its completion in 2023, with the dome completed in 2025 and first light in the same year. One instrument which is likely to be extremely important in a potential study of LSB features at higher redshifts is the Multi-AO Imaging Camera for Deep Observations (MICADO). This imager will cover the wavelengths between 0.8 and  $2 \mu\text{m}$ , with a spatial resolution of between 1.5 and 4 milli-arcsec (mas). This will allow MICADO to resolve similar or better spatial scales as HSC up to redshifts of  $\sim 0.6$ . At the cost of some spatial resolution, observing galaxies at redshifts of 0.7 and above shifts the rest-frame *g*-band into the wavelength range of MICADO, meaning similar optical wavelength SEDs could be fitted.

In summary, this research could be taken in a number of directions in order to either find the last solid evidence of minor mergers driving the size growth of massive galaxies, or more about the nature of the in- and ex-situ fractions of stellar material in galaxies and their respective distributions. Initial efforts should concentrate on the use of current and publicly available archival data to better constrain some of the results presented here. The techniques utilised in this research should be refined to more accurately constrain the results presented here. Finally, preparations for deeper and more detailed observations should be made either with cutting-edge instruments currently available or with upcoming projects due to go online within the next decade.

*"Working up these mountains is as good as it gets, at least as long as you're not freezing or sodden (though even then you feel alive in ways that I don't in modern life behind glass). There is a thrill in the timelessness up there. I have always liked the feeling of carrying on something bigger than me, something that stretches back through other hands and other eyes into the depths of time. To work there is a humbling thing, the opposite of conquering a mountain, if you like; it liberates you from any illusion of self-importance."*

James Rebanks – The Shepherd's life, 2015

# 9

## Conclusion

In this thesis, I (with the help of my collaborators) have investigated the formation, assembly and evolutionary processes of low redshift, massive, central galaxies in an attempt to find observational evidence of minor mergers driving the size evolution of massive galaxies, whereby galaxy sizes increase throughout cosmic time without growing significantly in stellar mass. To do this I used a three-part method: Part I focussed on constraining the stellar mass assembly histories of low redshift, central galaxies; Part II focussed on searching for connections between the LSB material found in the outskirts of such galaxies and the surrounding satellite populations by quantifying the nature of the LSB material; Part III focussed on the effects that minor merger processes may have on the stellar population properties of these galaxies, imprinted in their radial gradients.

In Part I of this work (Chapters 2 and 3), I (with the help of my collaborators) presented the stellar mass assembly of a sample of  $\sim 90,000$  local, central galaxies in groups and clusters above a halo mass  $M_{\text{Halo}} > 10^{12} M_{\odot}$  ( $M_{\text{Stellar}} \gtrsim 10^{9.5} M_{\odot}$ ). I matched SDSS group catalogues from [Yang et al. \(2007\)](#), [Lim et al. \(2017\)](#) and [Blanton et al. \(2005\)](#) to obtain numerous galaxy properties such as halo mass, Sérsic index, number of satellite galaxies, effective radius and Malmquist bias. I then took estimates of the assembly times for 10, 50 and 90 per cent of the stellar mass and the relative growth at various epochs from [Pacifi et al. \(2016\)](#). These estimates were obtained from fitting multi-wavelength photometry from the UV to the NIR with SED models. I then investigated the trends of these stellar assembly times simultaneously in the stellar versus halo mass plane in an attempt to separate secular and environmental processes and the effect they have on galaxy evolution.

I found clear dependencies of all of the stellar assembly lookback times on stellar mass, whereby galaxies with higher stellar masses (at constant halo mass) have on average older lookback times, mirroring downsizing behaviour found by previous studies of galaxy assem-

bly. I also find, however, secondary halo mass dependencies, whereby galaxies with higher halo mass at constant stellar mass have slightly younger assembly times. This is possibly due to either the larger potential of the more massive halo being able to accrete and cool gas more efficiently, or being able to recycle old gas more efficiently. An exception to this behaviour is a sub sample of massive galaxies in relatively small haloes ( $\text{Log}_{10} M_{\text{Stellar}} \sim 11 M_{\odot}$  and  $\text{Log}_{10} M_{\text{Halo}} \sim 12 M_{\odot}$ ). By observing the growth rate throughout cosmic time as well as inspecting the average sSFR, Sérsic indices and the number of satellite galaxies, I conclude that these are likely massive, late-type, field galaxies.

I compared these results to the TNG300 simulation. I found that the simulations predict on average similar stellar assembly lookback times as either a function of stellar or halo mass, with trends generally within the scatter of the observational data. However, differences are found in secondary trends when both stellar and halo mass are simultaneously considered. I found that these differences in behaviour in the assembly times as a function of stellar and halo mass are most noticeable in intermediate stellar mass objects ( $\text{Log}_{10} M_{\text{Stellar}} \sim 10.5 M_{\odot}$  and  $\text{Log}_{10} M_{\text{Halo}} \sim 13 M_{\odot}$ ). I also find that TNG300 predicts that these should be some of the oldest objects in the sample, compared to the youngest in the SDSS sample. Discrepancies in the stellar assembly times on the stellar-halo mass plane also manifest themselves in differences in the quenched fractions between TNG300 and SDSS when these are evaluated simultaneously in bins of stellar and halo masses. As the kinetic mode black hole feedback displays similar behaviour as a function of stellar and halo mass, I tentatively link this to the difference in behaviour between the observations and simulations. A deeper investigation, beyond the scope of this work, would be required to confirm this link.

In Part II of this work (Chapters 4 and 5), I collected deep imaging data (down to surface brightness limits of  $\mu_{r\text{-band}} \sim 28 \text{ mag arcsec}^{-2}$ ) of 118 low redshift, massive, central galaxies from the Subaru HSC-SSP wide survey, which I selected to have assembled 90 per cent of their stellar mass over 6 Gyr ago ( $t_{90} > 6 \text{ Gyr}$ ). I convolved the images with the worst FWHM of the PSFs across the five different bands, masked foreground and background objects and made cuts of  $S/N > 3$  per pixel before using Voronoi binning in order to maximise the  $S/N$  in the outskirts of the galaxies. This method was used to specifically detect and isolate LSB features. I then fitted these Voronoi bins with SEDs using CIGALE to yield stellar mass estimates. I also repeat these processes on a younger comparison sample with  $t_{90} < 4 \text{ Gyr}$ .

Using these stellar mass estimates and the measured  $g$  and  $r$  magnitudes, I constructed radial profiles of  $g - r$  colour and stellar mass surface density. I find that the colour profiles are in good agreement with the previous work of [La Barbera et al. \(2012\)](#). I also find expected declining stellar mass surface density profiles in the inner regions of the sample, but a flattening of the stellar mass surface density profile in the outskirts beyond  $\sim 3 R_{\text{eff,SDSS}}$  ( $\Sigma_* \sim 10^{7.5} M_{\odot} \text{ kpc}^{-2}$ ), driven by the low surface brightness features I observe. I find slightly bluer  $g - r$  colour profiles for the younger comparison sample (0.1 mag difference) and similar behaviour in the stellar mass density surface profiles, namely a declining profile in the central regions with excesses in the outskirts (also with  $\Sigma_* \sim 10^{7.5} M_{\odot} \text{ kpc}^{-2}$ ).

In order to compare to previous studies (cf. [van Dokkum et al. 2010](#)), I then stacked and normalised all images. I fitted profiles to these resulting combined galaxy images and

repeated the above process. I also convolved them with a constructed PSF to investigate whether the PSF wings could make a significant difference to the profile, thereby accounting for the stellar mass surface densities at larger effective radii ( $\gtrsim 2 R_{\text{eff,SDSS}}$ ). I find the colour profiles yielded by this process are in good agreement with previous studies, finding that the stellar mass surface density profiles are smooth and declining at all  $R/R_{\text{eff,SDSS}}$ . I also find that accounting for the wings of the PSF by manually constructing a full PSF has a minimal impact on the profiles, so the PSF wings are unlikely to drive the stellar mass surface densities observed at large radii in the original profiles.

Using visual morphological classification, I also split the sample into three different categories, finding that those that display tidal features make up 42.4 per cent of the sample, similar to previous studies (e.g. [Duc et al. 2015](#)). Those that have no interaction signatures but display a diffuse stellar halo make up 43.2 per cent of the sample and those that are featureless make up only 14.4 per cent of the sample. When I split the profiles by these three morphological classes, I find that those classified in the features sub-sample are the drivers of the stellar mass surface densities at large effective radii ( $\gtrsim 3 R_{\text{eff,SDSS}}$ ) with some contribution from the diffuse sub-sample. I find that the young comparison sample shows similar levels of merger activity, however many more galaxies are featureless and very few display a diffuse halo. I also find that increasing the stellar or halo mass increases the abundance of features or diffuse haloes, similar to previous studies ([Bílek et al. 2020](#)).

I find that the material in these outskirts makes up a minor percentage of the total stellar mass of these systems ( $\sim 8$  per cent beyond  $2 R_{\text{eff,SDSS}}$ ), corresponding to  $\sim 10^{10} M_{\odot}$ . This material has similar  $g - r$  colours to SDSS satellites of  $M_{\text{Stellar}} < 10^{10.5} M_{\odot}$ , leading to a plausible scenario that this material is accreted from the surrounding satellite population via minor mergers.

In Part III of this work (Chapters 6 and 7), I investigated how the assembly histories and interaction states of galaxies may be imprinted on the stellar populations. To do this I selected the sub-sample (15) of the HSC galaxies (from both the passive and comparison samples) with data coverage in the SAMI IFU galaxy survey, known as the SAMI-HSC galaxy sample. I first stacked the spectra in the IFU datacubes into the annuli, determined from the SAMI database ([Green et al. 2018](#)), and discarded any annuli with  $S/N < 20$ , leaving 59 annuli over the 15 galaxies. I then performed stellar population modelling using the MILES stellar library and the STARLIGHT spectral fitting code in order to estimate properties such as the light-weighted stellar age and metallicity. The estimates were complemented with kinematic data from [van de Sande et al. \(2017a,b\)](#). Finally I used the technique developed by [Boecker et al. \(2020\)](#), whereby the annuli spectra are fit using the pPXF fitting code in conjunction with the MILES stellar models. The best weighted combination of stellar populations yielded by the fitting process is compared to empirical models of satellite galaxies in order to determine the fraction of ex-situ stellar material.

I found stellar age and metallicity gradients in agreement with previous studies, and stellar mass surface density profiles in agreement with the estimates derived from the SED fitting processes of Chapters 2 and 3. When I split the SAMI-HSC sample into the three interaction classes contained in Chapters 2 and 3 (features, diffuse and featureless), I find

slight differences. Galaxies in the features sub-sample are younger on average than the diffuse or featureless sub-samples, and galaxies in the featureless are metal-poorer than the features and diffuse sub-samples. When I account for different distributions of stellar mass between different sub-samples, the differences in the age and metallicity profiles remain, indicating intrinsic differences in the stellar population properties of the three sub-samples. When I test for the connection of the gradients to the assembly histories (by inspecting the  $t_{90}$  values of each sub-sample), I find that this is the likely driver of the differences in the stellar population gradients, not interaction morphology.

When I investigate the fraction of ex-situ stars of the SAMI-HSC galaxy sample, I observe an increase in the ex-situ fraction with increasing radius, with ex-situ stars contributing  $\sim 4$  per cent of stellar material at  $0.5 R_{\text{eff,SDSS}}$  to  $\sim 18$  per cent at  $1.5 R_{\text{eff,SDSS}}$ . This is a lower fraction than previous studies using simulations, however with a steeper or shallower increase, depending on the simulation being compared, which themselves differ greatly. Although there is a hint of a slightly larger variation in the behaviour of the ex-situ fraction of stellar material as a function of radius for the features sub-sample than the diffuse or featureless, these differences are minimal, the sample sizes are too small to draw any concrete results and the fitting process is in need of refinement. Altogether, the results presented in Part III hint at slight differences between different interaction classes of galaxies, however these may be linked to the differences in the average assembly history of each sub-sample. These results should be carefully interpreted due to the low sample sizes, however they provide huge potential for future studies.

In summary: I have investigated the formation, assembly and evolutionary processes of low redshift, massive, central galaxies in a consistent manner from start to finish. This was conducted with the aim of finding observational evidence of minor mergers driving the size evolution of massive galaxies. I have found a number of new results in this work, including, but not exclusively, the first direct observational evidence of minor mergers driving the size evolution of massive, central galaxies. I have also presented a number of new methods to investigate such aspects of galaxy formation and evolution which are capable of providing great potential for future studies.

Hence I, Thomas Matthew Jackson, ask the reader to reflect on the quotes at the start of each chapter of this thesis, especially the following section:

*"I have always liked the feeling of carrying on something bigger than me, something that stretches back through other hands and other eyes into the depths of time." – James Rebanks*

In my opinion, this applies just as well to the astronomy research written here that I have dedicated the last 2 years and 8 months of my life to, as to my roots all those years ago on that little, windswept farm on the edge of the Lake District called Wintertarn.

*"The fleeting hour of life of those who love the hills is quickly spent, but the hills are eternal. Always there will be the lonely ridge, the dancing beck, the silent forest: always there will be the exhilaration of the summits. These are for the seeking, and those who seek and find while there is yet time will be blessed both in mind and body."*

Alfred Wainwright – The complete pictorial guides of the Lake District, 1955 - 66



## Appendix: Checks of the Data and Possible Biases

In this Appendix, we present a number of checks into the methods or routines utilised in this thesis. These checks into the reliability of the methods or routines are usually carried out by comparison to previous studies or by comparing the statistics of using different techniques.

Part [A.1](#) shows bias checking of the SED fitting method of [Pacifci et al. \(2016\)](#), by investigating potential AGN contributions and comparing results to other catalogues and techniques. Part [A.2](#) briefly outlines how different selection techniques may or may not affect the selection of observational and simulational sample. These Appendices are relevant for Part I of this thesis contained in Chapters [2](#) and [3](#).

Part [A.3](#) compares the SED fitting carried out in this thesis using CIGALE to the technique of [Pacifci et al. \(2016\)](#). This Appendix is relevant to Part II of this thesis contained in Chapters [4](#) and [5](#).

Part [A.4](#) compares the stellar population fitting using STARLIGHT implemented in this thesis to the line indices method used in the study of [Ferrereras et al. \(2019\)](#). This Appendix is relevant to Part III of this thesis contained in Chapters [6](#) and [7](#).

### A.1 Bias Checking the SED Fitting of [Pacifci et al. \(2016\)](#)

As the matches of an SED to the library of model star formation histories are dependent on the flux of the photometry itself, we decided to check the average SED shape for five sub-samples chosen to represent different populations of galaxies in halo and stellar mass, shown in the left panel of Figure [A.1.1](#). These sub-samples were chosen to have bin widths

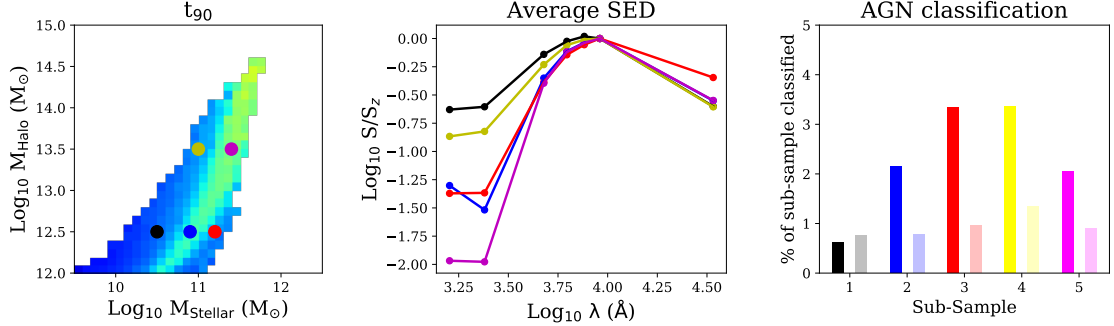


**Figure A.1.1:** **Left-hand panel:** The location in stellar and halo mass space of the five selected sub-samples from our SDSS data. These are selected to occupy different parts of phase space in halo and stellar mass and have significantly different values of  $t_{90}$ . **Central panel:** The average fluxes in each band for the five sub-populations, normalised to the  $z$ -band flux. The  $W1$  flux is noticeably higher for the high stellar-to-halo mass ratio sub-sample. **Right-hand panel:** The fraction of each sub-population selected as an AGN via either BPT (from [Kauffmann et al. 2003](#), solid bars) or MIR selection (from [Assef et al. 2018](#), shaded bars).

of 0.2 dex in both halo and stellar mass and to contain a minimum of 50 galaxies. This was done in order to verify if any of the sub-populations had systematic biases that could affect our results. The mean photometric flux for each sub-sample in every photometric band was calculated and then normalised to the flux in the  $z$ -band, as this was the peak flux in four of the five sub-samples. This is shown in the central panel of Figure A.1.1. We see raised levels of UV flux in sub samples 1 and 4 (black and yellow line,  $\text{Log}_{10} M_{\text{Stellar}} \sim 10.5 M_{\odot}$  and  $\text{Log}_{10} M_{\text{Halo}} \sim 12.5 M_{\odot}$  and  $\text{Log}_{10} M_{\text{Stellar}} \sim 11 M_{\odot}$  and  $\text{Log}_{10} M_{\text{Halo}} \sim 13.5 M_{\odot}$  respectively) due to their raised level of star formation, as expected from Figure 2.1.1. We also notice the raised  $z$  -  $W1$  flux of sub-sample 3, our high stellar-to-halo mass objects (red line,  $\text{Log}_{10} M_{\text{Stellar}} \sim 11 M_{\odot}$  and  $\text{Log}_{10} M_{\text{Halo}} \sim 12.5 M_{\odot}$ ), which is responsible for the high SFR estimates from the SED fitting.

AGN emission can significantly contribute to the IR flux, especially in the MIR bands ([Rosario et al. 2016](#)). Although type 1 AGN are removed from the catalogue of [Pacifici et al. \(2016\)](#), type 2 AGN may still contribute to some of the IR emission. In order to check that this phenomenon was not biasing the SFR estimates and therefore the assembly histories in any of the sub-populations, with our high stellar-to-halo mass sub-population in particular, we cross matched the AGN catalogues of [Kauffmann et al. \(2003\)](#) and [Assef et al. \(2018\)](#) with each sub-sample. We then calculated the percentage of each sub-sample that shows clear AGN activity, which can be seen in the right-hand panel of Figure A.1.1. The solid bar for each sub-sample represents the percentage of galaxies found with AGN using the selection criteria of [Kauffmann et al. \(2003\)](#) which are selected using the BPT selection criteria ([Baldwin, Phillips & Terlevich 1981](#)), and the shaded bar for each sub-sample represents those found in [Assef et al. \(2018\)](#), which are identified using WISE MIR colour-colour selection. We see that the AGN fraction is consistently less than 5 per cent for all sub-samples in both selection criteria, and that sub-sample 3, our high stellar-to-halo mass objects, does not have a significantly higher fraction of AGN using either selection criteria, implying that it is unlikely that AGN

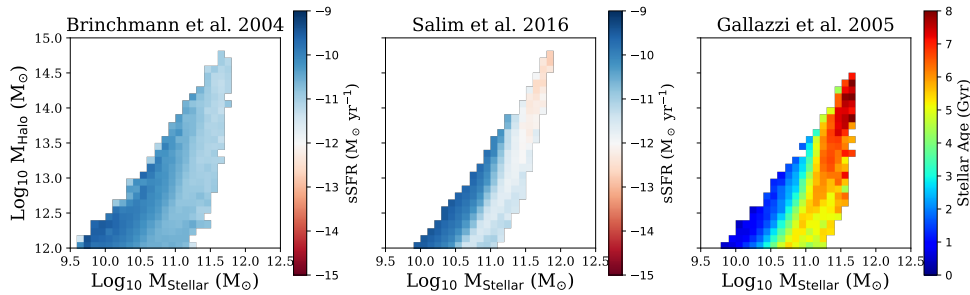


**Figure A.1.2:** **Left-hand panel:** The sSFR as a function of halo and stellar mass as determined by [Brinchmann et al. \(2004\)](#), from using a mixture of emission lines and the 4000 Å break. **Central panel:** The sSFR as a function of stellar and halo mass for our SDSS sample as estimated in the work of [Salim et al. \(2016\)](#), which used SED fitting to determine stellar masses and SFRs. **Right-hand panel:** The luminosity weighted stellar ages as a function of stellar and halo mass from [Gallazzi et al. \(2005\)](#). We see similar average trends as a function of stellar and halo mass as inferred from the SED fitting method of [Pacifi et al. \(2016\)](#), albeit at somewhat different strengths due to differences in each SED fitting method, thereby showing the average trends are unlikely to be biased by our SED fitting method.

emission biases the SFHs of this sub-sample.

We also took data from the catalogues of [Brinchmann et al. \(2004\)](#) and [Salim et al. \(2016\)](#). Although these two catalogues do not contain mass assembly histories, we checked the stellar and halo mass distributions versus the sSFR, using the stellar mass and SFR estimates from each catalogue for consistency with the halo mass estimates from [Lim et al. \(2017\)](#). If there is a systematic bias in the SED fitting method of [Pacifi et al. \(2016\)](#), then these two catalogues should not reproduce the trends in the sSFR, stellar mass-halo mass plane we observe in Figure 2.1.1. [Brinchmann et al. \(2004\)](#) combine data from SDSS DR4 ([Adelman-McCarthy et al. 2006](#)) and a Bayesian approach to estimating SFRs and stellar masses from a mixture of emission lines and the 4000 Å Balmer break. [Salim et al. \(2016\)](#), alternatively, fit multi-wavelength photometry from *GALEX*, SDSS and *WISE* with the SED fitting code CIGALE ([Noll et al. 2009](#)). By cross-matching these two catalogues with [Lim et al. \(2017\)](#), we compared the sSFR as a function of stellar mass and halo mass, shown in Figure A.1.2. We note that both catalogues have higher upper limits on the sSFR than the catalogue of [Pacifi et al. \(2016\)](#), meaning we searched for a replication of the general trends rather than absolute values.

The left-hand panel of Figure A.1.2 shows the sSFR as a function of both stellar mass and halo mass from [Brinchmann et al. \(2004\)](#). We see subtle trends as a function of both stellar and halo mass, confirming the secondary dependencies we see in Figure 2.1.1. We also see that the most massive galaxies ( $\text{Log}_{10} M_{\text{Stellar}} \sim 11.5 M_{\odot}$ ,  $\text{Log}_{10} M_{\text{Halo}} \sim 14 M_{\odot}$ ) have the lowest sSFRs and that the highest stellar-to-halo mass objects ( $\text{Log}_{10} M_{\text{Stellar}} \sim 11 M_{\odot}$  and  $\text{Log}_{10} M_{\text{Halo}} \sim 12$ ) have slightly higher sSFRs compared to objects of similar stellar mass but higher halo mass. These average trends are replicated, with more clear differences

in various sub-populations, in the central panel from the catalogue of [Salim et al. \(2016\)](#).

We also use stellar mass and luminosity weighted stellar age estimations derived from SDSS spectra from [Gallazzi et al. \(2020\)](#), method based on [Gallazzi et al. \(2005\)](#) and outlined in [Pasquali et al. \(2019\)](#)), in order to compare if spectroscopic techniques also reproduce our average trends in stellar and halo mass, this can be seen in the right-hand panel of Figure A.1.2. We see similar average trends reproduced as in Figures 2.1.1 and 3.1.1. We argue that the tests carried out in this section mean that the average trends found in previous sections are to a good degree of confidence, reliable.

## A.2 Selection Effects and Sample Matching Between SDSS and TNG300

As mentioned in Section 2.4, to be able to make a meaningful comparison between the observed and simulated data sets, some level of matching needs to be applied. Techniques such as stellar or halo mass matching, star formation rate or colours are commonly used. We chose not to match in these factors as we would significantly reduce the size of our SDSS observational sample and we wanted to compare how well TNG300 reproduced the trends in stellar-to-halo mass with respect to the other variables, in order to best observe the trends produced by environmental and secular processes. We briefly consider other possibly matching techniques and their possible effects on the results.

Due to cross-matching multiple group catalogues, which resulted in the loss of a significant number of galaxies, it is extremely difficult to calculate the volume of the observational sample, and beyond the scope of this work. We assume that TNG300 has a smaller volume than our observational sample due to the smaller sample size. This could mean that statistically we do not see the observed trend due to less extreme objects, however we argue that a ratio of 1:2 in the sample size difference would not be enough to hide the prominent behaviour of the highest stellar-to-halo mass objects and the differences in galaxies at intermediate stellar mass, which TNG300 should sample well.

[Jackson et al. \(2020c\)](#) applied a matching criterion between an observational and simulational sample of low redshift AGN. They used the Cartesian coordinates of each galaxy within the simulation box to calculate the distance from the centre of the simulation box. This was then combined with the luminosities of each galaxy to yield the fluxes, which could then be used to make a cut, mimicking the survey sensitivity limits. We repeated the same exercise here, from 100 different locations in the simulation box, in order to observe if a significant amount of objects were cut from the TNG300 sample according to the SDSS magnitude limit. We find that less than 1 per cent of all central galaxies above a stellar mass of  $10^9 M_{\odot}$  fall under the magnitude limit at any point in the simulation box, meaning the survey limit does not heavily bias our results. We tentatively conclude that selection effects from instrument sensitivity are unlikely to cause the differences we see between the observational and simulational trends.

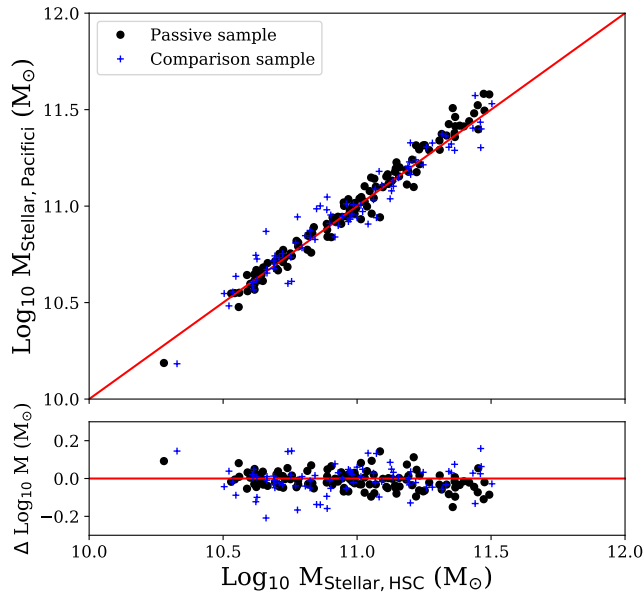


**Figure A.3.1:** **Top panel:** A comparison of the stellar mass estimates from the study of [Pacifici et al. \(2016\)](#) with the estimates yielded from CIGALE for the central regions of the HSC data. **Bottom panel:** The difference in log-space between the two different methods.

### A.3 Exploration of Biases in the Stellar Mass Estimates from CIGALE

One source of bias in a number of our results may come from the SED fitting we apply to the imaging data. In order to check that our stellar mass estimates are consistent with previous work, we compare total stellar mass estimates from our SED fitting using CIGALE on the HSC imaging data to the stellar mass estimates from the parent sample in [Jackson et al. \(2020b\)](#), which are derived from [Pacifici et al. \(2016\)](#) (see Section 4.1 or [Pacifici et al. 2012, 2016](#), for more detail). We measure the fluxes within the same aperture sizes (SDSS Petrosian radius) from our HSC imaging data as those used in [Pacifici et al. \(2016\)](#) for consistency.

The results of our comparison of the stellar masses are shown in Figure A.3.1. In the top panel, we see a tight correlation between the estimates from the HSC data computed by CIGALE and the routine from [Pacifici et al. \(2016\)](#). The bottom panel of Figure A.3.1 shows that there are no obvious systematic trends or outliers in both our passive galaxy sample and the comparison sample, with maximum differences in the estimates of  $\sim 0.2$  dex (within the observational uncertainties). This confirms that our data and SED fitting routine are consistent with previous estimates, and therefore should have a good level of reliability when applied to the outskirts of our galaxy sample.

The star formation history used in generating models for SED fitting routines is also a potential source of bias. Recent studies such as that of [Leja et al. \(2020\)](#) have shown that

using different star formation histories, including non-parametric ones, can cause differences of 0.1 - 1 dex in the stellar mass estimates. In order to check this potential source of bias we also ran our SED fitting with CIGALE assuming a delayed star formation history on all Voronoi bins in the passive galaxy sample, including those in the outskirts of the galaxies. The estimates of stellar mass yielded had a median difference of 0.1 dex with a maximum difference of 0.3 dex, generally within the estimated uncertainties of the stellar mass. This means that the radial profiles did not change significantly. This combined with the agreement between our estimates for the central regions of the galaxy samples and those from [Pacifi et al. \(2016\)](#), which use non-parametric star formation histories, indicates our SED fitting does not significantly bias our results.

Redshift biases may also be present in our morphological classification. At larger distances or higher redshifts, the sensitivity level of the survey means that we do not probe to as deep in surface brightness, meaning that some low surface brightness features may be missed and a galaxy classified as displaying no merger activity when there may be activity below the sensitivity level of the survey. To investigate possible biases we plot the redshift distributions of each sub-sample in redshift space and compare them in the bottom right panels of Figure 4.1.1.

## A.4 Comparing the Estimates of Stellar Populations from Different Methods

As stated in Chapter 1, previous studies using stellar population fitting have found general agreement in the age and metallicity gradients of the general galaxy population as a function of stellar mass. They may, however, disagree on dependencies with other parameters such as environment ([Sánchez-Blázquez et al. 2014](#); [Goddard et al. 2017a](#)). Some of these differences may be attributed to the use of different stellar population libraries, which can differ in that they are theoretical versus empirical or can weight evolved stellar populations such as post-AGB stars more or less heavily. Similarly the fitting code and the methods it employs therein (e.g. least squares fitting, sigma clipping of certain wavelengths, Monte-Carlo methods) can also create systematic biases in the estimates of certain stellar population properties. These differences in approach may create systematic differences in the estimates of the stellar population properties of the same spectra and hence the results or interpretation of the studies they are applied to.

In order to investigate if the different stellar population fitting methods applied in this thesis contain major biases, we provide a comparison here of the estimations of stellar age and metallicity obtained by the fitting codes STARLIGHT and pPXF for the subset of our SAMI-HSC sample also contained in the study of [Ferrer et al. \(2019\)](#). In their study, [Ferrer et al. \(2019\)](#) use line index methods, which concentrate on indices such as  $Mgb$  and  $H\beta$  in order to determine stellar ages and metallicities. This comparison is shown in Figure A.4.1.

The top left-hand panel of Figure A.4.1 shows the comparison of the estimated stellar ages obtained from STARLIGHT versus the study of [Ferrer et al. \(2019\)](#), represented by the black points with associated errors, with a one-to-one agreement indicated by the solid

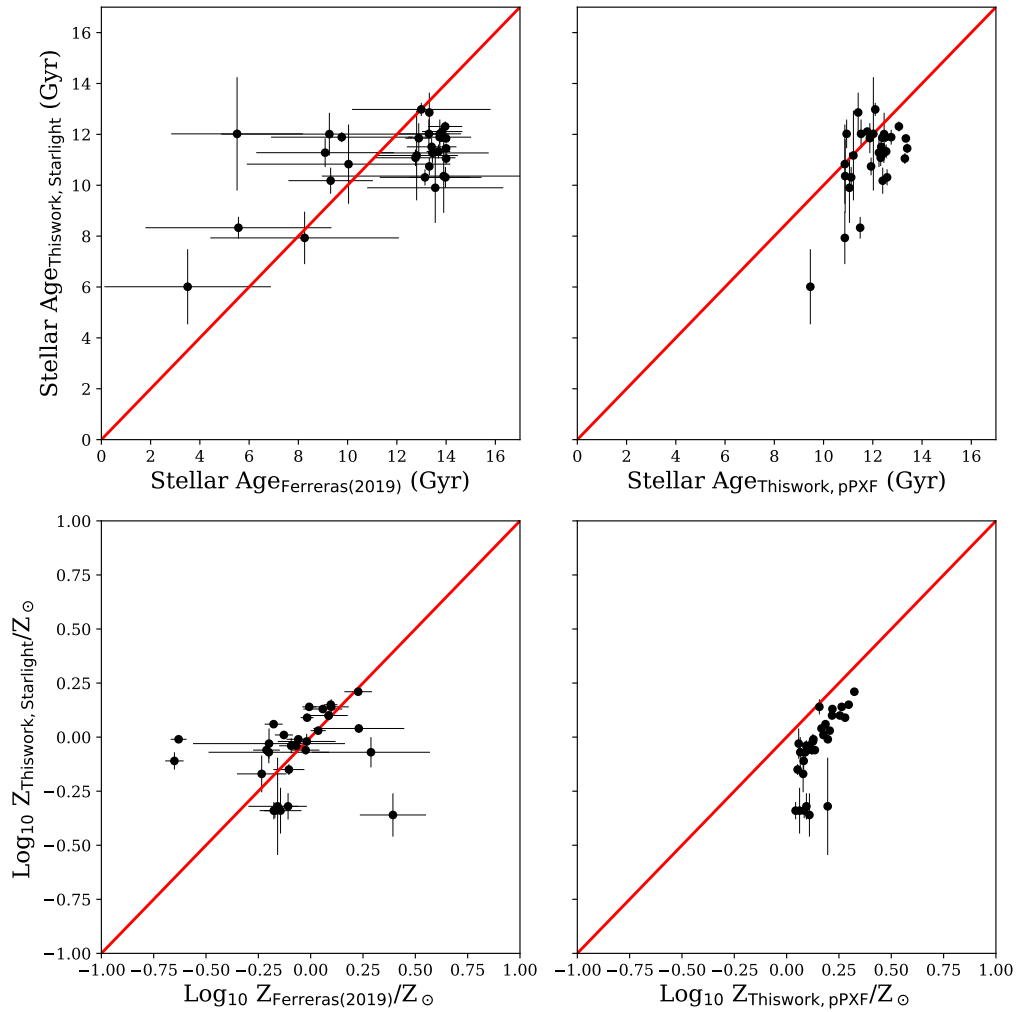


**Figure A.4.1:** **Top panels:** A comparison of the estimated light-weighted stellar ages for the annuli contained in both our sample using STARLIGHT and the study of Ferreras et al. (2019, left panel), who use line index methods to estimate stellar population properties, and between STARLIGHT and pPXF in this work (right panel). A one to one agreement is indicated by the solid red line. **Bottom panels:** A similar comparison between the three methods but for the estimated metallicities.

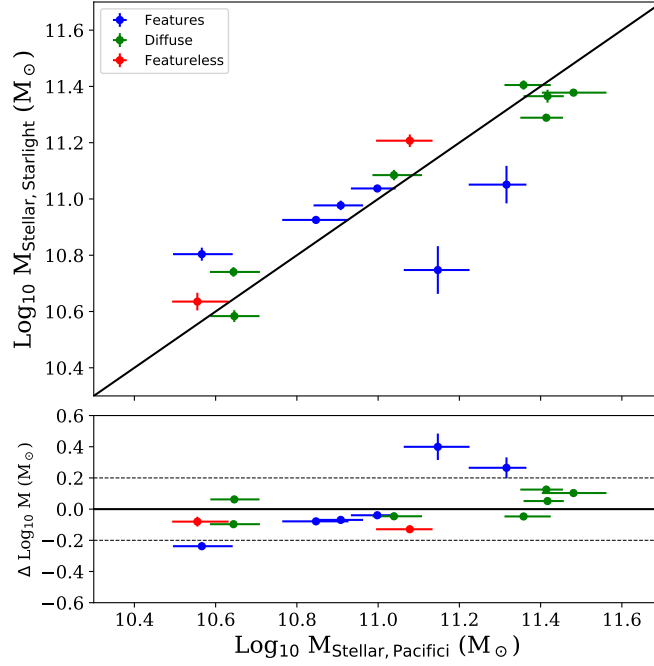


**Figure A.4.2:** A comparison of the integrated stellar masses obtained from the SED fitting process of [Pacifci et al. \(2016\)](#) and the integrated stellar masses obtained by fitting the IFU data from the SAMI survey with stellar populations. **Top panel:** The direct comparison, with residuals in the bottom panel. The coloured points indicate the different interaction classes (features - blue, diffuse - green and featureless - red), with the solid black line indicating a one-to-one agreement. The dashed lines in the residuals indicate the 0.2 dex uncertainty which is expected in such measurements.

red line. We see a fairly large scatter in the stellar ages, however most values agree within the associated uncertainties, which can be up to 3 Gyr. The top right-hand panel shows the difference between the estimates obtained from STARLIGHT and pPXF. We see a smaller scatter and generally good agreement, however with possible lower agreements at younger ages, whereby pPXF appears to overestimate the stellar ages. These, however, are lower S/N annuli, which pPXF struggles due to the regularisation.

The bottom left and bottom right panels of [Figure A.4.1](#) shows the comparison of the estimated stellar metallicities obtained from STARLIGHT versus the study of [Ferreras et al. \(2019\)](#) and STARLIGHT versus pPXF respectively, with the same black points and one-to-one agreement as the top two panels. We see a better agreement here between all methods, with differences minimised apart from a few outliers. These outliers have been thoroughly checked manually, with no obvious explanation to the difference in the estimations. One postulation may be due to the shape of the continuum, which may affect line index measurements less, although a thorough test of the systematic biases the continuum may have on estimates is beyond the scope of this work.

Altogether, although we find some scatter in our estimates of stellar ages and metallic-

ities, the estimations generally have uncertainties in which the one-to-one agreement lies. We are still fairly confident that the fitting methods we have utilised in this work are reliable.

As an extra check, we can also compare the integrated stellar mass estimates obtained from fitting the SAMI-HSC galaxy sample using `STARLIGHT` and summing all annuli of each galaxy to the estimates obtained from the SED fitting measurements of [Pacifci et al. \(2016\)](#), presented in Section 2.2). The top panel shows a comparison of the integrated stellar masses yielded by the two methods, with a one-to-one agreement indicated by the solid black line for all three interaction classes (features - blue, diffuse - green and featureless - red, see Section 4.2 for more details). The bottom panel presents the residual values, with the dashed line indicating the 0.2 dex uncertainties expected on average by such fitting methods.

We see good agreement of the integrated stellar mass estimates yielded by stellar population fitting and SED fitting, with nearly all galaxies within the 0.2 dex uncertainties. Those galaxies which lie outside of these uncertainties belong to the features sub-sample, and are likely biased. This is because the photometric SED fitting process uses Petrosian apertures which are generally larger in extent than the IFU data, and which are likely to be exacerbated by possible tidal features due to following the extent of the light distribution, biasing stellar mass measurements.



# Acknowledgments

## **I, Thomas Matthew Jackson would like to personally thank the following people:**

Firstly, my collaborators and co-authors throughout the course of this research for their insightful discussion, helpful suggestions and constant support. This includes Dr. Anna Pasquali, Dr. Francesco La Barbera, Dr. Surhud More, Dr. Camilla Pacifici, Dr. Annalisa Pillepich, Mr Christoph Engler, Ms Alina Böcker, Dr. Rory Smith and Prof. Dr. Eva K. Grebel.

Secondly, collaborators involved in other projects, either in AGN research such as Prof. Dr. David Alexander, Dr. David Rosario, Dr. Stuart McAlpine, Dr. Jan Scholtz, Prof. Dr. Richard Bower and Dr. Sarah Leslie or in large scale environmental research such as Mr Niko Winkel.

Thirdly, researchers and technicians who have helped by giving advice and discussing problems at various stages of research: such as Dr. Andy Goulding with his advice and input on the use of the HSC imaging data, Dr. Song Huang for advice and input on sky background issues in HSC imaging data and Mr Owen Vincent and Mr Dominic Kempf for their services in setting up access to computing power and parallelisation of the stellar population fitting codes.

Finally, Dr. Robert Harris, Mr Jacob Isbell and Mr William Lamb for their scientific discussion throughout this thesis and their help in bringing this work together and comments on the final thesis.

## **I would also like to acknowledge the following collaborations, funds, teams and projects:**

Thomas Jackson is a Fellow of the International Max Planck Research School for Astronomy and Cosmic Physics at the University of Heidelberg (IMPRS-HD).

Thanks go to Dr. Anna Gallazzi for the use of her SDSS based catalogue to compare age estimates from the SED fitting with estimates obtained from stellar population fitting.

Thanks go to the IllustrisTNG team for making their data publically available.

The flagship simulations of the IllustrisTNG project used in this research have been run on the HazelHen Cray XC40-system at the High Performance Computing Center Stuttgart as part of project GCS-ILLU of the Gauss centres for Super-computing(GCS). Ancillary and test runs of the project were also run on the Stampede supercomputer at TACC/XSEDE (allocation AST140063), at the Hydra and Draco supercomputers at the Max Planck Computing and Data Facility, and on the MIT/Harvard computing facilities supported by FAS and MIT MKI.

Funding for the Sloan Digital Sky Survey IV has been provided by the Alfred P. Sloan Foundation, the U.S. Department of Energy Office of Science, and the Participating Institutions.

SDSS-IV acknowledges support and resources from the Center for High-Performance Computing at the University of Utah. The SDSS web site is [www.sdss.org](http://www.sdss.org).

SDSS-IV is managed by the Astrophysical Research Consortium for the Participating Institutions of the SDSS Collaboration including the Brazilian Participation Group, the Carnegie Institution for Science, Carnegie Mellon University, the Chilean Participation Group, the French Participation Group, Harvard-Smithsonian Center for Astrophysics, Instituto de Astrofísica de Canarias, The Johns Hopkins University, Kavli Institute for the Physics and Mathematics of the Universe (IPMU) / University of Tokyo, the Korean Participation Group, Lawrence Berkeley National Laboratory, Leibniz Institut für Astrophysik Potsdam (AIP), Max-Planck-Institut für Astronomie (MPIA Heidelberg), Max-Planck-Institut für Astrophysik (MPA Garching), Max-Planck-Institut für Extraterrestrische Physik (MPE), National Astronomical Observatories of China, New Mexico State University, New York University, University of Notre Dame, Observatório Nacional / MCTI, The Ohio State University, Pennsylvania State University, Shanghai Astronomical Observatory, United Kingdom Participation Group, Universidad Nacional Autónoma de México, University of Arizona, University of Colorado Boulder, University of Oxford, University of Portsmouth, University of Utah, University of Virginia, University of Washington, University of Wisconsin, Vanderbilt University, and Yale University.

This research makes use of data products from the Wide-field Infrared Survey Explorer, which is a joint project of the University of California, Los Angeles, and the Jet Propulsion Laboratory/California Institute of Technology, funded by the National Aeronautics and Space Administration.

*GALEX* (Galaxy Evolution Explorer) is a NASA Small Explorer, launched in 2003 April. We gratefully acknowledge NASAs support for the construction, operation, and science analysis for the *GALEX* mission, developed in cooperation with the Centre National d'Etudes Spatiales of France and the Korean Ministry of Science and Technology.

This research is based in part on data collected at the Subaru Telescope and retrieved from the HSC data archive system, which is operated by Subaru Telescope and Astronomy Data Center at National Astronomical Observatory of Japan. Data analysis was in part carried out with the cooperation of Center for Computational Astrophysics, National Astronomical Observatory of Japan.

The Hyper Suprime-Cam (HSC) collaboration includes the astronomical communities of Japan and Taiwan, and Princeton University. The HSC instrumentation and software were developed by the National Astronomical Observatory of Japan (NAOJ), the Kavli Institute for the Physics and Mathematics of the Universe (Kavli IPMU), the University of Tokyo, the High Energy Accelerator Research Organization (KEK), the Academia Sinica Institute for Astronomy and Astrophysics in Taiwan (ASIAA), and Princeton University. Funding was contributed by the FIRST program from Japanese Cabinet Office, the Ministry of Education, Culture, Sports, Science and Technology (MEXT), the Japan Society for the Promotion of Science (JSPS), Japan Science and Technology Agency (JST), the Toray Science Foundation, NAOJ, Kavli IPMU, KEK, ASIAA, and Princeton University.

This research makes use of software developed for the Large Synoptic Survey Telescope. We

---

thank the LSST Project for making their code available as free software at <http://dm.lsst.org>  
Thanks go to the Virgo consortium and EAGLE team for making the data from their simulations public.

This research used the DiRAC Data Centric system at Durham University, operated by the Institute for Computational Cosmology on behalf of the STFC DiRAC HPC Facility. This equipment was funded by BIS National E-infrastructure capital grant ST/K00042X/1, STFC capital grant ST/H008519/1, and STFC DiRAC Operations grant ST/K003267/1 and Durham University. DiRAC is part of the National E-Infrastructure.

The SAMI Galaxy Survey is based on observations made at the Anglo-Australian Telescope. The Sydney-AAO Multi-object Integral field spectrograph (SAMI) was developed jointly by the University of Sydney and the Australian Astronomical Observatory. The SAMI input catalogue is based on data taken from the Sloan Digital Sky Survey, the GAMA Survey and the VST ATLAS Survey. The SAMI Galaxy Survey website is <http://sami-survey.org/>. The SAMI Galaxy Survey is supported by the Australian Research Council Centre of Excellence for All Sky Astrophysics in 3 Dimensions (ASTRO 3D), through project number CE170100013, the Australian Research Council Centre of Excellence for All-sky Astrophysics (CAASTRO), through project number CE110001020, and other participating institutions. Based on data acquired at the Anglo-Australian Telescope under programs A/2013B/012 and A/2016B/16. We acknowledge the traditional owners of the land on which the AAT stands, the Gamilaraay people, and pay our respects to elders past and present. GAMA is a joint European-Australasian project based around a spectroscopic campaign using the Anglo-Australian Telescope. The GAMA input catalogue is based on data taken from the Sloan Digital Sky Survey and the UKIRT Infrared Deep Sky Survey. Complementary imaging of the GAMA regions is being obtained by a number of independent survey programmes including GALEX MIS, VST KiDS, VISTA VIKING, WISE, Herschel-ATLAS, GMRT and ASKAP providing UV to radio coverage. GAMA is funded by the STFC (UK), the ARC (Australia), the AAO, and the participating institutions. The GAMA website is <http://www.gama-survey.org/>.

Thanks go to the Scientific Software Center in Heidelberg for allowing access to a computer cluster to run the Monte-Carlo methods for the errors on the stellar population fitting and for help in parallelising the codes.



---

## Publications

### First author papers included in this thesis:

*The stellar mass assembly of low redshift, massive, central galaxies in SDSS and the TNG300 simulation*

Thomas M. Jackson, A. Pasquali, C. Pacifici, C. Engler, A. Pillepich, E. K. Grebel, 2020, MNRAS, 497, 4262

*The nature and origins of the low surface brightness outskirts of massive, central galaxies in Subaru HSC*

Thomas M. Jackson, A. Pasquali, F. La Barbera, S. More, E. K. Grebel (subm. MNRAS, arxiv:2102.02241)

*The connection between minor merger activity and stellar population gradients in SAMI galaxies*

Thomas M. Jackson, Alina Boecker, Anna Pasquali, Francesco La Barbera, Rory Smith, Eva K. Grebel (in prep.)

### First author papers not included in this thesis:

*The star-formation properties of nearby AGN in the observed and simulated universe: BAT vs EAGLE*

Thomas M. Jackson, D.J.Rosario, D.M.Alexander, J. Scholtz, S. M. McAlpine, R. G. Bower, 2020, MNRAS, 498, 2323

*The impact of high luminosity SMBH accretion events on star formation: A view from EAGLE*

Thomas M. Jackson, D.J.Rosario, D.M.Alexander, S. M. McAlpine, A. Pasquali, J. Scholtz, R. G. Bower (in prep.)

### Co-author papers not included in this thesis:

*The imprint of cosmic web quenching on galaxy evolution* N. Winkel, A. Pasquali, K. Kraljic, R. Smith, A. Gallazzi, T. M. Jackson (subm. MNRAS)

*A correlation between BCG position angle and large scale structure spanning 10 Mpc*

Rory Smith, Ho Seong Hwang, Katarina Kraljic, Thomas M. Jackson, Anna Pasquali, Paula Calderón-Castillo, Jihye Shin, Jongwan Ko, Jaewon Yoo, Hyowon Kim, and Jaewoo Kim (subm. ApJ)



## References

- Abazajian K. N., et al., 2009, *ApJS*, **182**, 543
- Adelman-McCarthy J. K., et al., 2006, *ApJS*, **162**, 38
- Ahn C. P., et al., 2014, *ApJS*, **211**, 17
- Aihara H., et al., 2018, *PASJ*, **70**, S8
- Aihara H., et al., 2019, *PASJ*, **71**, 114
- Albaret F. D., et al., 2017, *ApJS*, **233**, 25
- Asari N. V., Cid Fernandes R., Stasińska G., Torres-Papaqui J. P., Mateus A., Sodré L., Schoenell W., Gomes J. M., 2007, *MNRAS*, **381**, 263
- Assef R. J., Stern D., Noirot G., Jun H. D., Cutri R. M., Eisenhardt P. R. M., 2018, *ApJS*, **234**, 23
- Atkinson A. M., Abraham R. G., Ferguson A. M. N., 2013, *ApJ*, **765**, 28
- Baldwin J. A., Phillips M. M., Terlevich R., 1981, *PASP*, **93**, 5
- Banerji M., et al., 2010, *MNRAS*, **406**, 342
- Bell E. F., McIntosh D. H., Katz N., Weinberg M. D., 2003, *ApJS*, **149**, 289
- Bezanson R., van Dokkum P. G., Tal T., Marchesini D., Kriek M., Franx M., Coppi P., 2009, *ApJ*, **697**, 1290
- Bílek M., et al., 2020, *MNRAS*, **498**, 2138
- Blanton M. R., et al., 2005, *AJ*, **129**, 2562
- Bluck A. F. L., Maiolino R., Sánchez S. F., Ellison S. L., Thorp M. D., Piotrowska J. M., Teimoorinia H., Bundy K. A., 2020, *MNRAS*, **492**, 96
- Boecker A., Leaman R., van de Ven G., Norris M. A., Mackereth J. T., Crain R. A., 2020, *MNRAS*, **491**, 823
- Boquien M., Burgarella D., Roehlly Y., Buat V., Ciesla L., Corre D., Inoue A. K., Salas H., 2019, *A&A*, **622**, A103

---

Bosch J., et al., 2018, [PASJ](#), **70**, S5

Bower R. G., Benson A. J., Malbon R., Helly J. C., Frenk C. S., Baugh C. M., Cole S., Lacey C. G., 2006, [MNRAS](#), **370**, 645

Brinchmann J., Charlot S., White S. D. M., Tremonti C., Kauffmann G., Heckman T., Brinkmann J., 2004, [MNRAS](#), **351**, 1151

Bruzual G., Charlot S., 2003, [MNRAS](#), **344**, 1000

Bryant J. J., et al., 2015, [MNRAS](#), **447**, 2857

Bundy K., et al., 2015, [ApJ](#), **798**, 7

Burgarella D., Buat V., Iglesias-Páramo J., 2005, [MNRAS](#), **360**, 1413

Callingham T. M., et al., 2019, [MNRAS](#), **484**, 5453

Calzetti D., Armus L., Bohlin R. C., Kinney A. L., Koornneef J., Storchi-Bergmann T., 2000, [ApJ](#), **533**, 682

Cappellari M., 2017, [MNRAS](#), **466**, 798

Cappellari M., Copin Y., 2003, [MNRAS](#), **342**, 345

Cappellari M., et al., 2013, [MNRAS](#), **432**, 1862

Cardelli J. A., Clayton G. C., Mathis J. S., 1989, [ApJ](#), **345**, 245

Carlberg R. G., 1984, [ApJ](#), **286**, 403

Carnall A. C., McLure R. J., Dunlop J. S., Davé R., 2018, [MNRAS](#), **480**, 4379

Carnall A. C., et al., 2020, [MNRAS](#), **496**, 695

Carter D., 1979, [MNRAS](#), **186**, 897

Chabrier G., 2003, [PASP](#), **115**, 763

Charlot S., Fall S. M., 2000, [ApJ](#), **539**, 718

Cid Fernandes R., Mateus A., Sodré L., Stasińska G., Gomes J. M., 2005, [MNRAS](#), **358**, 363

Cimatti A., et al., 2008, [A&A](#), **482**, 21

Conroy C., Gunn J. E., White M., 2009, [ApJ](#), **699**, 486

Cowie L. L., Songaila A., Hu E. M., Cohen J. G., 1996, [AJ](#), **112**, 839

Crain R. A., et al., 2015, [MNRAS](#), **450**, 1937

Croom S. M., et al., 2012, [MNRAS](#), **421**, 872

- 
- Daddi E., Cimatti A., Renzini A., Fontana A., Mignoli M., Pozzetti L., Tozzi P., Zamorani G., 2004, [ApJ](#), **617**, 746
- Daddi E., et al., 2005, [ApJ](#), **626**, 680
- Dale D. A., Helou G., Magdis G. E., Armus L., Díaz-Santos T., Shi Y., 2014, [ApJ](#), **784**, 83
- Dalla Vecchia C., Schaye J., 2012, [MNRAS](#), **426**, 140
- Davé R., Anglés-Alcázar D., Narayanan D., Li Q., Rafieferantsoa M. H., Appleby S., 2019, [MNRAS](#), **486**, 2827
- Davison T. A., Norris M. A., Pfeffer J. L., Davies J. J., Crain R. A., 2020, [MNRAS](#), **497**, 81
- De Lucia G., 2011, [Astrophysics and Space Science Proceedings](#), **27**, 203
- De Lucia G., Blaizot J., 2007, [MNRAS](#), **375**, 2
- Doi M., et al., 2010, [AJ](#), **139**, 1628
- Donnari M., et al., 2019, [MNRAS](#), **485**, 4817
- Dressler A., Lynden-Bell D., Burstein D., Davies R. L., Faber S. M., Terlevich R., Wegner G., 1987, [ApJ](#), **313**, 42
- Dubois Y., et al., 2014, [MNRAS](#), **444**, 1453
- Duc P.-A., 2020, arXiv e-prints, [p. arXiv:2007.13874](#)
- Duc P.-A., et al., 2015, [MNRAS](#), **446**, 120
- Faber S. M., Jackson R. E., 1976, [ApJ](#), **204**, 668
- Falcón-Barroso J., Sánchez-Blázquez P., Vazdekis A., Ricciardelli E., Cardiel N., Cenarro A. J., Gorgas J., Peletier R. F., 2011, [A&A](#), **532**, A95
- Fan L., Lapi A., De Zotti G., Danese L., 2008, [ApJL](#), **689**, L101
- Fan L., Lapi A., Bressan A., Bernardi M., De Zotti G., Danese L., 2010, [ApJ](#), **718**, 1460
- Feldmann R., Carollo C. M., Mayer L., Renzini A., Lake G., Quinn T., Stinson G. S., Yepes G., 2010, [ApJ](#), **709**, 218
- Ferland G. J., Korista K. T., Verner D. A., Ferguson J. W., Kingdon J. B., Verner E. M., 1998, [PASP](#), **110**, 761
- Ferland G. J., et al., 2017, [RMxAA](#), **53**, 385
- Ferreras I., Lisker T., Pasquali A., Khochfar S., Kaviraj S., 2009, [MNRAS](#), **396**, 1573
- Ferreras I., et al., 2014, [MNRAS](#), **444**, 906

- 
- Ferreras I., et al., 2019, [MNRAS](#), **489**, 608
- Fitzpatrick E. L., 1999, [PASP](#), **111**, 63
- Furlong M., et al., 2015, [MNRAS](#), **450**, 4486
- Gallazzi A., Charlot S., Brinchmann J., White S. D. M., Tremonti C. A., 2005, [MNRAS](#), **362**, 41
- Gallazzi A. R., Pasquali A., Zibetti S., La Barbera F., 2020, arXiv e-prints, [p. arXiv:2010.04733](#)
- Genel S., et al., 2014, [MNRAS](#), **445**, 175
- Genel S., et al., 2018, [MNRAS](#), **474**, 3976
- Goddard D., et al., 2017a, [MNRAS](#), **465**, 688
- Goddard D., et al., 2017b, [MNRAS](#), **466**, 4731
- Gott J. Richard I., 1975, [ApJ](#), **201**, 296
- Green A. W., et al., 2018, [MNRAS](#), **475**, 716
- Hidalgo S. L., et al., 2018, [ApJ](#), **856**, 125
- Hirschmann M., Naab T., Ostriker J. P., Forbes D. A., Duc P.-A., Davé R., Oser L., Karabal E., 2015, [MNRAS](#), **449**, 528
- Hocking A., Geach J. E., Sun Y., Davey N., 2018, [MNRAS](#), **473**, 1108
- Hopkins P. F., Bundy K., Murray N., Quataert E., Lauer T. R., Ma C.-P., 2009, [MNRAS](#), **398**, 898
- Huang S., et al., 2018a, [PASJ](#), **70**, S6
- Huang S., Leauthaud A., Greene J. E., Bundy K., Lin Y.-T., Tanaka M., Miyazaki S., Komiyama Y., 2018b, [MNRAS](#), **475**, 3348
- Hubble E. P., 1926, [ApJ](#), **64**, 321
- Jackson R. A., Martin G., Kaviraj S., Laigle C., Devriendt J. E. G., Dubois Y., Pichon C., 2020a, [MNRAS](#), **494**, 5568
- Jackson T. M., Pasquali A., Pacifici C., Engler C., Pillepich A., Grebel E. K., 2020b, [MNRAS](#), **497**, 4262
- Jackson T. M., Rosario D. J., Alexander D. M., Scholtz J., McAlpine S., Bower R. G., 2020c, [MNRAS](#), **498**, 2323
- Jackson T. M., Pasquali A., La Barbera F., More S., Grebel E. K., 2021, arXiv e-prints, [p. arXiv:2102.02241](#)

- 
- Katz N., Keres D., Dave R., Weinberg D. H., 2003, How Do Galaxies Get Their Gas?. p. 185, [doi:10.1007/978-94-010-0115-1\\_34](https://doi.org/10.1007/978-94-010-0115-1_34)
- Kauffmann G., et al., 2003, *MNRAS*, **346**, 1055
- Kennicutt Robert C. J., 1998, *ApJ*, **498**, 541
- Kereš D., Katz N., Weinberg D. H., Davé R., 2005, *MNRAS*, **363**, 2
- Kobayashi C., 2004, *MNRAS*, **347**, 740
- Koch A., Black C. S., Rich R. M., Longstaff F. A., Collins M. L. M., Janz J., 2017, *Astronomische Nachrichten*, **338**, 503
- Kormendy J., 1977, *ApJ*, **218**, 333
- Kroupa P., 2001, *MNRAS*, **322**, 231
- Kruijssen J. M. D., Pfeffer J. L., Crain R. A., Bastian N., 2019, *MNRAS*, **486**, 3134
- La Barbera F., Ferreras I., de Carvalho R. R., Lopes P. A. A., Pasquali A., de la Rosa I. G., De Lucia G., 2011, *ApJL*, **740**, L41
- La Barbera F., Ferreras I., de Carvalho R. R., Bruzual G., Charlot S., Pasquali A., Merlin E., 2012, *MNRAS*, **426**, 2300
- La Barbera F., Pasquali A., Ferreras I., Gallazzi A., de Carvalho R. R., de la Rosa I. G., 2014, *MNRAS*, **445**, 1977
- La Barbera F., et al., 2019, *MNRAS*, **489**, 4090
- Leaman R., et al., 2013, *ApJ*, **767**, 131
- Lees J. F., Knapp G. R., Rupen M. P., Phillips T. G., 1991, *ApJ*, **379**, 177
- Leja J., Johnson B. D., Conroy C., van Dokkum P. G., Byler N., 2017, *ApJ*, **837**, 170
- Leja J., et al., 2019, *ApJ*, **877**, 140
- Leja J., Speagle J. S., Johnson B. D., Conroy C., van Dokkum P., Franx M., 2020, *ApJ*, **893**, 111
- Lim S. H., Mo H. J., Lu Y., Wang H., Yang X., 2017, *MNRAS*, **470**, 2982
- Lintott C. J., et al., 2008, *MNRAS*, **389**, 1179
- Lu Z., Mo H. J., Lu Y., Katz N., Weinberg M. D., van den Bosch F. C., Yang X., 2015, *MNRAS*, **450**, 1604
- Ludwig J., Pasquali A., Grebel E. K., Gallagher John S. I., 2012, *AJ*, **144**, 190

- 
- Mancillas B., Duc P.-A., Combes F., Bournaud F., Emsellem E., Martig M., Michel-Dansac L., 2019, *A&A*, **632**, [A122](#)
- Maraston C., 2005, *MNRAS*, **362**, [799](#)
- Marinacci F., et al., 2018, *MNRAS*, **480**, [5113](#)
- Martín-Navarro I., La Barbera F., Vazdekis A., Falcón-Barroso J., Ferreras I., 2015, *MNRAS*, **447**, [1033](#)
- Martín-Navarro I., Vazdekis A., Falcón-Barroso J., La Barbera F., Yıldırım A., van de Ven G., 2018, *MNRAS*, **475**, [3700](#)
- Martínez-Delgado D., et al., 2010, *AJ*, **140**, [962](#)
- Mateus A., Sodré L., Cid Fernandes R., Stasińska G., Schoenell W., Gomes J. M., 2006, *MNRAS*, **370**, [721](#)
- McAlpine S., et al., 2016, *Astronomy and Computing*, **15**, [72](#)
- McAlpine S., Bower R. G., Harrison C. M., Crain R. A., Schaller M., Schaye J., Theuns T., 2017, *MNRAS*, **468**, [3395](#)
- Mendel J. T., Simard L., Palmer M., Ellison S. L., Patton D. R., 2014, *ApJS*, **210**, [3](#)
- Miyazaki S., et al., 2018, *PASJ*, **70**, [S1](#)
- Mo H., van den Bosch F. C., White S., 2010, *Galaxy Formation and Evolution*
- Morales G., Martínez-Delgado D., Grebel E. K., Cooper A. P., Javanmardi B., Miskolczi A., 2018, *A&A*, **614**, [A143](#)
- Mullaney J. R., Alexander D. M., Goulding A. D., Hickox R. C., 2011, *MNRAS*, **414**, [1082](#)
- Naab T., Johansson P. H., Ostriker J. P., Efstathiou G., 2007, *ApJ*, **658**, [710](#)
- Naab T., Johansson P. H., Ostriker J. P., 2009, *ApJL*, **699**, [L178](#)
- Naiman J. P., et al., 2018, *MNRAS*, **477**, [1206](#)
- Navarro J. F., Frenk C. S., White S. D. M., 1997, *ApJ*, **490**, [493](#)
- Nelson D., et al., 2015, *Astronomy and Computing*, **13**, [12](#)
- Nelson D., et al., 2018, *MNRAS*, **475**, [624](#)
- Nelson D., et al., 2019, *Computational Astrophysics and Cosmology*, **6**, [2](#)
- Newman A. B., Ellis R. S., Bundy K., Treu T., 2012, *ApJ*, **746**, [162](#)
- Noll S., Burgarella D., Giovannoli E., Buat V., Marcillac D., Muñoz-Mateos J. C., 2009, *A&A*, **507**, [1793](#)

---

O'Donnell C., Behroozi P., More S., 2020, arXiv e-prints, p. [arXiv:2005.08995](https://arxiv.org/abs/2005.08995)

Ogle P. M., Lanz L., Nader C., Helou G., 2016, [ApJ](#), **817**, 109

Ogle P. M., Lanz L., Appleton P. N., Helou G., Mazzearella J., 2019, [ApJS](#), **243**, 14

Oh K., Sarzi M., Schawinski K., Yi S. K., 2011, [ApJS](#), **195**, 13

Oser L., Ostriker J. P., Naab T., Johansson P. H., Burkert A., 2010, [ApJ](#), **725**, 2312

Oser L., Naab T., Ostriker J. P., Johansson P. H., 2012, [ApJ](#), **744**, 63

Pacifici C., Charlot S., Blaizot J., Brinchmann J., 2012, [MNRAS](#), **421**, 2002

Pacifici C., Oh S., Oh K., Lee J., Yi S. K., 2016, [ApJ](#), **824**, 45

Pasquali A., van den Bosch F. C., Mo H. J., Yang X., Somerville R., 2009, [MNRAS](#), **394**, 38

Pasquali A., Gallazzi A., Fontanot F., van den Bosch F. C., De Lucia G., Mo H. J., Yang X., 2010, [MNRAS](#), **407**, 937

Pasquali A., Smith R., Gallazzi A., De Lucia G., Zibetti S., Hirschmann M., Yi S. K., 2019, [MNRAS](#), **484**, 1702

Pillepich A., et al., 2018a, [MNRAS](#), **473**, 4077

Pillepich A., et al., 2018b, [MNRAS](#), **475**, 648

Pillepich A., et al., 2019, [MNRAS](#), **490**, 3196

Planck Collaboration et al., 2015, [A&A](#), **582**, A31

Planck Collaboration et al., 2016, [A&A](#), **594**, A13

Qu Y., et al., 2017, [MNRAS](#), **464**, 1659

Remus R.-S., Forbes D. A., 2021, arXiv e-prints, p. [arXiv:2101.12216](https://arxiv.org/abs/2101.12216)

Renzini A., 2006, [ARA&A](#), **44**, 141

Rosario D. J., Mendel J. T., Ellison S. L., Lutz D., Trump J. R., 2016, [MNRAS](#), **457**, 2703

Rosas-Guevara Y., Bower R. G., Schaye J., McAlpine S., Dalla Vecchia C., Frenk C. S., Schaller M., Theuns T., 2016, [MNRAS](#), **462**, 190

Salim S., et al., 2016, [ApJS](#), **227**, 2

Salpeter E. E., 1955, [ApJ](#), **121**, 161

Sánchez-Blázquez P., et al., 2006, [MNRAS](#), **371**, 703

Sánchez-Blázquez P., et al., 2014, [A&A](#), **570**, A6

---

Sánchez S. F., et al., 2012, [A&A](#), **538**, A8

Sánchez S. F., et al., 2013, [A&A](#), **554**, A58

Sanders D. B., Mirabel I. F., 1996, [ARA&A](#), **34**, 749

Sandin C., 2014, [A&A](#), **567**, A97

Schaye J., Dalla Vecchia C., 2008, [MNRAS](#), **383**, 1210

Schaye J., et al., 2015, [MNRAS](#), **446**, 521

Schlafly E. F., Finkbeiner D. P., 2011, [ApJ](#), **737**, 103

Scholtz J., et al., 2018, [MNRAS](#), **475**, 1288

Scholtz J., et al., 2020, [MNRAS](#), **492**, 3194

Scott N., et al., 2018, [MNRAS](#), **481**, 2299

Smith R., Pacifici C., Pasquali A., Calderón-Castillo P., 2019, [ApJ](#), **876**, 145

Spavone M., et al., 2017, [A&A](#), **603**, A38

Springel V., 2005, [MNRAS](#), **364**, 1105

Springel V., 2010, [MNRAS](#), **401**, 791

Springel V., Hernquist L., 2003, [MNRAS](#), **339**, 312

Springel V., White S. D. M., Tormen G., Kauffmann G., 2001, [MNRAS](#), **328**, 726

Springel V., et al., 2005, [Nature](#), **435**, 629

Springel V., et al., 2018, [MNRAS](#), **475**, 676

Suess K. A., Kriek M., Price S. H., Barro G., 2019, arXiv e-prints, p. [arXiv:1904.10992](#)

Taylor E. N., Franx M., Glazebrook K., Brinchmann J., van der Wel A., van Dokkum P. G., 2010, [ApJ](#), **720**, 723

Thomas D., Greggio L., Bender R., 1999, [MNRAS](#), **302**, 537

Thomas D., Maraston C., Bender R., Mendes de Oliveira C., 2005, [ApJ](#), **621**, 673

Thomas D., Maraston C., Schawinski K., Sarzi M., Silk J., 2010, [MNRAS](#), **404**, 1775

Tissera P. B., Machado R. E. G., Sanchez-Blazquez P., Pedrosa S. E., Sánchez S. F., Snaith O., Vilchez J., 2016, [A&A](#), **592**, A93

Trayford J. W., Schaye J., 2019, [MNRAS](#), **485**, 5715

---

Trayford J. W., et al., 2017, [MNRAS](#), **470**, 771

Trujillo I., et al., 2006, [MNRAS](#), **373**, L36

Trujillo I., Conselice C. J., Bundy K., Cooper M. C., Eisenhardt P., Ellis R. S., 2007, [MNRAS](#), **382**, 109

Trujillo I., Cenarro A. J., de Lorenzo-Cáceres A., Vazdekis A., de la Rosa I. G., Cava A., 2009, [ApJ](#), **692**, L118

Trujillo I., Ferreras I., de La Rosa I. G., 2011, [MNRAS](#), **415**, 3903

Trussler J., Maiolino R., Maraston C., Peng Y., Thomas D., Goddard D., Lian J., 2020, arXiv e-prints, p. [arXiv:2006.01154](#)

Valentinuzzi T., et al., 2010, [ApJ](#), **712**, 226

Vazdekis A., Sánchez-Blázquez P., Falcón-Barroso J., Cenarro A. J., Beasley M. A., Cardiel N., Gorgas J., Peletier R. F., 2010, [MNRAS](#), **404**, 1639

Vázquez-Mata J. A., et al., 2020, [MNRAS](#), **499**, 631

Vogelsberger M., et al., 2014a, [MNRAS](#), **444**, 1518

Vogelsberger M., et al., 2014b, [Nature](#), **509**, 177

Vulcani B., et al., 2011, [MNRAS](#), **413**, 921

Weinberger R., et al., 2017, [MNRAS](#), **465**, 3291

Weinmann S. M., van den Bosch F. C., Yang X., Mo H. J., 2006, [MNRAS](#), **366**, 2

Wetzell A. R., Tinker J. L., Conroy C., 2012, [MNRAS](#), **424**, 232

Wiersma R. P. C., Schaye J., Smith B. D., 2009a, [MNRAS](#), **393**, 99

Wiersma R. P. C., Schaye J., Theuns T., Dalla Vecchia C., Tornatore L., 2009b, [MNRAS](#), **399**, 574

Wilkinson D. M., et al., 2015, [MNRAS](#), **449**, 328

Wylezalek D., Flores A. M., Zakamska N. L., Greene J. E., Riffel R. A., 2020, [MNRAS](#), **492**, 4680

Yang X., Mo H. J., van den Bosch F. C., Pasquali A., Li C., Barden M., 2007, [ApJ](#), **671**, 153

York D. G., et al., 2000, [AJ](#), **120**, 1579

Young L. M., et al., 2011, [MNRAS](#), **414**, 940

Zhu L., et al., 2020, [MNRAS](#), **496**, 1579

- 
- Zibetti S., Gallazzi A. R., Hirschmann M., Consolandi G., Falcón-Barroso J., van de Ven G., Lyubenova M., 2020, [MNRAS](#), **491**, 3562
- Zirm A. W., et al., 2007, [ApJ](#), **656**, 66
- da Cunha E., Charlot S., Elbaz D., 2008, [MNRAS](#), **388**, 1595
- van Dokkum P. G., Franx M., 2001, [ApJ](#), **553**, 90
- van Dokkum P. G., et al., 2008, [ApJL](#), **677**, L5
- van Dokkum P. G., et al., 2010, [ApJ](#), **709**, 1018
- van de Sande J., et al., 2017a, [MNRAS](#), **472**, 1272
- van de Sande J., et al., 2017b, [ApJ](#), **835**, 104
- van den Bosch F. C., Pasquali A., Yang X., Mo H. J., Weinmann S., McIntosh D. H., Aquino D., 2008, arXiv e-prints, [p. arXiv:0805.0002](#)
- van der Wel A., Holden B. P., Zirm A. W., Franx M., Rettura A., Illingworth G. D., Ford H. C., 2008, [ApJ](#), **688**, 48
- van der Wel A., et al., 2014, [ApJ](#), **788**, 28